

Development of coated fibre-optic sensors to monitor carbon dioxide

by

Luis Melo

B.Sc., University of Aveiro, 2008

M.Sc., University of Aveiro, 2010

A Dissertation Submitted in Partial Fulfillment  
of the Requirements for the Degree of

DOCTOR OF PHILISOPHY

in the Department of Mechanical Engineering

© Luis Melo, 2016  
University of Victoria

All rights reserved. This dissertation may not be reproduced in whole or in part, by  
photocopy or other means, without the permission of the author.

# **Supervisory Committee**

Development of coated fibre-optic sensors to monitor carbon dioxide

by

Luis Melo

B.Sc., University of Aveiro, 2008

M.Sc., University of Aveiro, 2010

## **Supervisory Committee**

Dr. Peter Wild, Department of Mechanical Engineering  
**Supervisor**

Dr. Martin Jun, Department of Mechanical Engineering  
**Departmental Member**

Dr. Thomas Darcie, Department of Electrical and Computer Engineering  
**Outside Member**

## **Abstract**

### **Supervisory Committee**

Dr. Peter Wild, Department of Mechanical Engineering  
Supervisor

Dr. Martin Jun, Department of Mechanical Engineering  
Departmental Member

Dr. Thomas Darcie, Department of Electrical and Computer Engineering  
Outside Member

This dissertation presents a fibre-optic sensing approach to provide continuous measurements of CO<sub>2</sub> concentration at discrete points under typical conditions of geological CO<sub>2</sub> storage. Carbon capture and storage is considered to have potential for a large-scale reduction in CO<sub>2</sub> emissions in a relatively short period of time while other solutions to replace fossil fuels are being investigated. One significant drawback of carbon capture and storage is the possibility of long-term CO<sub>2</sub> leakage. Therefore, the development of reliable technology for monitoring, verification, and accounting of geological CO<sub>2</sub> storage is critical to fulfill safety regulations and achieve public acceptance. The major limitations of current technology include relatively low resolutions, high costs, and the lack of continuous monitoring for long periods of time.

To address these limitations, two types of fibre-optic sensors are investigated, namely long period gratings and Mach-Zehnder interferometers. The sensing principle for CO<sub>2</sub> detection is based on the sensitivity of these sensors to the refractive index of the medium that surrounds the fibre. Fibre-optic sensors are attractive for downhole applications due to the possibility of fabricating inexpensive high resolution devices that are able to operate in harsh environments over long periods of time.

This dissertation focuses on increasing the refractive index sensitivity of long period gratings and Mach-Zehnder interferometers by applying coatings that have a high refractive index. The dip-coating method is used to coat long period gratings with polystyrene, and the sensitivity at low refractive indices is increased by tuning coating thickness. The results show that long period gratings coated with polystyrene are able to

detect CO<sub>2</sub> in gaseous and aqueous media. This work reports the first measurement of CO<sub>2</sub> dissolution in water at high pressure with a fibre-optic sensor.

Additionally, atomic layer deposition is investigated to coat long period gratings and Mach-Zehnder interferometers with hafnium oxide. The study of this coating technique aims to address the main limitation of the dip-coating method: the challenge to achieve precise control over coating thickness. The results show that atomic layer deposition is suitable to maximize the sensitivity of long period gratings and Mach-Zehnder interferometers at a target refractive index.

# Table of Contents

|  |      |
|--|------|
| Supervisory Committee .....  | ii   |
| Abstract .....   | iii  |
| Table of Contents .....  | v    |
| List of Tables .....   | vi   |
| List of Figures .....  | vii  |
| List of Abbreviations .....  | viii |
| Acknowledgments .....  | x    |
| Dedication .....   | xi   |
| Chapter 1: Introduction .....  | 1    |
| Introduction .....   | 1    |
| 1.1 Overview of monitoring methods applied in geological CO <sub>2</sub> storage .....   | 3    |
| 1.2 Review of fibre-optic sensors for CO <sub>2</sub> detection .....  | 8    |
| 1.3 Objectives .....   | 14   |
| 1.4 Organization of dissertation .....   | 15   |
| Chapter 2: Literature review: Fibre-optic sensors for refractive index measurement .....   | 17   |
| Introduction .....   | 17   |
| 2.1 Long period gratings .....   | 19   |
| 2.2 Mach-Zehnder interferometers .....   | 29   |
| 2.3 Summary .....  | 36   |
| Chapter 3: Contributions .....   | 39   |
| Introduction .....   | 39   |
| 3.1 Highly sensitive coated long period grating sensor for CO <sub>2</sub> detection at atmospheric pressure .....                                 | 40   |
| 3.2 Experimental investigation of long-period grating transition modes to monitor CO <sub>2</sub> in high-pressure aqueous solutions .....         | 43   |
| 3.3 Long period gratings coated with hafnium oxide by plasma-enhanced atomic layer deposition for refractive index measurements .....              | 46   |
| 3.4 Refractive index sensor based on inline Mach-Zehnder interferometer coated with hafnium oxide by atomic layer deposition .....                 | 49   |
| Chapter 4: Summary contributions and future work .....   | 52   |
| 4.1 Summary contributions .....  | 52   |
| 4.2 Future work .....  | 56   |
| References .....   | 59   |
| Appendix A: Highly sensitive coated long period grating sensor for CO <sub>2</sub> detection at atmospheric pressure .....                         | 77   |
| Appendix B: Experimental Investigation of Long-Period Grating Transition Modes to Monitor CO <sub>2</sub> in High-Pressure Aqueous Solutions ..... | 85   |
| Appendix C: Long period gratings coated with hafnium oxide by plasma-enhanced atomic layer deposition for refractive index measurements .....      | 93   |
| Appendix D: Refractive index sensor based on inline Mach-Zehnder interferometer coated with hafnium oxide by atomic layer deposition .....         | 110  |

## List of Tables

|   |    |
|---|----|
| Table 2-1. Summary of RI-based FOSs ..... | 38 |
|---|----|

## List of Figures

|  |    |
|--|----|
| Figure 1-1. Illustration of the phase diagram for CO <sub>2</sub> .....  | 2  |
| Figure 1-2. Schematic of the integration of various MVA methods in CO <sub>2</sub> storage in saline aquifers. Reprinted with permission from [13]. Copyright 2011 American Chemical Society. ....   | 7  |
| Figure 1-3. Illustration of FOS arrays for monitoring CO <sub>2</sub> leakages in geological storage sites.....  | 11 |
| Figure 2-1. Schematic of an LPG .....  | 20 |
| Figure 2-2. SRI characterization of a typical LPG. Reprinted with permission from [86]. Copyright 1997 The Optical Society.....  | 22 |
| Figure 2-3. Plot of resonance wavelength as a function of grating period for coupling between core mode and cladding modes of order m=11 (curve on the right hand side) to m=20 (curve on the left hand side). © 2002 IEEE [88]. ....                    | 24 |
| Figure 2-4. Wavelength shift as a function of the SRI for different modes of an LPG coated with 150 nm layer of polystyrene, Reprinted with permission from [101]. Copyright 2005 The Optical Society .....  | 26 |
| Figure 2-5. Different MZI configurations for RI measurements, fabricated by (a) two LPGs in-line; (b) single-mode fibre tapering; (c) lateral offset splicing; (d) core diameter mismatch; (e) fibre peanut-shape structure; (d) laser irradiated points | 30 |
| Figure 2-6. (a) solid core and (b) hollow core photonic crystal fibre .....  | 30 |
| Figure 2-7. Illustration of a PCF interferometer.....  | 32 |
| Figure 2-8. Characterization of a PCF interferometer to SRI changes. Reprinted with permission from [130]. Copyright 2009 The Optical Society.....   | 34 |

## List of Abbreviations

|                                |   |
|--------------------------------|---|
| Al <sub>2</sub> O <sub>3</sub> | Aluminium Oxide   |
| ALD                            | Atomic Layer Deposition   |
| CCS                            | Carbon, Capture and Storage   |
| CVD                            | Chemical Vapor Deposition   |
| DTP                            | Dispersion Turning Point  |
| EC                             | Eddy Covariance   |
| ESA                            | Electrostatic Self-Assembly   |
| FBG                            | Fibre Bragg Grating   |
| FOS                            | Fibre optic sensor  |
| FPI                            | Fabry-Perot Interferometer  |
| FSR                            | Free Spectral Range   |
| FWHM                           | Full Width at Half Maximum  |
| LPG                            | Long Period Grating   |
| MVA                            | Monitoring, Verification and Accounting of geological CO <sub>2</sub> storage |
| MZI                            | Mach-Zehnder Interferometer   |
| OH                             | Hydroxyl group  |
| PCF                            | Photonic Crystal Fibre  |
| RI                             | Refractive Index  |
| scCO <sub>2</sub>              | Supercritical Carbon Dioxide  |
| SEM                            | Scanning Electron Microscopy  |
| SiO <sub>2</sub>               | Silica glass  |

|                  |                              |
|------------------|------------------------------|
| SRI              | Surrounding Refractive Index |
| TFBG             | Tilted Fibre Bragg Grating   |
| TiO <sub>2</sub> | Titanium Dioxide             |

## Acknowledgments

This dissertation summarizes a research that contributed to a professional and personal growth which has been supported by several people.

First and foremost I would like express my gratitude to my supervisor, Dr. Peter Wild, for guiding me in this work and being always supportive to tackle challenging research topics. His technical expertise and personal qualities have had a significant impact on the way I approach my research work. He has also challenged my technical writing skills to create quality and concise academic writing.

I would like to thank Dr. Tao Lu for technical discussions and Dr. Martin Jun for the access to his Lab and for encouraging collaborations with his research group.

I would like to thank my former and current colleagues, Ben Davies, Stephen Warwick, Reza Harirforoush, and Elizabeth Trudel for creating an enjoyable working atmosphere. In particular, I am grateful to Geoff Burton who has designed and manufactured the rigs used in this work, provided technical support in experiments, and helped to revise manuscripts and this dissertation. Geoff started as a colleague, always contributing with valuable discussions about my research with positive feedback, and has become a life-long friend.

I would like thank two special friends, Jean Duquette for his company in the morning coffees and discussions about life-future plans, and Kelly Henderson for inspiring my life through tango.

I would like to thank my best friend, Agnieszka Broda, for being a good listener, for all the patience, and for believing in me.

Finally I am grateful to my family, in special my sisters and my mother for unconditional love.

## **Dedication**

To my father, Luis Brito e Melo, and my mother, Alda Brito e Melo

# Chapter 1: Introduction

## Introduction

Carbon capture and storage (CCS) consists of the capture of CO<sub>2</sub> from major emission facilities such as coal power plants, and its subsequent storage over long periods of time [1], [2].

Different types of sites have been identified for CO<sub>2</sub> storage such as depleted oil and gas reservoirs, unmineable coalbeds, and oceans and saline aquifers (at sufficient depth to reduce the likelihood of leakage) [1]. Saline aquifers are currently the most attractive option for CO<sub>2</sub> storage due the high number of available sites, relative proximity to the major CO<sub>2</sub> emission sources and potential for large storage volumes [3].

The saline aquifers suitable for CO<sub>2</sub> storage are typically located at depths of more than 800 m because, at these depths, the CO<sub>2</sub> can be stored in a high density state (*i.e.* either as a liquid or in the supercritical state) [4]. The critical point at which CO<sub>2</sub> behaves as supercritical fluid (scCO<sub>2</sub>) is at temperatures and pressures above 31.1 °C and 1072 psi (73.8 bar) [5], respectively (see Figure 1-1). In saline aquifers located at sequestration depths, CO<sub>2</sub> is in a liquid state if the temperature is below the critical point, and in supercritical state if the temperature is above the critical point (*i.e.* assuming thermal and pressure gradients of 30 °C/km and 105 bar/km, respectively) [5].

In the storage process, scCO<sub>2</sub> is injected into a deep saline aquifer and propagates as a plume which is immiscible in saline water (*i.e.* brine). The density of scCO<sub>2</sub> is less than the density of brine, and buoyant forces will drive the CO<sub>2</sub> plume upward within the saline

aquifer. CO<sub>2</sub> will then dissolve into the brine and the rate of dissolution is a function of temperature, pressure and brine composition [3]. This reaction is expected to take place over time scales of hundreds or thousands of years. CO<sub>2</sub> saturated brine is more dense than typical brine, and thus CO<sub>2</sub> saturated brine will sink to the bottom of the saline aquifer [3].

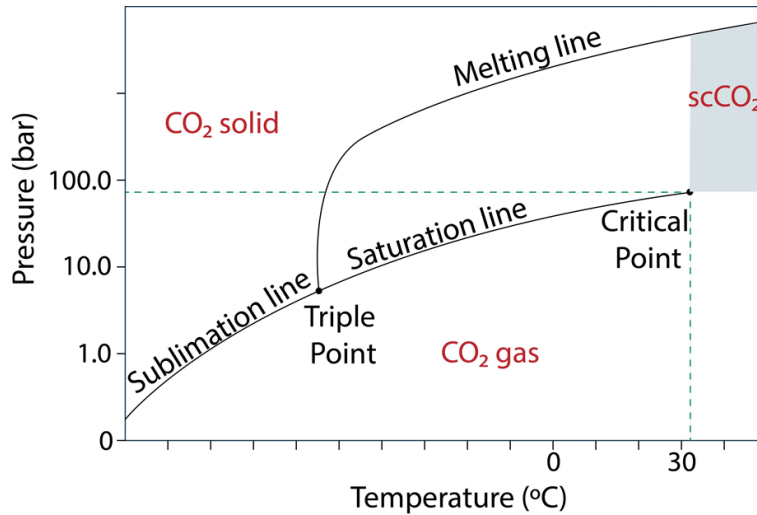


Figure 1-1. Illustration of the phase diagram for CO<sub>2</sub>

The vertical or lateral migration of CO<sub>2</sub> from the storage reservoir is hindered by low permeability caprocks that surround the saline aquifers. However, there are legitimate concerns that sequestered CO<sub>2</sub> may leak into the groundwater or to the surface as a result of the caprock failure, presence of faults or through poorly cemented boreholes [6].

The development of reliable technology for monitoring, verification and accounting of geological CO<sub>2</sub> storage (MVA) is important for four reasons: to determine storage effectiveness (*i.e.* reduction of CO<sub>2</sub> emissions), to meet safety considerations, to gain public acceptance, and to fulfil public regulations.

A number of monitoring methods have been developed to confirm CO<sub>2</sub> storage and/or to detect possible CO<sub>2</sub> leakage from storage reservoirs. A discussion of current methods is provided in Section 1.1.

## 1.1 Overview of monitoring methods applied in geological CO<sub>2</sub> storage

Monitoring technologies applied in MVA include deep-subsurface, near-surface, and atmospheric monitoring methods. Current deep-subsurface monitoring methods include seismic, gravimetric, and electromagnetic methods [4].

Seismic methods measure the velocity or the signal attenuation of seismic waves due to the interference (*i.e.* reflecting or propagating) with materials that have different densities. There are three main configurations: 3D surface seismic, vertical seismic and cross-hole seismic. The main difference between these three configurations is the location of the seismic wave source and the receiver array in the storage site, as described by Chadwick *et al.* [4]. This technology has the potential to measure the total amount of CO<sub>2</sub> stored in a deep saline aquifer as well as to identify the migration of a CO<sub>2</sub> plume from a reservoir to the overburden [7].

The image resolution of seismic methods is highly dependent on the properties of the geological formation. For instance, the image quality decreases when this method is applied in reservoirs that are sealed by cap rocks with low porosity and low permeability [4]. The limit of detection of a CO<sub>2</sub> plume is given by the minimum mass of CO<sub>2</sub> sufficient to produce a discernible seismic response. One study suggests that the limit of detection to identify a CO<sub>2</sub> plume in favourable site conditions is higher than 10,000 tonnes of CO<sub>2</sub> for 3D surface seismic and higher than 100 tonnes of CO<sub>2</sub> for crosswell seismic [4]. Seismic methods also have limited spatial resolution, on the order of tens of meters [8]. Finally, the number of surveys acquired in CCS applications has been typically limited to one survey per year due to the high cost and complexity of data analysis [8], [9].

Gravimetric methods measure the gravitational effects of mass distributions within the earth to detect changes in the density of the medium [4]. Although gravimetric methods have lower spatial resolution than seismic methods, gravimetry can be used to obtain extra information that seismic methods cannot provide. For example, gravimetric methods can be used to estimate the rate of CO<sub>2</sub> dissolution in brine whereas dissolved CO<sub>2</sub> in brine is invisible in seismic data [4], [7].

Electromagnetic methods measure the conductivity contrast between CO<sub>2</sub> (*i.e.* relatively resistive) and brine (*i.e.* relatively conductive). This method can be used to track the migration of a CO<sub>2</sub> plume from a storage site. Electromagnetic methods have a similar resolution to that of seismic methods and have been used in conjunction with seismic methods to reduce the uncertainty in the interpretation of data [10]. However, the use of electromagnetic methods is limited to non-conductive well casings [7]. The application of this technology requires further investigation since the electric properties of CO<sub>2</sub> distributed in geological storage sites are not fully understood [4].

In addition to the methods described above, the measurement of subsurface temperature, pressure, and pH can be used to monitor a CO<sub>2</sub> injection, assess the integrity of the reservoir, and help in tracking CO<sub>2</sub> migration [11].

Near-surface monitoring methods are applied to detect CO<sub>2</sub> leakage at depths of up to 100 m. In this region, a leak of CO<sub>2</sub> is in a gas phase assuming geothermal and pressure gradients of 30 °C/km and 105 bar/km [5], respectively. The CO<sub>2</sub> is expected to occupy the empty spaces in the soil or to accumulate in shallow freshwater aquifers [4]. The most common near-surface monitoring methods to detect CO<sub>2</sub> leakage are soil gas monitoring and groundwater geochemical sampling [7].

Soil gas monitoring is used to measure the composition of a gas sample in the vadose zone (*i.e.* typically less than 10 m deep) at specific locations where the leakage is more likely to occur. At each location, a well is drilled to accommodate a tube which collects the gas samples. The sample is drawn from the tube and externally analyzed using different analytical techniques including infrared absorption based sensors, gas chromatography, and Fourier transform infrared spectroscopy [12]. A challenge associated with soil gas monitoring is to differentiate between injected CO<sub>2</sub> and native CO<sub>2</sub> to determine whether the measurement is a leakage or CO<sub>2</sub> background levels. Therefore, long-term monitoring prior to injection is important to establish a baseline [12]. Additional information can also help to differentiate between native and leakage CO<sub>2</sub>. For example, by measuring chemical tracers (*e.g.* perfluorocarbon) which are introduced along with the injected CO<sub>2</sub> in the storage site, native and leaked CO<sub>2</sub> can be differentiated from one another [7].

Groundwater geochemical sampling is based on the analysis of samples drawn from observation wells typically located at less than 100 m deep. Similar to soil gas analysis, the water samples are analyzed to identify the concentration of CO<sub>2</sub> and chemical tracers [7]. The major limitation of groundwater geochemical sampling is the challenge to preserve *in-situ* pressure and temperature of the samples for chemical analysis [7]. Different pressure and temperature conditions change solubility of CO<sub>2</sub> in water and causes CO<sub>2</sub> to degas from the water sample [7].

Atmospheric monitoring methods are well established as they have been developed to monitor CO<sub>2</sub> levels in the atmosphere over the last six decades [4]. The current methods applied in MVA include tracking atmospheric tracers (*i.e.* similarly to near-surface

monitoring described above), and the utilization of the Eddy Covariance (EC) flux technique [7].

The EC flux technique uses optical sensors mounted in an observation tower in combination with meteorological parameters such as wind speed and direction, relative humidity and temperature. Mathematical models are then used to determine CO<sub>2</sub> flux, expressed as the amount of CO<sub>2</sub> per unit area per unit time. This method allows measurement of CO<sub>2</sub> flux in an area up to several square kilometres [12].

In a typical MVA program, a number of monitoring methods described above are used to obtain complementary data. An illustration of the integration of different methods to monitor CO<sub>2</sub> storage in a saline aquifer is shown in Figure 1-2. Unfortunately, the available methods suffer from limitations, which hinder the development of a fully reliable monitoring plan. In particular, deep-subsurface monitoring methods are unable to: (1) measure CO<sub>2</sub> concentration dissolved in brine accurately; (2) detect small CO<sub>2</sub> accumulations (*i.e.* plumes with less than 100 tonnes of CO<sub>2</sub>); and (3) provide continuous monitoring of CO<sub>2</sub>.

Fibre-optic sensors (FOSs) have been widely explored for chemical and environmental monitoring due to the possibility of producing small sized sensors with high resolution that can be remotely and continuously operated in contact with a sample. Additional advantages inherent to optical fibres include immunity to electromagnetic interferences, low cost, low signal losses, and the ability to operate under water and in harsh environments.

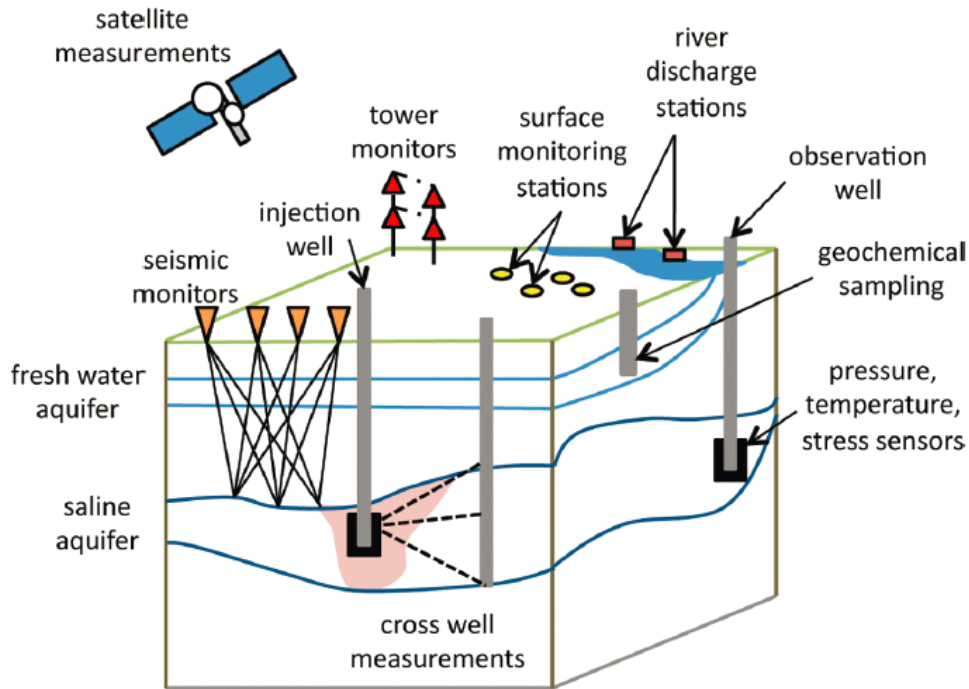


Figure 1-2. Schematic of the integration of various MVA methods in CO<sub>2</sub> storage in saline aquifers. Reprinted with permission from [13]. Copyright 2011 American Chemical Society.

The advantages of FOSs have triggered the development of sensors for downhole applications. Temperature and pressure sensors are already a mature technology and various sensor configurations have been explored by the oil and gas industry for downhole monitoring [14], [15]. Examples of downhole configurations include: distributed temperature sensing based on the detection of back-scattering light using Rayleigh, Raman, or Brillouin principles [16], [17]; Fabry-Perot interferometers (FPIs) [18], [19]; and fibre Bragg gratings (FBGs) [20], [21]. FOS for downhole applications are already commercialized by a number of companies such as Schlumberger [22], Verrillon [23], and AFL [24].

The utilization of FOS in CCS applications to monitor temperature and pressure have been already demonstrated. For instance, distributed temperature sensing and FBGs were

applied at a CCS pilot well in Ketzin, Germany, to monitor temperature and pressure at various depths ranging from near-surface to deep-subsurface depths [25], [26].

FOSs for the detection of CO<sub>2</sub> in downhole environments are not commercially available. This technology is a promising candidate for near-surface and deep-subsurface monitoring in CCS applications with the potential to overcome the identified limitations of current MVA technology.

Section 1.2 provides a review of fibre-optic sensors for detection of CO<sub>2</sub> in a general context. The possibility to adapt existing sensor configurations for CCS application is also discussed in the next section.

## **1.2 Review of fibre-optic sensors for CO<sub>2</sub> detection**

Over the last two decades, various sensor configurations to measure CO<sub>2</sub> concentrations have been reported. These configurations are divided into three different groups based on the mechanism of detection, namely fluorescence [27], [28], absorption [29], [30] and refractive index (RI) [31], [32].

Fluorescence based sensors measure CO<sub>2</sub> concentration in aqueous solutions based on pH [28]. The dissolution of CO<sub>2</sub> in water produces carbonic acid which decreases the pH of the solution. The change in pH can be detected by selected deprotonated dyes coated on the core [27] or tip [28] of an optical fibre. The decrease in pH results in the reduction of fluorescence intensity at a specific wavelength [28]. Fluorescence based sensors have been widely applied to monitor CO<sub>2</sub> concentration in aqueous media at atmospheric conditions; however, this type of sensors is not well-suited for downhole applications because the harsh, high pressure environment can cause the dye to leach out, causing erroneous signals and premature failure [28].

Absorption based sensors are used to monitor concentrations of CO<sub>2</sub> in a gas environment [29], [30]. Two types of sensor configurations have been reported, namely extrinsic and intrinsic sensors. Extrinsic sensors use an optical fibre to direct the light from a laser source to the gas. CO<sub>2</sub> has a strong absorption band at the wavelength region of 2 μm, which causes the intensity of the transmitted signal to decrease as a function of CO<sub>2</sub> concentration [29]. Intrinsic sensors are based on the interaction between CO<sub>2</sub> and the evanescent field adjacent to an optical fibre. A multimode fibre is used to guide the light in the wavelength range corresponding to the absorption bands of CO<sub>2</sub> and the fibre cladding is removed to extend the evanescent field into the surrounding medium [33], [34]. The transmission signal is a function of CO<sub>2</sub> concentration in the surrounding region into which the evanescent field of the multimode fibre extends [34]. Microstructured optical fibre can also be used to develop intrinsic sensors. The air holes of this type of fibre can be filled with a gas mixture containing CO<sub>2</sub>, leading to increased interaction between the gas and the light field of the optical modes [30].

The utilization of absorption based sensors to monitor CO<sub>2</sub> storage at near-surface depths was demonstrated by Soukup *et al* [35]. The authors developed an extrinsic sensor to monitor CO<sub>2</sub> concentrations which was field tested using a controlled release in Montana, USA. The limit of detection of this sensor is 1000 ppm [35]. Although absorption based CO<sub>2</sub> sensors can reach higher resolution in a gas environment (*i.e.* less than 500 ppm [33]), the use of these sensors to detect dissolution of liquid CO<sub>2</sub> in water at carbon sequestration conditions as not been demonstrated to date. The main challenge of this approach is to analyze the complex spectral absorption bands of multiple fluids present in saline aquifers (e.g. water, CO<sub>2</sub>, CO<sub>2</sub> saturated water, methane, among others).

RI-based sensors have been developed to monitor CO<sub>2</sub> at different pressures. Avdeev *et al.* investigated the utilization of a fibre tip sensor to distinguish between different CO<sub>2</sub> phases based on Fresnel reflection at the interface of the fibre tip [36]. This is a suitable approach to monitor phase changes; however, the utilization of fibre tip sensors to monitor dissolution of CO<sub>2</sub> in water is challenging due to the low RI sensitivity of these devices. Recently, various sensor configurations have been proposed to monitor CO<sub>2</sub> at atmospheric pressure. Pevec *et al.* reported the development of a nanowire etched on the tip of an optical fibre [31]. This sensor was able to distinguish between CO<sub>2</sub> (RI of 1.00044) and H<sub>2</sub> (RI of 1.00013) based on the difference in the RI of the two gases. Shivananju *et al.* reported a CO<sub>2</sub> sensor using carbon nanotubes coated on the core of an etched FBG [32]. This sensor was used to monitor concentrations of CO<sub>2</sub> as low as 1000 ppm. However, none of these sensor configurations have been shown to be effective in measuring CO<sub>2</sub> in deep-subsurface environments.

FOS for deep-subsurface monitoring of CO<sub>2</sub> must fulfill a number of performance requirements including high resolution, mechanical robustness for survival in harsh environments, optical stability to operate over long periods of time, and low optical losses to propagate the signal from great depth.

Over the last decade, the research interest on RI-based sensors has increased significantly, enabling the fabrication of sensors with high resolution that are able to continuously monitor RI *in-situ* [37]. Examples of RI sensors include fibre tapers, surface plasmon resonance sensors, grating-based sensors, and fibre interferometers. The typical resolution of these devices operating in aqueous media is between  $10^{-3}$  –  $10^{-4}$  RI units (RIU) [38]–[40]. The resolution of grating-based sensors and fibre interferometers can be

increased by coating the fibre with a material whose RI is higher than that of the cladding [41]. This method has been widely applied in long period gratings (LPGs) and more recently in Mach-Zehnder interferometers (MZI) leading to sensor resolutions in the order of  $10^{-6}$  at the RI of water [42], [43].

In the context of CCS applications, there are two main scenarios for which RI-based sensors are potentially important. The first is to detect the displacement of brine due to the propagation of a CO<sub>2</sub> plume within the storage reservoir during injection or in an adjacent saline aquifer due to CO<sub>2</sub> migration. The second is to detect long-term dissolution of CO<sub>2</sub> in brine within the storage reservoir after injection or, again, in adjacent saline aquifers due to CO<sub>2</sub> migration). These two scenarios are illustrated in Figure 1-3.

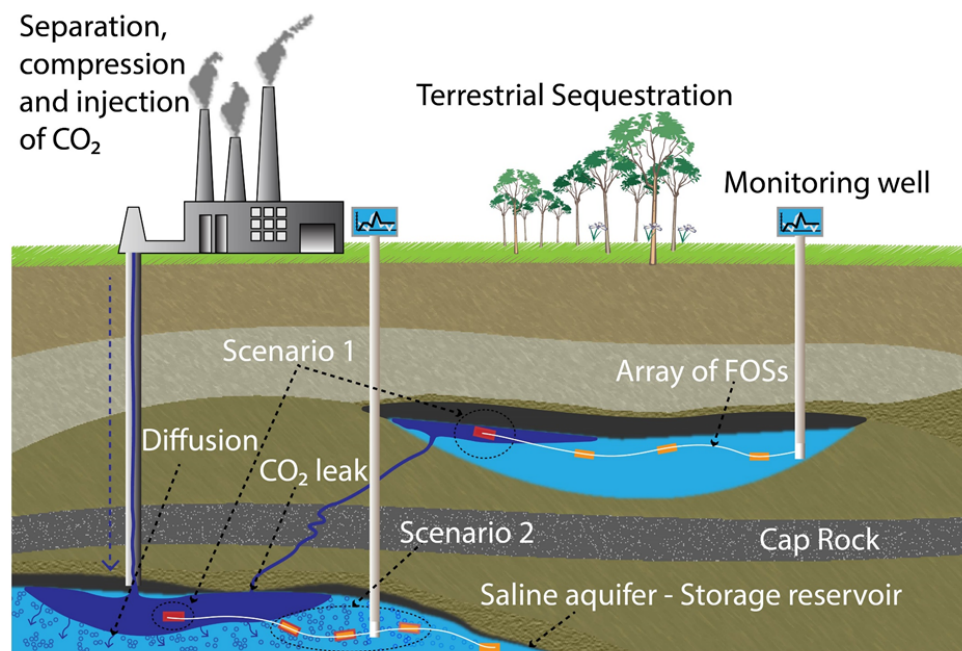


Figure 1-3. Illustration of FOS arrays for monitoring CO<sub>2</sub> leakages in geological storage sites

In Scenario 1, a sensor must detect the difference between the RI of the formation water in a saline aquifer and that of the pure CO<sub>2</sub> at high pressure. The RI of pure water and pure

CO<sub>2</sub> at 25 °C and 1400 psi are 1.335 and 1.18, respectively [44], [45]. This corresponds to a RI difference of 0.155 RIU between water and pure CO<sub>2</sub>.

In Scenario 2, CO<sub>2</sub> is expected to dissolve into the formation water of saline aquifers over a long period of time. The RI of water as a function of CO<sub>2</sub> concentration can be predicted using the Lorentz-Lorenz equation [46]. Assuming available data at 25 °C and 1400 psi, the density of pure water is 1.0013 g/ml, the density of pure CO<sub>2</sub> is 0.81180 g/ml, the RI of pure water is 1.335 and the RI of pure CO<sub>2</sub> is 1.18 [47]. Considering a concentration target of 100 ppm of CO<sub>2</sub> in water as the detection limit, the RI of the water-CO<sub>2</sub> system calculated by Lorentz-Lorenz equation is 1.334. This RI value corresponds to a difference of  $1.15 \times 10^{-5}$  RIU between pure water and water with a CO<sub>2</sub> concentration of 100 ppm. For a more detailed description of this calculation, the reader is referred to the manuscript in Appendix B or [48].

The resolution of reported RI-based sensors, in particular for coated LPGs and MZIs, is approximately five orders of magnitude higher than the RI change in Scenario 1. The resolution of these sensors is also one order of magnitude higher than the target resolution calculated in Scenario 2. These preliminary calculations suggest that RI-based sensors are well suited to distinguish between CO<sub>2</sub> and water, and are a promising approach to detect low concentrations of CO<sub>2</sub> in water at high pressure.

In a field application, sensor robustness is an important aspect to avoid potential damage during deployment of sensors in monitoring wells. Additionally, temperature and pressure, parameters that can lead to fibre fracture, are dependent on the depth at which the sensors are installed. Therefore, it is important to ensure that the sensors are design to withstand the thermal expansion as well as the loads applied to the fibre under downhole

conditions. Sensors that are intrinsically sensitive to RI, such as LPGs and MZIs, are preferred because they retain the mechanical integrity of the optical fibre compared to fibre tapers or sensors that require etching, such as FBGs.

The other important performance requirement in this application is the long-term stability of the sensors. Grating-based sensors and MZIs have shown high optical stability, unlike fibre tapers which show significant degradation of optical performance, typically in less than a week [49]. Additionally, one concern associated to the utilization of optical fibres in downhole applications is the diffusion of H<sub>2</sub> into the core of the fibre which may lead to an increase of optical losses [50]. The presence of H<sub>2</sub> in the fibre leads to the formation of hydroxyl (OH) groups, which bond with the oxygen atoms of the silica glass (SiO<sub>2</sub>) as well as with germanium dopants (GeO<sub>2</sub>) present in standard single mode fibre (SMF) [51]. The effect of hydrogen diffusion into optical fibres on the sensor performance is not well documented in the literature and is out of the scope of this dissertation. However, it is known that the effect of hydrogen diffusion is less pronounced in dopant-free fibres such as pure silica fibre [52]. LPGs [53] and MZIs [54] have been fabricated in pure silica fibres including photonic crystal fibre (PCF).

Finally, the development of FOS for CCS applications has to account for long transmission lengths due to the depth of geological sites suitable for CO<sub>2</sub> (*i.e.* deeper than 800 m). It is important to select sensors that can be fabricated using SMF and with low insertion losses. LPGs and MZIs are well suited for remote monitoring because they fulfil these two conditions [55], [56].

Based on the performance requirements discussed above, LPGs and MZIs are promising candidates for monitoring CO<sub>2</sub> storage in downhole environments. The wide

utilization of LPGs and MZIs in various applications confirm the reliability of these sensors. A detailed discussion of RI-based sensors is provided in Chapter 2.

### 1.3 Objectives

The overarching objective of this research is to develop RI-based FOSs to monitor CO<sub>2</sub> concentrations in CCS applications. The main identified challenges of the overarching objective include selectivity to CO<sub>2</sub>, confounding effects due to temperature and pressure changes, and RI sensitivity. This research aims to address the topic of RI sensitivity by investigating the coating of LPGs and MZIs.

The work presented in this dissertation is organized into specific objectives that progress towards reaching the overarching objective.

The first objective is to increase the sensitivity of LPGs at the low SRI range required to monitor CO<sub>2</sub> storage (*i.e.* between 1.0 - 1.335). The minimum sensitivity target in this work is 100 nm/SRI which corresponds to a sensor resolution of  $1 \times 10^{-5}$  (*i.e.* assuming a resolution of 1 pm for a fibre-optic based interrogation system). This will be investigated by coating LPGs with polystyrene using the dip-coating method.

The second objective is to validate the performance of polystyrene coated LPGs as sensors for monitoring CO<sub>2</sub> concentrations at atmospheric pressure in the gas phase and at high pressure in liquid phase (*i.e.* 1400 psi). These two conditions simulate monitoring of CO<sub>2</sub> geological storage in shallow and deep-subsurface environments, respectively.

The third objective is to improve the control of coating thickness on optical fibres relative to that achievable by the dip-coating method. Atomic layer deposition (ALD) will be investigated to coat LPGs and MZIs with hafnium oxide (HfO<sub>2</sub>). The ultimate goal is to develop sensors with maximum RI sensitivity at a target SRI.

The CO<sub>2</sub> tests conducted in this research are performed under laboratory conditions, *i.e.* temperature controlled tests with selected chemical species. For field application of the sensors in downhole conditions, the reader is referred to future work described in Chapter 4.

#### **1.4 Organization of dissertation**

This dissertation is presented in the manuscript format, comprising a body and four appendices. The body contains an introductory chapter, background information on the sensors investigated in this work, discussion of the contributions of the research, summary of the key contributions and future work considerations. Each study is presented in detail in a separate manuscript which has been published in a peer reviewed journal. The manuscripts are presented in the appendices.

In Chapter 1, the motivation of the work was presented. This chapter starts with a discussion of the state-of-art of available technology for MVA. This discussion highlights the limitations of current monitoring methods. A review of CO<sub>2</sub> sensors based on fibre-optic technology is also provided in Chapter 1. This review demonstrates that RI-based sensors are promising candidates for CCS applications; however, CO<sub>2</sub> sensors proposed to date are not well-suited for downhole environments.

In Chapter 2, background information of the sensors investigated in this research is presented, namely LPGs and MZIs. This discussion focuses on the RI sensitivity of the sensors as the main sensing principle explored in this work. The effect of coatings to increase RI sensitivity is also presented in Chapter 2. The chapter is concluded with a summary of important considerations that guide the reader to Chapter 3.

Chapter 3 presents the main four studies of this research in different sections. Each section comprises an introduction, methods, key results and logical progression of each manuscript that is presented in the appendix section.

Finally, Chapter 4 summarizes the key contributions of the dissertation and provides new insights for future work.

## **Chapter 2: Literature review: Fibre-optic sensors for refractive index measurement**

### **Introduction**

Over the last decade, the development of FOS for measuring RI has experienced significant growth, in which various types of optical fibres have been explored to develop new sensor configurations [37], [57].

The growth of the telecommunication industry stimulated the use of SMFs for sensor fabrication due to the reduction of transmission losses in this type of fibre as well as the development of optical equipment for SMFs such as light sources and optical interrogators. However, a number of FOSs have also been fabricated using other types of fibres such as multimode [58], D-shape [59], [60], and microstructured fibre including plastic optical fibre (POF) [61] and PCF [62].

For RI measurements, the simplest FOS is based on Fresnel reflection that occurs at the tip of an optical fibre [63]. When light exits the tip of a fibre, the percentage of light that is reflected back into the fibre is a function of the SRI. This intensity based approach is attractive to discriminate between substances that have significantly different RIs [63], or in the same substance to discriminate between different phases [36]. However, the utilization of fibre tip sensors to monitor small RI changes is limited due to the weak RI resolution of this sensor.

Fibre tapering has been also widely investigated for RI measurements [64], [65]. The RI sensitivity of fibre tapers arises from the interaction between the fraction of light guided

in an optical fibre that extends beyond the fibre (*i.e.* the evanescent field) and the medium surrounding the fibre. The RI sensitivity increases with the reduction of the taper waist with the expense of the sensor becoming more brittle [65].

Grating-based sensors have attracted particular attention due to the possibility of fabricating sensors with high RI sensitivity and long-term optical stability [55]. FBGs are well-known devices that have been widely used to measure temperature and strain [66]; however, the utilization of FBGs to measure RI requires partial etching of the fibre cladding [67]. Tilted FBGs (TFBGs) are devices that have intrinsic sensitivity to RI and have been successfully used to measure various parameters simultaneously such as temperature, strain and RI, with a single grating [68]. The main disadvantages of TFBGs are the high polarization dependence and the complex demodulation methods [69]. LPGs are also intrinsically sensitive to RI [55]. This type of grating has been often preferred over TFBGs due to lower polarization dependence, easier fabrication and simpler demodulation methods [55].

LPGs have been successfully developed for biochemical applications for detection of *Escherichia coli* (*E. coli*) in water [70], in biological applications to detect DNA hybridization in real time [71], and environmental applications to monitor moisture content in concrete structures [72] and corrosion in steel bars for structural health monitoring [73].

Fibre-optic interferometers offer an alternative approach for measurement of RI and can be divided into different configurations, namely: FPIs, Michelson interferometers (MIs), and MZIs [38]. FPIs have shown low temperature dependence and high RI sensitivity [74], [75]. However, the intensity of the output signal and the amplitude of the fringes are significantly reduced when the sensors are immersed in liquids [74], [75]. This

phenomenon occurs due to the reduction of the RI contrast between the FP cavity and the fibre (*i.e.* silica), which leads to lower Fresnel reflections at the FP cavity end-faces. As a result, the signal-to-noise ratio decreases and the interrogation based on wavelength becomes challenging. This configuration has been explored in gas sensing applications for detection of volatile organic compounds [76], and hydrogen [77]. MIs have been developed for applications that benefit from sensors that are interrogated in reflection [38]. An example of a typical application of MIs is the measurement of liquid level [78], [79]. However, MIs have not been preferred for RI measurements due to the relatively low RI sensitivity. MZIs have attracted greater attention due to the possibility of producing low-cost sensors with high RI sensitivity using simple fabrication methods [38]. Examples of applications of MZIs include measurement of humidity [80], measurement of glucose concentration in water [81] and measurement of sodium chloride in water [82].

LPGs and MZIs are investigated in this work for RI measurements. The basic properties of these sensors are discussed in Sections 2.1 and 2.2. In particular, this discussion is focused on the response of these sensors to changes in the SRI. The potential to increase the RI sensitivity of LPGs and MZIs by applying coatings that have a higher RI than silica is also discussed in Sections 2.1 and 2.2, respectively.

## **2.1 Long period gratings**

Fibre gratings are formed by inducing a periodic modulation of the RI of the core of an optical fibre [55]. These optical devices can be divided into two general classifications based on the length of the period modulations. FBGs have a submicron period which enables coupling between the fundamental core mode to a counter-propagating core mode [83]. LPGs have a period between 100  $\mu\text{m}$  and 1000  $\mu\text{m}$  which enables coupling between

the fundamental core mode and several cladding modes in the forward propagation direction (see Figure 2-1) [84]. The cladding modes attenuate as they propagate along the fibre axis due to high scattering losses at the interface between the cladding and the surrounding medium. As a consequence, the transmission spectrum of an LPG consists of a series of attenuation bands centered at discrete resonance wavelengths.

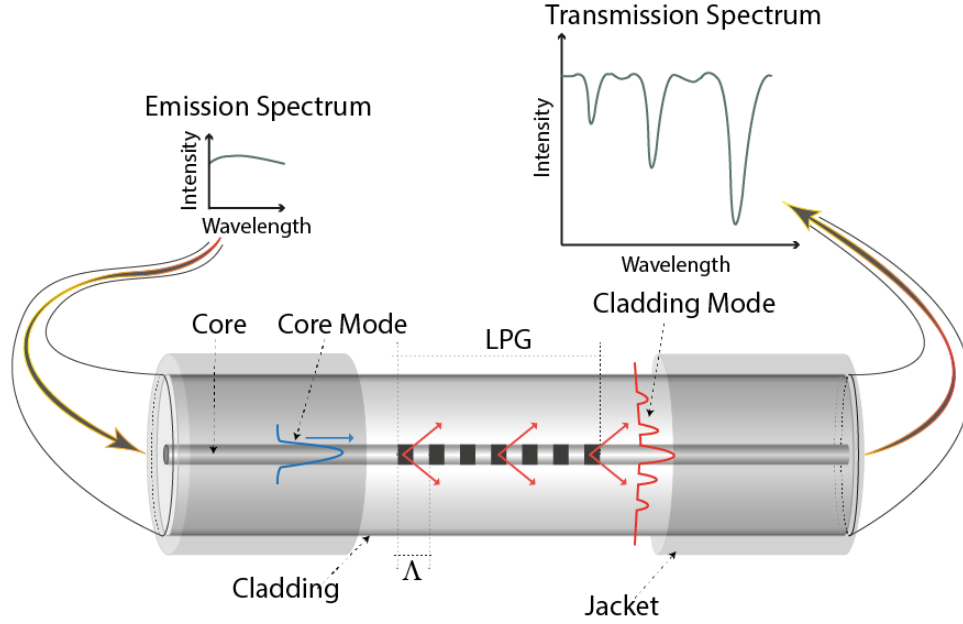


Figure 2-1. Schematic of an LPG

Each attenuation band corresponds to the coupling between a core and a cladding mode of a specific order that satisfies the phase matching condition given by [55]:

$$\lambda_{\text{res}}^i = \left[ n_{\text{eff,co}}(\lambda) - n_{\text{eff,cl}}^i(\lambda) \right] \Lambda, \quad (2.1)$$

where  $\lambda_{\text{res}}^i$  is the  $i$ th resonance wavelength,  $n_{\text{eff,co}}(\lambda)$  is the effective RI of the core mode,  $n_{\text{eff,cl}}^i(\lambda)$  is the effective RI of the  $i$ th cladding mode and  $\Lambda$  is the period of the grating. The depth of the attenuation bands in the transmission spectrum is given by [55]:

$$T_i = 1 - \sin^2(\kappa_i L), \quad (2.2)$$

where  $L$  is the length of the LPG,  $\kappa_i$  is the coupling coefficient of the  $i$ th cladding mode and  $T_i$  is the minimum transmission of the attenuation band corresponding to the coupling between the core mode and the  $i$ th cladding mode.

Similar to FBGs, LPGs are sensitive to temperature and strain. The sensitivity to these parameters arises from both the material and the waveguide contributions [55]. The material contribution is related to the change in the difference between  $n_{\text{eff,co}}(\lambda)$  and  $n_{\text{eff,cl}}^i(\lambda)$  due to the thermo-optic effect. The waveguide contribution is related to the change of the grating period. The sensitivity to temperature and strain is dependent on the period, order of the cladding mode and fibre composition.

Unlike FBGs, LPGs are sensitive to changes in the SRI due to its dependence on  $n_{\text{eff,cl}}^i(\lambda)$ . This dependence leads to three different cases, each of which has a unique sensor response [85].

Case 1 -  $\text{SRI} < n_{\text{cl}}$ : The condition of total internal reflection (TIR) is satisfied. As the SRI increases, the value of  $\lambda_{\text{res}}^i$  decreases as shown in Figure 2-2. The value of  $n_{\text{eff,co}}(\lambda)$  is independent of the SRI because the fundamental core mode is well confined in the fibre core. The value of  $n_{\text{eff,cl}}^i(\lambda)$  is dependent on the SRI because of the evanescent field of the cladding modes around the optical fibre surface. The value of  $n_{\text{eff,cl}}^i(\lambda)$  increases with the increase of SRI, and thus the difference between effective RIs decreases which leads to the decrease of  $\lambda_{\text{res}}^i$  (Equation 2.1). The maximum sensitivity occurs when the SRI approaches the RI value of the cladding (see Figure 2.2).

Case 2 -  $\text{SRI} = n_{\text{cl}}$ : The cladding is considered to be infinite, and thus the fibre supports no discrete cladding modes. As a consequence, the fundamental core mode couples to the

continuum of radiation modes and the attenuation bands in the transmission spectrum disappear.

Case 3 -  $SRI > n_{cl}$ : The cladding modes no longer undergo TIR. Instead, the fundamental core mode couples to a new set of cladding modes referred to as leaky modes. Part of the energy of each leaky mode is reflected at the interface between the cladding and the surrounding medium according to Fresnel reflection. As a consequence, the attenuation bands reappear in the transmission spectrum; however,  $\lambda_{res}^i$  is located at higher wavelengths compared to Case 1 (see Figure 2.2). As it can be observed in Figure 2.2, the resonance wavelength is approximately constant for RIs higher than 1.48 [55]. Therefore, the dependence of  $\lambda_{res}^i$  with SRI is much smaller in Case 3 compared to Case 1.

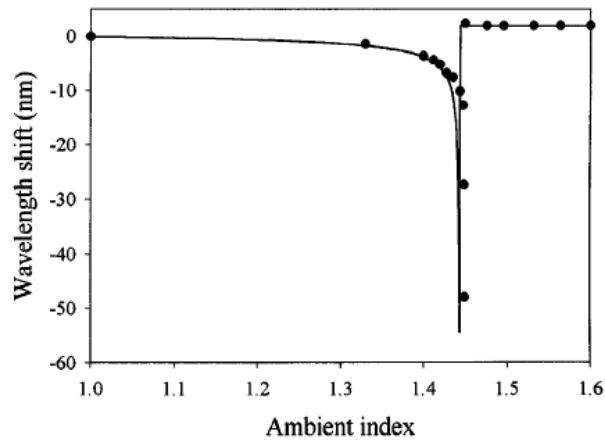


Figure 2-2. SRI characterization of a typical LPG. Reprinted with permission from [86].  
Copyright 1997 The Optical Society

This dissertation is focused on RI measurements in the low SRI range for monitoring CO<sub>2</sub> storage. Detection of CO<sub>2</sub> leakage at shallow depths requires sensors with high sensitivity at the RI of 1.0. At subsurface depths, the RI range of interest is between the RI of CO<sub>2</sub> (*i.e.* 1.18) and the RI of water (*i.e.* 1.335) [44]. As shown in Figure 2-2, the

sensitivity of a typical LPG operating at the SRI range between 1.0 and 1.335 is relatively low (*i.e.* less than 50 nm/SRI).

A number of approaches have been proposed to increase the sensitivity of LPGs at low SRIs. These include etching the fibre [87], designing LPGs that promote coupling between the core mode and a specific cladding mode at the dispersion turning point (DTP) [88], and coating the fibre [41].

Fibre etching leads to a shift of the optical field of the cladding modes towards the radial edge of the fibre [87]. This leads to the increase of the intensity of the evanescent field that penetrates in the surrounding medium, and thus, increases the sensitivity of the LPGs. The increase of sensitivity occurs predominantly at high SRIs, and is gradually shifted towards low SRIs as the fibre diameter is further reduced. Iadicicco *et al.* investigated the RI sensitivity of LPGs for various fibre diameters [89]. These authors show that the reduction of the fibre diameter from 125  $\mu\text{m}$  to 100  $\mu\text{m}$  only increases the sensitivity at SRIs higher than 1.38. The etching of the fibre to a diameter of 21  $\mu\text{m}$  leads to a sensitivity gain of 5 at an SRI range between 1 – 1.33 [89]. However, this increase of RI sensitivity is lower than the sensitivity of LPGs designed to operate at the DTP or coated LPGs.

The DTP of an LPG corresponds to the resonance wavelength at which the phase matching curves of the cladding modes exhibit a transition between a positive and a negative slope [90]. This behavior is illustrated in Figure 2-3 with the DTPs represented by the open circles. For a given SRI, an LPG can be designed to operate at the DTP by an appropriate selection of the grating period which results in a cladding mode at a selected wavelength range. An LPG operating at the DTP has a broadband attenuation band (*i.e.* approximately 100 nm) relative to an LPG operating away from the DTP (*i.e.*

approximately 10 nm). The broadband attenuation band splits into two attenuation bands for SRIs higher than that corresponding to the DTP. Two methods have been reported to use the DTP for RI measurements [88]. The first method is to monitor the depth of the attenuation band of an LPG operating at the DTP. However, this approach is hindered by the amplitude noise induced by thermal variations of the optical interrogation systems [91]. The second method is to monitor the wavelength separation between each attenuation band for an LPG operating near the DTP. Biswas *et al.* reported a sensitivity of 1847 nm/SRI using the second monitoring method [88]. However, the disadvantage of this approach is the wide separation between the two attenuation bands (*i.e.* wider than 100 nm). This limitation prevents the utilization of most of the available optical interrogators which have a wavelength range of less than 90 nm.

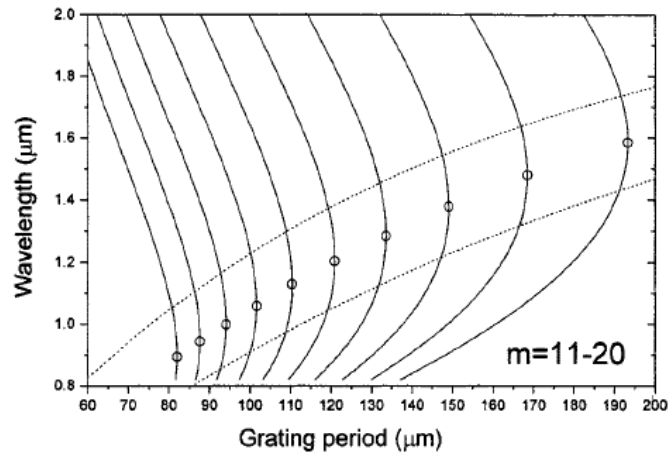


Figure 2-3. Plot of resonance wavelength as a function of grating period for coupling between core mode and cladding modes of order  $m=11$  (curve on the right hand side) to  $m=20$  (curve on the left hand side). © 2002 IEEE [88].

Additionally, the attenuation bands of LPGs operating near the DTP have large width. This possesses a challenge for software algorithms to continuously track the central wavelength of each attenuation band as the SRI changes over time. Finally, the fabrication

of LPGs operating near the DTP at a target wavelength and SRI is challenging due to limitations of the fabrication methods [88]. For instance, the attenuation bands of LPGs written by UV-irradiation in hydrogen loaded fibres shift after inscription due to hydrogen outgassing. Other fabrication methods including systems based on femtosecond laser, CO<sub>2</sub> laser, and electric arc-discharge, have poor control to induce repeatable RI modulations in the fibre core. As consequence, the inscription of LPGs as theoretically modeled is challenging. Researchers have overcome this disadvantage by writing LPGs away of the DTP and using post-processing etching to reduce the diameter of the cladding to tune the LPG at or near the DTP [88].

In the last decade, coating of LPGs has attracted special attention as an alternative method to increase the sensitivity of the LPGs at different SRIs, without the requirement for fibre etching [92].

Two different coating approaches have been explored by various authors. In the first approach, a coating can be selected to react with a target chemical species, responding by swelling and/or changing its RI. Examples of this approach include: LPGs coated with palladium by DC magnetron sputtering for hydrogen detection [93]; LPGs coated with gelatin [94] or polyimide [95] by dip-coating to measure humidity; LPGs coated with zeolites by hydrothermal synthesis for detection of organic vapors [96]; LPGs coated with zinc oxide nanorods by pulsed laser deposition combined with aqueous chemical growth to detect ethanol vapor [97]; and LPGs coated with silica nanoparticles by electrostatic self-assembly to monitor the concentration of ammonia [98].

The second approach consists of coating an LPG with a material that has a higher RI than silica promoting a phenomenon referred to as *transition mode* [41], [99], [100]. This

behavior is illustrated in Figure 2-4 for an LPG coated with polystyrene (RI of 1.59). Referring to Figure 2-4, as the SRI increases, the resonance wavelength of mode LP<sub>08</sub> decreases until it approaches the resonance wavelength of mode LP<sub>07</sub> at the SRI of air (*i.e.* original resonance wavelength). Similarly, the resonance wavelength of mode LP<sub>07</sub> decreases until it approaches the original resonance wavelength of mode LP<sub>06</sub>, and so on. This phenomenon is due to the coupling of the lowest order cladding mode (*i.e.* mode LP<sub>02</sub>) to the coating [101]. This relocation of mode LP<sub>02</sub> causes a reorganization of the remaining cladding modes. During the mode reorganization, higher order cladding modes than those guided by the coating shift their resonance wavelength toward the original resonance wavelength of the immediate lower order cladding mode [99].

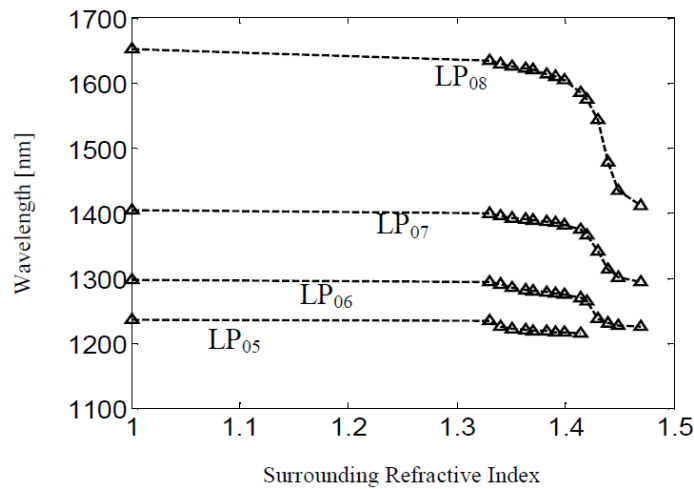


Figure 2-4. Wavelength shift as a function of the SRI for different modes of an LPG coated with 150 nm layer of polystyrene, Reprinted with permission from [101].

Copyright 2005 The Optical Society

The mode reorganization occurs within a narrow SRI range which is referred to as the *transition region* [101]. The RI sensitivity of a coated LPG operating in the transition region is significantly higher than the sensitivity of a bare LPG.

The sensitivity of a coated LPG at a given SRI depends on the coating parameters (RI and thickness of the coating material) and the order of the cladding mode [101]. For a given RI and thickness of the coating, there is a unique value of SRI at which the transition point of a cladding mode occurs (*i.e.* transition point). Therefore, for a target SRI measurement, it is possible to tune the thickness of the coating to maximize the sensitivity of an LPG.

Various coating methods and materials have been investigated to promote transition mode behavior of LPGs. This phenomenon was originally reported by Rees *et al.*, who used the Langmuir-Blodgett method to coat an LPG with tricosenoic acid [41]. This coating method has been mostly used to develop coated LPGs for detection of volatile organic compounds. For instance, Partridge *et al.* reported an LPG coated with calixarene for detection of toluene for use in water contamination [102]. Disadvantages of this method include: the requirement of expensive equipment to allow for constant surface pressure of the Langmuir monolayer during coating, limited choice of coating materials, and relative weak adhesion of the coating to the optical fibres.

Electrostatic self-assembly (ESA) has been used to deposit polymers [103] and silica nanoparticles [104] on LPGs. Although ESA allows control of coating thickness and follows a relatively simple fabrication process, the coatings show weak adhesion to the optical fibre in aqueous solutions. Therefore, this coating has been mostly used to develop gas sensors for atmospheric measurements. For instance, Wang *et al.* reported LPGs coated with polyelectrolytes by ESA for detection of ammonia for use in diagnosis of human respiratory diseases [105].

The dip-coating method has been used to coat LPGs with polystyrene [101]. Dip-coating is a low cost and practical method that does not require special equipment. This method has been successfully used to increase the sensitivity of LPGs in the vicinity of water [43], [106]. For example, Pilla *et al.* reported an LPG coated with polystyrene with a RI sensitivity of approximately 1500 nm/SRI [106]. This group has also developed polystyrene coated LPGs to monitor binding of specific proteins to the surface of the grating for biochemical applications [107]. The disadvantage of the dip-coating method is the lack of precision to control coating thickness. As a consequence, the fabrication of sensors with maximum sensitivity at a target SRI using the dip-coating method is challenging.

Vapor precursor based methods have been used to deposit different coatings on LPGs. Smietana *et al.* investigated LPGs coated with silicon nitride [108] and diamond-like coatings [109] by radio-frequency plasma chemical vapor deposition (CVD). This group reported a sensitivity of approximately 300 nm/SRI at the RI of water for an LPG coated with diamond-like coating [110]. Coelho *et al.* investigated LPGs coated with titanium dioxide (TiO<sub>2</sub>) by thermal evaporation [111]. The focus of this group has been the development of highly sensitive sensors for the high SRI range (*i.e.* higher than 1.45). The sensors developed by Coelho *et al.* have been applied to monitor the concentration of organic solvents in edible oils for food processing control [111]. There are two main disadvantages of CVD and thermal evaporation. First, these deposition methods are directional and are, therefore, well suited for coating flat substrates. However, control of coating thickness on optical fibres is challenging using these directional deposition methods [112], [113]. Secondly, the high deposition temperature required by these methods

might constitute a risk of thermal degradation of LPGs written by UV irradiation. This has been shown in a study that compares the deposition of silicon nitride performed by CVD on LPGs written by UV irradiation with LPGs written by electric arc discharge [114].

ALD has recently been used to deposit aluminium oxide ( $\text{Al}_2\text{O}_3$ ) on LPGs [115], [116]. Smietana *et al.* reported a sensitivity value of 1850 nm/SRI in the SRI range between 1.3330 – 1.3420 [115]. ALD is non-directional, and thus, offers the potential to achieve high control of coating thickness on complex substrates such as optical fibres.

Recently, a number of studies have shown that the sensitivity of LPGs can be further increased by combining the DTP with transition modes. This has been used to increase the sensitivity of LPGs operating at the RI of water. Pilla *et al.* reported a sensitivity of 9100 nm/SRI for an LPG coated with polystyrene by the dip-coating method [117]. Smietana *et al.* reported a sensitivity of 6200 nm/SRI for an LPG coated with  $\text{TiO}_2$  by ALD [118]. Villar reported a numerical study which shows that an LPG can be potentially tuned to have a sensitivity of  $143 \times 10^3$  nm/SRI [119].

## **2.2 Mach-Zehnder interferometers**

A basic MZI comprises a structure that splits the incident light into two optical paths, and after a certain fibre length, recombines the two optical paths in one path in the forward propagation direction [38].

Several techniques have been proposed to fabricate MZIs with RI sensitivity. Examples include the inscription of two LPGs in-line [120], tapering of single-mode fibre [121], lateral offset splicing [122], core diameter mismatch [123], fibre peanut-shape structure [124], and laser irradiated points [125]. Schematics of these MZI configurations are illustrated in Figure 2-5.

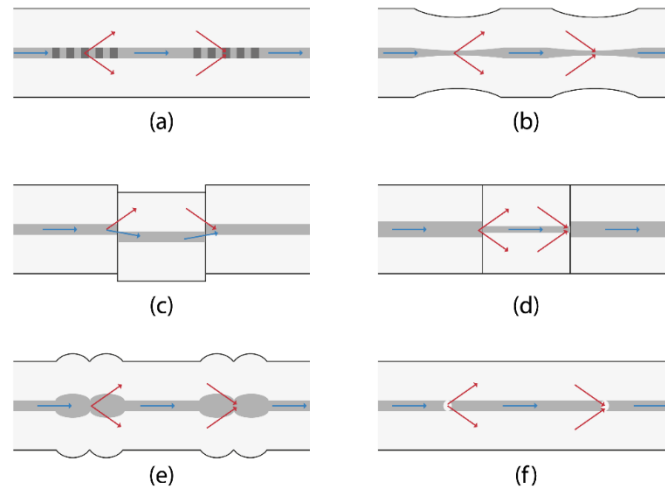


Figure 2-5. Different MZI configurations for RI measurements, fabricated by (a) two LPGs in-line; (b) single-mode fibre tapering; (c) lateral offset splicing; (d) core diameter mismatch; (e) fibre peanut-shape structure; (d) laser irradiated points

Another technique to fabricate MZIs is to use PCF as the active region of the sensor [62], [126]. PCF was introduced by Knight *et al.* in 1996 and consists of a pure silica fibre which incorporates a periodic array of cylindrical voids (*i.e.* holes) aligned parallel to the fibre axis [127]. PCF can be fabricated with a solid silica core or with a hollow core (see Figure 2-6).

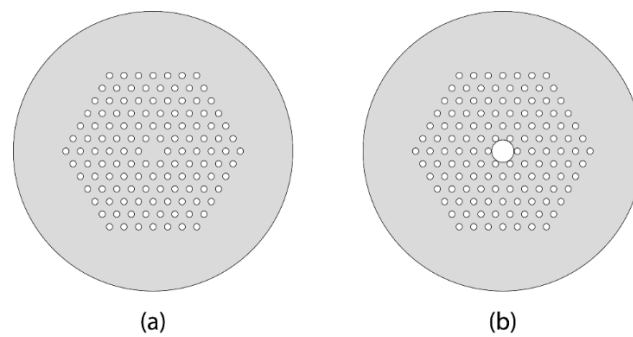


Figure 2-6. (a) solid core and (b) hollow core photonic crystal fibre

In solid core PCF, the air holes located in the cladding region create a cladding in which the average RI is lower than that of the solid core. Similar to SMF, solid core PCF allows

light guidance in the core by TIR. Hollow core PCF comprises an air hole aligned with the central axis of the fibre in addition to the air holes in the cladding region. This type of PCF allows light guidance in the core by a different guiding mechanism referred to as the *band gap effect*. For further details about the band gap effect on hollow PCF the reader is referred to the reference [128]. Hollow core PCF has not been investigated in this work, and thus the term PCF is used to refer to a solid core PCF.

Three different methods have been proposed to fabricate sensors based on PCF, namely by tapering the PCF segment [129], by splicing a PCF with a lateral offset between SMFs, and by collapsing the air holes of the PCF spliced in-line between the SMFs (*i.e.* without offset) [54]. The air hole collapsing method is investigated in this research and this sensor is referred to as *PCF interferometer*. This method comprises a simple fabrication process and the sensors are more robust relative to the other two methods.

A PCF interferometer is fabricated by splicing a segment of a PCF between a lead-in and lead-out SMF. The time and intensity of the electric arc of the fusion splicer are set to collapse the holes of the PCF at the splicing regions. At the first splice, the core mode of the SMF is diffracted by the region of the collapsed holes and couples to the core mode and cladding modes of the PCF [126]. At the second splice, the SMF acts as a spatial filter because it only supports a core mode, and thus the core mode and the cladding modes of the PCF are recombined and coupled to the core mode of the SMF [126]. An illustration of this sensor is provided in Figure 2-7.

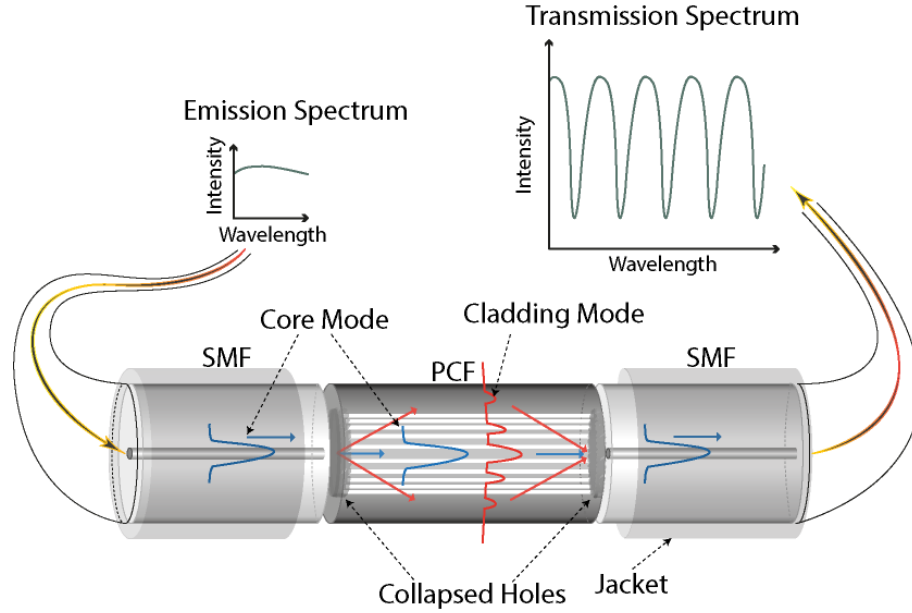


Figure 2-7. Illustration of a PCF interferometer

The core mode and the cladding modes of the PCF accumulate a phase difference due to the difference between the effective RI of each mode. This phase difference leads to an interferometric behaviour between the two modes and, as a consequence, the transmission spectrum exhibits an interference pattern (see Figure 2-7). The transmission spectrum for the interference between a core and a cladding mode is given in Equation 2.3:

$$T(\lambda) = I_{co}(\lambda) + I_{cl}(\lambda) + 2 \left[ I_{co}(\lambda) I_{cl}(\lambda) \right]^{\frac{1}{2}} \cos(\delta\phi), \quad (2.3)$$

where  $T(\lambda)$  is the transmission signal,  $I_{co}(\lambda)$  and  $I_{cl}(\lambda)$  are the intensities of the core and cladding modes, respectively, and  $\delta\phi$  is the phase difference between the modes. The phase difference between the two modes can be expressed as following:

$$\delta\phi = \frac{2\pi\Delta n_{eff}L}{\lambda}, \quad (2.4)$$

where  $\Delta n_{\text{eff}}$  is the difference between the effective RI of the core mode ( $n_{\text{eff,co}}$ ) and cladding modes ( $n_{\text{eff,cl}}$ ),  $L$  is the length of the PCF segment and  $\lambda$  is the incident wavelength. The maximum intensity occurs for constructive interference when:

$$\frac{2\pi\Delta n_{\text{eff}}L}{\lambda} = 2m\pi, \quad (2.5)$$

where  $m$  is an integer. The separation between two consecutive peaks, *i.e.* free spectral range (FSR), is given by:

$$\text{FSR} = \frac{\lambda^2}{\Delta n_{\text{eff}}L}. \quad (2.6)$$

From Equation 2.6 it can be observed that the increase of  $L$  leads to the decrease of the FSR. As a consequence of the decrease of FSR, the full width at half maximum (FWHM) decreases. Therefore, the increase of  $L$  leads to an increase in sensor resolution. However, the number of fringes in the transmission spectrum is another important factor when designing PCF interferometers. As the FSR increases, the total number of fringes at a given wavelength range also increases. Depending on the dynamic range on which the sensor is designed to operate, the interrogation of PCF interferometers with long PCF lengths may become more complex as the fringes overlap due to the wavelength shift of the interference pattern.

The RI sensitivity of PCF interferometers arises from the dependence of the effective RI of the cladding  $n_{\text{eff,cl}}$  on the SRI into which the evanescent field of the cladding mode extends [62]. The SRI change leads to the change of  $\Delta n_{\text{eff}}$ , and thus, leads to the wavelength shift of the interference pattern. Therefore, SRI can be measured by tracking the maximum (*i.e.* peak) or minimum (*i.e.* valley) of the interference pattern.

The wavelength shift of the interference pattern of a PCF interferometer is shown in Figure 2-8 as a function of SRI [130].

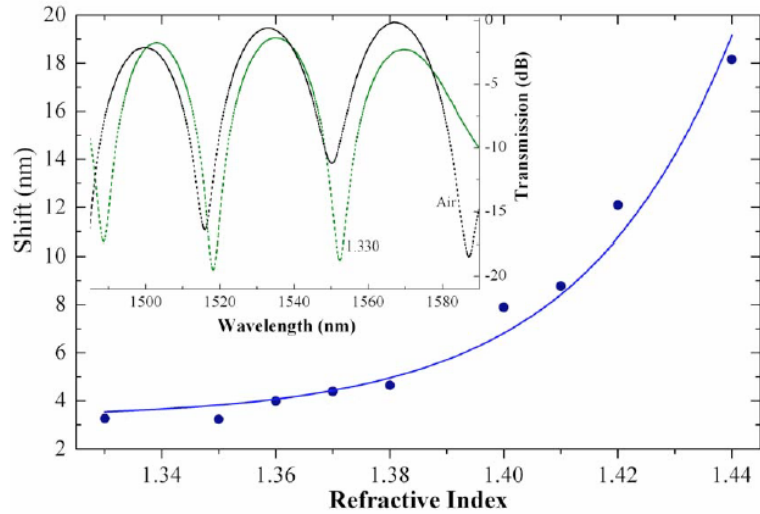


Figure 2-8. Characterization of a PCF interferometer to SRI changes. Reprinted with permission from [130]. Copyright 2009 The Optical Society

The wavelength of the interference pattern of the PCF interferometer increases with the increase of SRI. This behavior is explained by analyzing the constructive or destructive interference in a PCF interferometer. Considering constructive interference as an example (Equation 2.5),  $\delta\phi$  is directly proportional to  $\Delta n_{\text{eff}}$  and to  $L$ , and is inversely proportional to  $\lambda$ . Similarly to LPGs,  $n_{\text{eff,co}}$  is not influenced by the SRI because the core mode is well confined in the core of the PCF. However, the value of  $n_{\text{eff,cl}}$  increases with the increase of SRI leading to the increase of  $\Delta n_{\text{eff}}$ . Considering that the only parameter to which  $\delta\phi$  is inversely proportional is  $\lambda$ , this latter parameter must increase as the SRI increases for the condition of constructive interference to remain valid. The same explanation is applied for the analysis of destructive interference.

The sensitivity of a PCF interferometer increases as SRI increases and the maximum sensitivity occurs when the SRI is close to the RI of silica (*i.e.* 1.455). At an SRI range between 1.33 – 1.38, the sensitivity is approximately 100 nm/SRI and at an SRI range between 1.38 – 1.46 the sensitivity is approximately 700 nm/SRI [62]. For SRIs higher than silica, the condition of TIR is not satisfied and the cladding modes are converted into radiation modes. In this case, the interference pattern is not observed.

The sensitivity of a PCF interferometer at low SRIs can be increased by partial etching of the PCF segment or by applying fibre coatings. Zhao *et al.* reported a sensitivity value of 252 nm/SRI at the RI of water by etching the PCF with a diameter of 125  $\mu\text{m}$  to 87  $\mu\text{m}$  [131]. However, the sensitivity gain achieved by fibre etching method is lower than that achieved by the coating method.

Similarly to LPGs, two different approaches have been used for fibre coating. The first approach consists of coating PCF interferometers with a material that reacts with target species by swelling and/or changing its RI. This method has been explored to develop humidity sensors. Examples include, PCF interferometer coated with Agarose by the dip-coating method [132]; and PCF interferometer coated with polyvinyl alcohol by the dip-coating method [133].

The second approach consists of coating PCF interferometers with a material that has a RI greater than the RI of silica. This has been shown only by Smietana *et al.* using radio frequency plasma enhanced CVD to coat PCF interferometers with silicon nitride [42]. The coating shifts the distribution of the light field of the cladding mode towards the outer radial edge of the PCF, increasing the energy density in this region [42]. This leads to an increase in the intensity of the evanescent wave that penetrates into the surrounding medium. This

increases the RI sensitivity of a coated PCF interferometer relative to a bare device. Smietana *et al.* reported a sensitivity value of 874 nm/SRI for a coated PCF interferometer operating at an SRI in the vicinity of water [42].

### **2.3 Summary**

This chapter discusses FOSs for RI measurements, with a special focus on the sensors investigated in this research: LPGs and PCF interferometers. The key characteristics of these sensors include mechanical robustness, optical stability and the possibility to enhance the sensor performance by applying high-RI coatings. A summary of the sensitivity, merits and drawbacks of the RI-based FOSs discussed in Chapter 2 is presented at the end of this section in Table 2.1.

Background information of LPGs and PCF interferometers is organized in Section 2.1 and Section 2.2, respectively. Both sections start with the description of fundamental concepts of the sensors. The RI sensitivity of the sensors to SRI changes is then discussed in detail. LPGs and PCF interferometers have low sensitivity at the SRI range of interest for CO<sub>2</sub> monitoring in downhole conditions (*i.e.* between 1.0 – 1.335). However, there are methods that allow for the increase of the RI sensitivity in this SRI range. One of the methods that has attracted special attention over the last decade is the coating of the sensors with materials that have an RI higher than silica.

The current coating methods and materials available in the literature to coat LPGs and PCF interferometers are discussed in Section 2.1 and 2.2, respectively. Among these coating methods, dip-coating has shown potential to achieve high sensitivities by coating LPGs with polystyrene. Additionally, dip-coating is a low cost and practical method that does not require special equipment. However, the lack of precision to control the coating

thickness at the nanometer scale hinders the development of sensors with maximum sensitivity at a target SRI. ALD is the method that offers the potential to achieve the highest control over coating thickness on optical fibre coatings.

The maximum sensitivity obtained for LPGs coated with polystyrene using the dip-coating method and with Al<sub>2</sub>O<sub>3</sub> using ALD is 1500 nm/SRI and 1850 nm/SRI, respectively, at an RI of 1.335. The maximum sensitivity obtained for a coated PCF interferometer is 874 nm/SRI coated with silicon nitride using radio frequency plasma enhanced CVD. Assuming a resolution of 1 pm as specified by commercial optical interrogators, the maximum RI resolutions of coated LPGs and coated PCF interferometer are  $5 \times 10^{-7}$  and  $1 \times 10^{-6}$ , respectively. As shown in Section 1.2, *Review of fibre-optic sensors for CO<sub>2</sub> detection*, these RI resolution values are higher than the expected RI changes in water with low concentration of CO<sub>2</sub> at high pressure (*i.e.*  $1.15 \times 10^{-5}$ ). The results of coated LPGs and PCF interferometers published in the literature suggest that these sensors are promising candidates for CCS applications.

The combination of transition mode behavior with the DTP of LPGs is expected to further increase the RI sensitivity. However, this approach requires the control of coating thickness with high precision to achieve high performance at a target SRI and within a desired wavelength range. This is further discussed in Future Work presented in Chapter 4.

The details of the development of coated of LPGs and PCF interferometers for CCS applications are presented in Chapter 3.

**Table 2-1. Summary of RI-based FOSs**

| Configuration                              | RI Sensitivity in water ( <i>i.e.</i> RI of 1.335) | Merits  | Drawbacks  |
|--|--|---|--|
| <b>Conventional RI sensors</b>             |  |   |  |
| Fibre tapers                               | 1656 nm/SRI [65]                                   | Relatively easy to fabricate  | Trade-off between sensitivity and robustness   |
| Etched FBGs                                | 92 nm/SRI [134]                                    | Commercially available, multiplexing capabilities   | Trade-off between sensitivity and robustness, acid handling  |
| TFBGs                                      | 11 nm/SRI [135]                                    | Multi-parameters sensing, intrinsic RI sensitivity, mechanical robustness   | High polarization dependence, complex demodulation methods, low RI sensitivity at low SRIs               |
| LPGs                                       | 40 nm/SRI [136]                                    | Commercially available, intrinsic RI sensitivity, low polarization dependence, simple demodulation methods, mechanical robustness | High temperature dependence, low RI sensitivity at low SRIs  |
| FPIs                                       | 851 nm/SRI [75]<br>1163 nm/SRI [74]                | Low temperature dependence, well-suited for gas monitoring  | Complex fabrication methods, high insertion losses, brittle, increased losses in the presence of liquids |
| MIs  | 27 nm/SRI [137]<br>274 nm/SRI [138]                | Interrogation in reflection   | Low sensitivity at low SRIs  |
| MZIs                                       | 50 nm/SRI [124]<br>100 nm/SRI [62]                 | Low-cost sensors, simple fabrication methods, mechanical robustness   | High sensitivity to strain, low sensitivity at low SRIs  |
| <b>RI sensor with enhanced sensitivity</b> |  |   |  |
| LPGs near DTP                              | 1847 nm/SRI [88]                                   | High RI sensitivity at low SRIs   | Wide separation between valleys, attenuation bands with large bandwidth, complex fabrication             |
| Coated LPGs                                | 1500 nm/SRI [106]<br>1850 nm/SRI [115]             | High RI sensitivity at low SRIs, mechanical robustness  | High sensitivity to temperature  |
| Coated LPGs near DTP                       | 6200 nm/SRI [118]<br>9100 nm/SRI [117]             | High RI sensitivity at low SRIs   | Wide separation between valleys, attenuation bands with large bandwidth, complex fabrication             |
| Coated PCF interferometers                 | 874 nm/SRI [42]                                    | High RI sensitivity at low SRIs, mechanical robustness  | High sensitivity to strain   |

## Chapter 3: Contributions

### Introduction

This dissertation presents four studies which resulted in significant contributions that are organized into four manuscripts included in Appendices A through D. This chapter provides an overview of the motivation, methods and key results for each study.

As presented in Section 1.1, *Overview of monitoring methods applied in geological CO<sub>2</sub> storage*, monitoring geological CO<sub>2</sub> storage requires measurements of CO<sub>2</sub> concentrations at atmospheric, near-surface and deep-subsurface depths. At atmospheric and near-surface depths, potential leaks of CO<sub>2</sub> are expected to be in the gas phase. The target RI for detection of CO<sub>2</sub> concentrations in gas environments is 1.0. At deep-subsurface depths, CO<sub>2</sub> is in the liquid or supercritical phase. The target RI for detection of CO<sub>2</sub> concentrations in water is approximately 1.335.

As presented in Section 2.1, *Long period gratings*, and in Section 2.2, *Mach-Zehnder interferometers*, the sensitivity of LPGs and PCF interferometers at a target SRI can be increased by coating the sensors with high-RI materials. Coating methods that offer precise control over coating thickness allow development of RI sensors with maximum performance at a target SRI.

This research aims to develop sensors for both atmospheric and deep-subsurface environments. The transition mode behavior of LPGs coated with polystyrene by the dip-coating method is explored to develop sensors with high sensitivity at target SRIs. This is achieved by investigating the coating thickness that increases the sensitivity of LPGs at the

RI of 1.0 and at the RI of 1.335. Additionally, ALD is investigated to achieve higher precision of coating thickness than that obtained by the dip-coating method. This new deposition method is applied to develop highly sensitive LPGs and PCF interferometers to operate at the RI of 1.335.

The order of the sections in this chapter present the logical progression of this research. Section 3.1 and Section 3.2 present the study of coated LPGs to monitor concentrations of CO<sub>2</sub> at atmospheric pressure and dissolution of CO<sub>2</sub> at high pressure (*i.e.* 1400 psi), respectively. Section 3.3 and Section 3.4 present the study of ALD to coat LPGs and PCF interferometers with HfO<sub>2</sub>, respectively.

### **3.1 Highly sensitive coated long period grating sensor for CO<sub>2</sub> detection at atmospheric pressure<sup>1</sup>**

The objective of this study is to investigate the transition mode behavior of LPGs, focusing specifically on increasing the sensitivity at low SRIs to develop sensors for monitoring CO<sub>2</sub> at low pressure.

As the lead student in this study, my role was to: coat LPGs, characterize the coatings by measuring coating thickness, characterize the RI behavior of the sensors, develop lab testing protocols, test the sensors with CO<sub>2</sub>, perform data analyses, and prepare the manuscript. The co-authors of this manuscript designed and fabricated the test rigs, conducted sensor tests and provided editorial input for the manuscript.

As discussed in Section 1.1, current MVA technology for monitoring CO<sub>2</sub> storage at shallow depths have several limitations including the inability to continuously monitor CO<sub>2</sub>

---

<sup>1</sup> Manuscript published in Sensors and Actuators B: Chemical

*in-situ*. Although a number of FOS for monitoring CO<sub>2</sub> have been proposed showing high resolution, the majority of these studies are based on fluorescence and absorption based sensors which have limitations when applied to monitor CO<sub>2</sub> storage (see Section 1.2). The dyes used in fluorescence based sensors tend to leach leading to erroneous signals and absorption based sensors are limited by the difficulty in interpreting complex spectral absorption bands of different gases and multi-fluids present in downhole environments. These limitations can be overcome by coated LPGs, to which the key features are the intrinsic sensitivity to SRI without the need for etching the fibre and the possibility of tuning the coating thickness to increase the sensitivity at a target SRI.

The transition mode phenomenon has been widely investigated as discussed in Chapter 2. In this study, the transition mode behavior was investigated to increase the sensitivity of LPGs in the low range of SRI to monitor gases at atmospheric pressure which have RIs of approximately 1.0. This is the first study of a coated LPG to monitor CO<sub>2</sub> based on transition mode behavior. In this study, data from a number of cycles between N<sub>2</sub> and CO<sub>2</sub> as well as for different CO<sub>2</sub> concentrations is provided. This is the first time that these gases are measured in a cyclic fashion using LPGs. This type of experiment demonstrates the potential of coated LPGs for continuous monitoring of CO<sub>2</sub>.

The dip-coating method was used to coat the fibre with polystyrene to promote transition mode behavior on LPGs. The RI of bulk polystyrene is 1.59 which is higher than that of the cladding (*i.e.* RI of 1.455), as required to promote transition modes on LPGs. Three LPGs with different coating thicknesses were investigated in this study, namely 204 nm, 249 nm and 365 nm, which were labeled in the manuscript as LPG2, LPG3, and LPG4 [139]. The transition point of LPG2 and LPG3 occur at RI values of 1.4482 and 1.4224,

whereas the coating thickness of LPG4 was tuned to provide transition at a low SRI, which results in higher sensitivity at the RI of gases. The performance of the three coated LPGs and a bare LPG (labeled as LPG1) was compared to monitor injections at atmospheric pressure between N<sub>2</sub> and CO<sub>2</sub> as well as different CO<sub>2</sub> concentrations.

The results show that LPG4 was able to distinguish between N<sub>2</sub> and CO<sub>2</sub> with good reproducibility and reversibility whereas the other LPGs were virtually insensitive to the cycling between these gases. The sensitivity of LPG4 to CO<sub>2</sub> concentrations was shown to be 1.23± 0.08 pm/%CO<sub>2</sub>.

However, the key result of this manuscript in the context of this dissertation was the understanding that CO<sub>2</sub> interacts with the polystyrene coating and amplifies the sensor response. The sensitivity of LPG4 to CO<sub>2</sub> and N<sub>2</sub> was significantly higher than that predicted by the pre-calibration of this sensor with glycerin solutions. This result suggests that the wavelength shift is not solely due to the change of SRI, but is also likely due to sorption of CO<sub>2</sub> by the polystyrene coating which leads to a change of RI of the coating.

Insights from this study are important to understand interaction of CO<sub>2</sub> with polystyrene in more complex experiments such as monitoring CO<sub>2</sub> at high pressure.

A more complete description of this study is presented in [139], which is included here as Appendix A.

### **3.2 Experimental investigation of long-period grating transition modes to monitor CO<sub>2</sub> in high-pressure aqueous solutions<sup>2</sup>**

The objectives of this study are the investigation of transition mode behavior to increase the sensitivity of coated LPGs at the SRI of water (*i.e.* around 1.33) and to perform the first measurement of dissolution of CO<sub>2</sub> in water at high pressure with a coated LPG.

As the lead student in this study, my role was to: coat LPGs, characterize the coatings by measuring coating thickness, characterize the RI behavior of the sensors, develop lab testing protocols, test the sensors with CO<sub>2</sub>, perform data analyses, and prepare the manuscript. The co-authors of this manuscript designed and fabricated the test rigs, conducted sensor tests and provided editorial input for the manuscript.

As discussed in Section 1.1, there are a number of techniques for deep-subsurface monitoring of CO<sub>2</sub> storage in geological formations including seismic, gravimetric and electromagnetic methods [4]. The main limitations of these methods are low resolutions, high costs and inability to monitor continuously over the long time scales of CCS projects.

Most of the reported FOSs for detection of CO<sub>2</sub> have only been tested at atmospheric pressures (see Section 1.2). Among these, fluorescence based sensors are not suited for monitoring geological storage of CO<sub>2</sub> due to leaching of the dye in the high pressure environment of subsurface storage sites, and absorption based sensors have only been demonstrated to measure CO<sub>2</sub> in a gas phase. Detection of CO<sub>2</sub> at high pressure has been demonstrated using a tip sensor approach based on SRI. However, this method is only suitable to monitor significant changes in SRI, for example to distinguish between different CO<sub>2</sub> phases. The utilization of fibre tip sensors to monitor dissolution of CO<sub>2</sub> in water is

---

<sup>2</sup> Manuscript published in Journal of Lightwave Technology

challenging due to the low RI sensitivity of these devices. More recently, a study led by Bao *et al.* demonstrated that bare LPGs are well suited to distinguish between brine and scCO<sub>2</sub> under carbon sequestration conditions [140]. This later study was co-authored by our research group, and established context and motivation for the work developed in this dissertation. The main limitation of the study reported in [140] is the low sensitivity of bare LPGs to monitor concentrations of scCO<sub>2</sub> in brine under tested conditions.

This study aims to develop a coated LPG sensor that addresses the limitations summarized above. The key contribution of this study is the application of transition mode behavior to monitor CO<sub>2</sub> at high pressure. This is the first study that reports continuous monitoring of dissolution of CO<sub>2</sub> in water at CCS conditions with a FOS.

The dip-coating method was used to coat LPGs with polystyrene. Coating thickness is a function of the withdrawal speed and the concentration of the polystyrene solutions (*i.e.* polystyrene dissolved in chloroform). The relationship between the concentration of the polystyrene solution and coating thickness was investigated using scanning electron microscopy (SEM) to measure coating thickness on fibre samples. LPGs coated with different concentrations of polystyrene solutions were tested to determine the coating thickness that allow enhanced sensitivity at the RI of water. The coated LPG with higher sensitivity was used to monitor dissolution of CO<sub>2</sub> in water at high pressure (*i.e.* 1400 psi) and the response was compared with a bare LPG.

The characterization of LPGs with glycerin solutions show that the highest sensitivity in the SRI range between 1.333 and 1.348 is 169 nm/SRI for an LPG with an estimated coating thickness 307.5 nm.

This coated LPG was successfully applied to measure CO<sub>2</sub> at high pressure. Under test conditions, the results of the coated LPG show that the dissolution of CO<sub>2</sub> in water takes approximately 7 hrs, corresponding to an increase of the wavelength shift of 5.144 nm. This test also confirms that a bare LPG does not have enough sensitivity to monitor concentrations of CO<sub>2</sub> in water. The CO<sub>2</sub> resolution of the coated LPG is estimated to be 15 ppm.

The results of CO<sub>2</sub> tests at high pressure show that the wavelength shift caused by dissolution of CO<sub>2</sub> in water was higher than expected, based on the sensor calibration in glycerin. These results are in agreement with the finding presented in Section 3.1. Again, this result is attributed to the SRI changes caused by the presence of CO<sub>2</sub>. In addition, the wavelength shift of the coated LPG is also attributed to the sorption of CO<sub>2</sub> by the polystyrene coating which changes the RI of the coating.

The utilization of dip-coating to develop CO<sub>2</sub> sensors based on polystyrene coated LPGs has two limitations. First, in typical transition mode behavior, LPGs cannot be coated to operate at the transition point (*i.e.* point of maximum sensitivity) because the depth of the attenuation bands are significantly reduced at this point [101]. The challenge with coated LPGs is to establish the coating thickness that gives the maximum sensitivity to the grating at a target SRI while the depth of the attenuation band is readily detectable [101]. This is difficult to achieve with the dip-coating method due to the limited control over coating thickness. Secondly, polystyrene has a relative weak adhesion to the optical fibres. This limitation is a constraint of the dip-coating method, associated with a weak chemical interaction between the coating and substrate. As a consequence, the sensors cannot be

mechanically cleaned without damaging the coating. To address these limitations, a new coating method and a suitable material is presented in Sections 3.3 and 3.4.

A more complete description of this study is presented in [48], which is included here as Appendix B.

### **3.3 Long period gratings coated with hafnium oxide by plasma-enhanced atomic layer deposition for refractive index measurements<sup>3</sup>**

The objective of this study is to investigate a new deposition method, plasma enhanced ALD (PEALD), to coat UV-written LPGs with HfO<sub>2</sub>. This deposition method addresses two limitations associated with dip-coating, as described in Section 3.2, *i.e.* inability to achieve fine control over coating thickness and weak coating adhesion to the optical fibre.

As the lead student in this study, my role was to: model LPGs using the software Optigrating, coat LPGs, characterize the RI behavior of the sensors, calibrate the RI behavior of the sensors, perform data analyses, and prepare the manuscript. The co-authors of this manuscript designed and fabricated the test rigs and provided editorial input for the manuscript.

In ALD, the reactions can be thermally activated typically at temperatures higher than 200 °C (*i.e.* thermal ALD) or supported by plasma (*i.e.* PEALD). Prior to this study, ALD has been investigated to coat LPGs by two different groups, Smietana *et al.* and Zou *et al.* These authors used thermal ALD to coat LPGs, written by electric arc-discharge [115] and by CO<sub>2</sub> laser [116], with Al<sub>2</sub>O<sub>3</sub>. LPGs written by these two methods are stable at

---

<sup>3</sup> Manuscript published in Optics Express

temperatures higher than 700 °C, and thus the deposition temperature of thermal ALD does not constitute a risk for grating degradation. However, LPGs written by UV-irradiation start to show thermal degradation at approximately 150 °C which then requires the decrease of the ALD temperature.

PEALD is a suitable method for coating UV-written LPGs because it can be performed at low temperatures while also maintaining shorter purge times than are required in thermal ALD to achieve uniform coating thickness.

This study comprises modeling and experimental work of LPGs coated with HfO<sub>2</sub> by PEALD. Modeling was carried out using the software Optigrating™ to determine the thickness range of HfO<sub>2</sub> that promotes transition mode behavior of LPGs. LPGs were coated with three different coating thicknesses namely 30 nm, 50 nm and 70 nm. The experimental results of the LPGs coated with a coating thickness of 50 nm were compared with the modeled results. Coating thickness and uniformity were measured by SEM on coated optical fibre samples and, as a reference, film thickness was measured by ellipsometry on a coated silicon wafer. Ellipsometry was also used to measure the RI of the coatings.

A key result from this work was the quality of coatings achieved by PEALD. This method allowed deposition of conformal (*i.e.* full coverage) and uniform coating thicknesses on optical fibres. Measurements of coating thickness taken by SEM show low variability on optical fibres coated by the same process. This is an important result for researchers investigating transition mode behavior because the ability to achieve a target coating thickness is critical for tuning maximum sensitivity of LPGs at a given SRI. As a

result of uniform depositions, two LPGs coated in the same deposition process exhibit identical behavior as a function of SRI.

Another key result from this work was that two-step transitions were promoted due to the high RI of HfO<sub>2</sub>. These transitions can be explained using hybrid mode formulation (*i.e.* HE and EH modes). Unlike one-step transition in which the attenuation bands vanish at the transition point [101], in two-step transitions, the attenuation bands of the HE and EH modes are readily detectable at the transition point. This result is important because LPGs coated by HfO<sub>2</sub> can be tuned to operate at maximum sensitivity with amplitudes that are readily detectable by commercial optical interrogators.

The experimental results validate the results from the modeling for an LPG coated with 50 nm. Although the modeling conducted in this work does not account for EH modes, it is shown that it can be used to estimate the SRI at which the transition point of HE modes occur.

One limitation of the sensors reported in this study is the long deposition times required for PEALD at 150 °C to avoid grating degradation. Additionally, LPGs are expensive to manufacture because they require relatively complex manufacturing systems. This cost limitation led to a study of coated PCF interferometers presented in Section 3.4. This type of sensor is cheaper to manufacture and does not show thermal degradation which allows for use of thermal ALD at higher temperatures, decreasing deposition times.

Additional work, not included in the presented manuscript, was conducted to monitor concentrations of CO<sub>2</sub> in water at high pressure using LPGs coated with HfO<sub>2</sub>. The response of the sensors was lower than that predicted by the Lorentz-Lorenz equation

applied to the water/CO<sub>2</sub> mixtures. This is further discussed in Future Work presented in Chapter 4.

A more complete description of this study is presented in [141], which is included here as Appendix C.

### **3.4 Refractive index sensor based on inline Mach-Zehnder interferometer coated with hafnium oxide by atomic layer deposition<sup>4</sup>**

The objectives of this study are (1) to investigate the process parameters of thermal ALD that allow precise control over coating thickness; and (2) maximize the sensitivity of coated PCF interferometers at the RI of water (*i.e.* around 1.33).

As the lead student in this study, my role was to: coat PCF interferometers, characterize the coatings by measuring coating thickness and RI, characterize the RI behavior of the sensors, perform data analyses, and prepare the manuscript. The co-authors of this manuscript designed and fabricated the test rigs and provided editorial input for the manuscript.

Prior to this study, Smietana *et al.* reported on coating PCF interferometers with silicon nitride by radio frequency plasma enhanced CVD to increase RI sensitivity. The authors showed that the RI sensitivity of a coated PCF interferometer at a given SRI is highly dependent on coating thickness. CVD is a directional deposition method and, thus, control of coating thickness is challenging.

---

<sup>4</sup> Manuscript published in Sensors and Actuators B: Chemical

ALD is non-directional and is, therefore, well suited for deposition of conformal coatings on complex substrates [142]. Recently, ALD has been investigated for the application of coatings on FOSs. Examples include LPGs [115], [116], TFBGs [143], fibre tapers [144], and interferometers based on double cladding fibre coated with  $\text{Al}_2\text{O}_3$  [145]. These previous studies of ALD coatings on optical fibres focus mainly on the optical performance of the coated sensors. Determination of the deposition process parameters for precise control of coating thickness is not described in detail. ALD on surfaces that are not flat may require deposition parameters, such as pulse and purge times, to be adjusted to achieve adequate control over coating thickness

In this study, the effect of purge times on coating thickness was investigated by performing depositions with different purge times. For each deposition, coating thickness is measured on optical fibres by SEM and film thickness is measured on silicon wafers by ellipsometry. PCF interferometers were coated with  $\text{HfO}_2$  by selecting the process parameters determined by the study of purge time. The effect of coating thicknesses on the RI sensitivity of PCF interferometers was investigated. This study is the first to apply ALD to coat PCF interferometers to increase RI sensitivity.

One key result of this study is that control of coating thickness on optical fibres is achieved by selecting longer purge times, compared to conventional depositions on flat substrates. This occurs because the optical fibres disturb the gas flow, creating dead spaces where the precursors are trapped. As a consequence, if purges times specified for deposition on flat substrates are used to coat optical fibres, the gas precursors are not fully purged, leading to CVD-type deposition. In this case, the coating thickness can be

significantly thicker on fibres placed at the centre of the ALD substrate table and thinner on fibres placed on the edge of the ALD substrate table.

Another key result is the behavior of coated PCF interferometers as a function of SRI. The coating of PCF interferometers induces up to three different sensitivity regions. A region of higher sensitivity located between two regions of lower sensitivity. It is possible to shift the region of higher sensitivity to a target SRI range by tuning the coating thickness. This study shows that a sensitivity of 1307 nm/SRI at an SRI in the vicinity of water is obtained for a PCF interferometer with a coating thickness of 60 nm. This is the highest RI sensitivity reported for a PCF interferometer.

Additional work, not included in the presented manuscript, was conducted to monitor concentrations of CO<sub>2</sub> in water at high pressure using LPGs coated with HfO<sub>2</sub>. The response of the sensors was lower than that predicted by the Lorentz-Lorenz equation applied to the water/CO<sub>2</sub> mixtures. This is further discussed in Future Work presented in Chapter 4.

A more complete description of this study is presented in [146], which is included here as Appendix D.

## Chapter 4: Summary contributions and future work

### 4.1 Summary contributions

The overarching objective of this research was to develop RI-based FOSs to monitor CO<sub>2</sub> concentrations targeting CCS applications.

Two types of sensors were investigated, namely LPGs and an MZI configuration based on the intermodal interference between the core and a cladding mode of a PCF, referred to as PCF interferometer. As presented in *Section 2.1 Long period gratings* and in *Section 2.2 Mach-Zehnder interferometers*, these two sensors have low RI sensitivity in the region of interest for monitoring CO<sub>2</sub> storage (*i.e.* between 1.0 - 1.335).

The first objective of this research was to increase the sensitivity of LPGs at low SRIs. This objective was accomplished by coating LPGs with polystyrene using the dip-coating method. The second objective was to validate the performance of polystyrene coated LPGs as CO<sub>2</sub> sensors. This objective was accomplished by conducting tests at atmospheric and high pressure (*i.e.* 1400 psi) to simulate typical conditions of CO<sub>2</sub> monitoring at shallow and deep-subsurface environments, respectively. The third objective was to improve the precision in controlling the coating thickness relative to that achievable by the dip-coating method. This objective was accomplished by investigating ALD to coat LPGs and MZIs with HfO<sub>2</sub>.

This dissertation presents novel contributions organized into four main manuscripts that have been published in journals in the area of optics. These contributions also span

other disciplines such as chemistry and nanoscience including both modeling and experimental work. This work required knowledge and utilization of techniques to characterize materials including SEM and ellipsometry, and advanced deposition methods including ALD.

The first general topic of research in this dissertation comprises the study of LPGs and MZIs coated by dip-coating and ALD to increase the RI sensitivity at low SRIs. The second topic comprises the application of the developed sensors to monitor CO<sub>2</sub> under CCS conditions. The specific contributions for each of the four manuscripts presented in this dissertation are summarized below.

Highly sensitive coated long period grating sensor for CO<sub>2</sub> detection at atmospheric pressure: For this manuscript, the first two contributions are associated with sensor development. The first contribution of this study is the development of a polystyrene coated LPG able to distinguish between CO<sub>2</sub> and N<sub>2</sub> gases with reproducibility and reversibility. This was achieved by exploring transition mode behavior on LPGs. Specifically, by selecting a coating thickness that tunes the transition point of LPGs to the low SRI range, resulting in high RI sensitivity at the RI of gases. The second contribution is the development of a sensor that is able to continuously monitor concentrations of CO<sub>2</sub> at atmospheric pressure. Tests conducted at various CO<sub>2</sub> concentrations demonstrate that the polystyrene coated LPGs have a resolution of  $\pm 4.07\% \text{CO}_2$ .

The third contribution is associated with the understanding of the sensing mechanism. The detection of different gases (*i.e.* CO<sub>2</sub> and N<sub>2</sub>) and the measurement of CO<sub>2</sub> concentrations are based on the combination between SRI changes with the change of the

RI of the polystyrene coating. This manuscript compares the response of coated LPGs with transition points at high and low SRIs. The sensors with transition points at high SRI are unable to distinguish between N<sub>2</sub> and CO<sub>2</sub>. This demonstrates that the sorption of CO<sub>2</sub> into polystyrene is not sufficient to obtain a measurable signal between N<sub>2</sub> and CO<sub>2</sub> or between different CO<sub>2</sub> concentrations. To achieve a measurable wavelength shift is crucial to tune the transition point to the low SRI range.

Experimental investigation of long-period grating transition modes to monitor CO<sub>2</sub> in high-pressure aqueous solutions: The first contribution of this study is the development of an FOS based on a polystyrene coated LPG to monitor dissolution of CO<sub>2</sub> in water at high pressure. Tests conducted with a bare and a polystyrene coated LPG confirm that the bare LPG does not have sufficient sensitivity to distinguish between water and CO<sub>2</sub> saturated water, whereas the polystyrene coated LPG shows a significant wavelength shift as CO<sub>2</sub> dissolves in water at high pressure. The second contribution is the method used to measure coating uniformity on optical fibres coated with polystyrene by the dip-coating method. The measurement method comprised a rigorous protocol to measure coating thickness by SEM on different locations around a fibre section and on various fibre sections along a fibre length. The third contribution, similar with the previous study, is associated with the sensing principle for detection of CO<sub>2</sub>. This study confirms that the sensing mechanism is based on the combination of SRI and sorption of CO<sub>2</sub> by the polystyrene coating.

Long period gratings coated with hafnium oxide by plasma-enhanced atomic layer deposition for refractive index measurements: The first contribution of this manuscript is the investigation into PEALD to coat a UV-written LPG with the benefit of reduced deposition temperature, relative to thermal ALD, which avoids significant thermal

degradation of LPGs. The second contribution is utilization of a new coating material (*i.e.* HfO<sub>2</sub>) to promote transition mode behavior on LPGs. The advantages of this coating materials are articulated in the introduction of Appendix C.

The third contribution is associated with the potential of PEALD to coat optical fibres with conformal and uniform coating thicknesses. This was confirmed by measurements of coating thickness taken by SEM on various locations around the fibre section and length of two different coated fibres. As a result, the RI characterization of two LPGs coated at the same time by the same process show identical behavior.

The fourth contribution is associated with the nature of the transition mode behavior. Coating of LPGs with HfO<sub>2</sub> promotes two-step transitions due to the high-RI of the coating material. The benefit of this behavior is that the attenuation bands of the LPG are readily detectable at the transition point.

Refractive index sensor based on inline Mach-Zehnder interferometer coated with hafnium oxide by atomic layer deposition: The first contribution of this study is the investigation of thermal ALD to coat MZIs to increase RI sensitivity. This is a key contribution because the sensitivity of these sensors at low SRI is highly dependent on coating thickness. This demonstrates ALD as a suitable deposition method for these devices due to its potential to achieve high control of coating thickness. The second contribution is the PCF interferometer coated with a 60 nm coating which has the highest sensitivity (*i.e.* 1307 nm/SRI) at an SRI in the vicinity of water (*i.e.* 1.3327- 1.3478). The third contribution is associated with the deposition method. Control over coating thickness is achieved by increasing purge times relative to purge times required for deposition on a flat substrate.

## 4.2 Future work

The nature of research is such that, for each question answered, new questions arise. Given this, a project is rarely fully finished upon its completion. This section highlights potential areas of future work.

One limitation observed in the study presented in Section 3.2, *Experimental Investigation of Long-Period Grating Transition Modes to Monitor CO<sub>2</sub> in High-Pressure Aqueous Solutions*, is the lack of reversibility and subsequent reproducibility between consecutive trials of monitoring CO<sub>2</sub> at high pressure with a polystyrene coated LPG. Although the reason for this is not fully understood it may be due to: (1) contamination of the sensor caused by oil residues from mechanical components in the setup such as pumps and tank regulators; (2) coating damage due to degassing of the CO<sub>2</sub> from the coating during depressurization at the end of the test. Investigation of these two potential causes requires further tests. In the context of monitoring CO<sub>2</sub> leakage in storage sites, sensor reversibility may not be an essential condition given the long time-scales associated with CCS applications. In this application, polystyrene coated LPGs could be used as single-use sensors. These sensors could still provide useful information regarding a potential CO<sub>2</sub> leakage, which would help the decision making to initiate remediation protocols. Once a leak is controlled and the CO<sub>2</sub> concentration returns to the original levels, the CO<sub>2</sub> saturated sensors located in the observation wells could be replaced by new polystyrene coated LPGs.

For monitoring CO<sub>2</sub> concentrations in water at high pressure, LPGs and PCF interferometers coated with HfO<sub>2</sub> show lower wavelength shifts than those predicted by Lorentz-Lorenz equation. This result might be due to the approximation for the density of

the water/CO<sub>2</sub> mixture. In the calculation of the RI of CO<sub>2</sub> saturated water presented in Section 1.2, *Review of Fibre-optic sensors for CO<sub>2</sub> detection*, using Lorentz-Lorenz equation, the density of the mixture was assumed to be equal to the density of water, based on the large volume of water relative to CO<sub>2</sub>. This approximation was assumed due to the lack of precise data for the density of water/CO<sub>2</sub> mixture. Further investigation is necessary to develop a theoretical model to predict the RI of water with different concentrations of CO<sub>2</sub> with higher accuracy.

With this new knowledge, monitoring low concentrations of CO<sub>2</sub> in water may require LPGs and PCF interferometers with higher sensitivity than that reported in Appendix C and D, respectively. The sensitivity of coated LPGs could be further increased by combining the transition point with the DTP. Work reported by other groups show that the combination of these two phenomena leads to the highest reported RI sensitivities [117]–[119]; however, this requires coating of LPGs with high precision. PEALD is well suited to meet this precision requirement. The sensitivity of PCF interferometers could be further increased by etching or tapering the sensor as demonstrated recently by Zhao *et al.* [131]. However, the reduction of the fibre diameter introduces two limitations. First, the sensor becomes more fragile which is undesirable for downhole applications. Second, the spectrum becomes noisy due to the excitation of modes which are superimposed in the interference pattern. As a result, the detection of the valleys in the transmission spectrum becomes more challenging due to the irregular shape of the fringes [131]. Therefore, approaches based on reduction of fibre diameter of PCF interferometers require further investigation.

The application of the FOS in downhole environments requires the investigation of CO<sub>2</sub> selectivity and sensor packaging. CO<sub>2</sub> selectivity could be achieved by membranes that prevent confounding substances from reaching the evanescent field of the sensors. Additionally, FOS are prone to breakage and thus, the sensors will need mounting in a protective enclosure which allows fluid access to the sensors.

Additionally, as discussed in Section 1.2, *Review of fibre-optic sensors for CO<sub>2</sub> detection*, a concern of long-term monitoring using FOS is the increase in optical losses due to hydrogen diffusion into the optical fibres. As described in Appendix C, HfO<sub>2</sub> coating is expected to act as a hermetic coating which will reduce the diffusion of H<sub>2</sub> into the core of the optical fibre due to the high density of this coating material. The effect requires further investigation.

Finally, although the sensors developed in this research target CO<sub>2</sub> monitoring, the utilization of these sensors can be extended to other applications that require FOSs with high RI sensitivity and capability to withstand harsh environments.

## References

- [1] K. Keller, D. McInerney, and D. F. Bradford, "Carbon dioxide sequestration: how much and when?," *Clim. Change*, vol. 88, no. 3–4, pp. 267–291, 2008.
- [2] Intergovernmental Panel on Climate Change, Special report on "Carbon dioxide capture and storage," 2005.
- [3] J. M. Lemieux, "Review: The potential impact of underground geological storage of carbon dioxide in deep saline aquifers on shallow groundwater resources," *Hydrogeol. J.*, vol. 19, no. 4, pp. 757–778, 2011.
- [4] R. A. Chadwick, R. Arts, M. Bentham, O. Eiken, S. Holloway, G. A. Kirby, J. M. Pearce, J. P. Williamson, and P. Zweigel, "Review of monitoring issues and technologies associated with the long-term underground storage of carbon dioxide," *Geol. Soc. London, Spec. Publ.*, vol. 313, pp. 257–275, 2009.
- [5] R. G. Bruant, A. J. Guswa, M. A. Celia and C. A. Peters, "Safe Storage of CO<sub>2</sub> in Deep.," *Environ. Sci. Technol.*, vol. 36, no. 11, pp. 240A-245A, 2002
- [6] J. Song and D. Zhang, "Comprehensive review of caprock-sealing mechanisms for geologic carbon sequestration.," *Environ. Sci. Technol.*, vol. 47, no. 1, pp. 9–22, 2013.
- [7] National Energy Technology Laboratory, "Best practices for Monitoring, Verification , and Accounting of CO<sub>2</sub> Stored in Deep Geologic Formations," 2012
- [8] F. C. Boait, N. J. White, M. J. Bickle, R. A. Chadwick, J. A. Neufeld, and H. E. Huppert, "Spatial and temporal evolution of injected CO<sub>2</sub> at the Sleipner Field, North Sea," *J. Geophys. Res. Solid Earth*, vol. 117, pp. 1–21, 2012.
- [9] R. Arts, O. Eiken, A. Chadwick, P. Zweigel, L. Van der Meer, and B. Zinszner, "Monitoring of CO<sub>2</sub> injected at Sleipner using time-lapse seismic data," *Energy*, vol. 29,

no. 9–10, pp. 1383–1392, 2004.

[10] X. Jiang, W. Hassan, and J. Gluyas, “Modelling and monitoring of geological carbon storage: A perspective on cross-validation,” *Appl. Energy*, vol. 112, pp. 784–792, 2013.

[11] S. I. Plasynski, J. T. Litynski, H. G. McIlvried, D. M. Vikara, and R. D. Srivastava, “The critical role of monitoring, verification, and accounting for geologic carbon dioxide storage projects,” *Environ. Geosci.*, vol. 18, no. 1, pp. 19–34, 2011.

[12] S. Schloemer, M. Furche, I. Dumke, J. Poggenburg, A. Bahr, C. Seeger, A. Vidal, and E. Faber, “A review of continuous soil gas monitoring related to CCS - Technical advances and lessons learned,” *Appl. Geochemistry*, vol. 30, pp. 148–160, 2013.

[13] C. J. Seto and G. J. McRae, “Reducing risk in basin scale CO<sub>2</sub> sequestration: a framework for integrated monitoring design,” *Environ. Sci. Technol.*, vol. 45, no. 3, pp. 845–59, 2011.

[14] A. D. Kersey, “Optical Fiber Sensors for Permanent Downwell Monitoring Applications in the Oil and Gas Industry,” *IEICE Transactions on Electronics*, vol. E83C, no. 3, pp. 400–404, 2000.

[15] B. Culshaw, “Optical Fiber Sensor Technologies: Opportunities and-Perhaps-Pitfalls,” *J. Light. Technol.*, vol. 22, no. 1, pp. 39–50, 2004.

[16] D. Voigt, J. L. W. a van Geel, and O. Kerkhof, “Spatio-temporal noise and drift in fiber optic distributed temperature sensing,” *Meas. Sci. Technol.*, vol. 22, no. 8, 2011.

[17] A. Ukil, S. Member, H. Braendle, and P. Krippner, “Distributed Temperature Sensing : Review of Technology and Applications,” *IEEE Sensors Journal*, vol. 12, no. 5, pp. 885–892, 2012.

[18] S. H. Aref, H. Latifi, M. I. Zibaii, and M. Afshari, “Fiber optic Fabry–Perot pressure

- sensor with low sensitivity to temperature changes for downhole application,” *Opt. Commun.*, vol. 269, no. 2, pp. 322–330, 2007.
- [19] X. Zhou, Q. Yu, and W. Peng, “Simultaneous measurement of down-hole pressure and distributed temperature with a single fiber,” *Meas. Sci. Technol.*, vol. 23, no. 8, 2012.
- [20] Y. Zhao, Y. Liao, and S. Lai, “Simultaneous Measurement of Down-Hole High Pressure and Temperature With a bulk-modulus and FBG sensor,” vol. 14, no. 11, pp. 1584–1586, 2002.
- [21] P. M. Nellen, P. Mauron, A. Frank, U. Sennhauser, K. Bohnert, P. Pequignot, P. Bodor, H. Brandle, “Reliability of fiber Bragg grating based sensors for downhole applications,” vol. 103, pp. 364–376, 2003.
- [22] Schlumberger “[www.slb.com](http://www.slb.com).”
- [23] Verrillon “[www.verrillon.com](http://www.verrillon.com).”
- [24] AFL “[www.aflglobal.com](http://www.aflglobal.com).”
- [25] S. Martens, A. Liebscher, F. Möller, H. Würdemann, F. Schilling, and M. Kühn, “Progress report on the first european on-shore CO<sub>2</sub> storage site at ketzin (Germany) — Second year of injection,” *Energy Procedia*, vol. 4, pp. 3246–3253, 2011.
- [26] A. Liebscher, F. Möller, A. Bannach, S. Köhler, J. Wiebach, C. Schmidt-Hattenberger, M. Weiner, C. Pretschner, K. Ebert, and J. Zemke, “Injection operation and operational pressure–temperature monitoring at the CO<sub>2</sub> storage pilot site Ketzin, Germany-Design, results, recommendations,” *Int. J. Greenh. Gas Control*, vol. 15, pp. 163–173, 2013.
- [27] H. Segawa, E. Ohnishi, Y. Arai, and K. Yoshida, “Sensitivity of fiber-optic carbon dioxide sensors utilizing indicator dye,” *Sensors Actuators B Chem.*, vol. 94, no. 3, pp. 276–281, 2003.

- [28] C. S. Chu and Y. L. Lo, "Highly sensitive and linear optical fiber carbon dioxide sensor based on sol-gel matrix doped with silica particles and HPTS," *Sensors Actuators B Chem.*, vol. 143, no. 1, pp. 205–210, 2009.
- [29] A. Ksendzov, S. Forouhar, R. M. Briggs, C. Frez, K. J. Franz, and M. Bagheri, "Linewidth measurement of high power diode laser at 2  $\mu\text{m}$  for carbon dioxide detection," *Electron. Lett.*, vol. 48, no. 9, pp. 520–522, 2012.
- [30] J. A. Nwaboh, J. Hald, J. K. Lyngso, J. C. Petersen, and O. Werhahn, "Measurements of CO<sub>2</sub> in a multipass cell and in a hollow-core photonic bandgap fiber at 2  $\mu\text{m}$ ," *Appl. Phys. B*, vol. 110, no. 2, pp. 187–194, 2013.
- [31] S. Pevec and D. Donlagic, "Nanowire-based refractive index sensor on the tip of an optical fiber," *Appl. Phys. Lett.*, vol. 102, no. 21, 2013.
- [32] B. N. Shivananju, S. Yamdagni, R. Fazuldeen, A. K. Sarin Kumar, G. M. Hegde, M. M. Varma, and S. Asokan, "CO<sub>2</sub> sensing at room temperature using carbon nanotubes coated core fiber Bragg grating," *Rev. Sci. Instrum.*, vol. 84, no. 6, 2013.
- [33] X. Chong, K. J. Kim, P. R. Ohodnicki, E. Li, C. H. Chang, and A. X. Wang, "Ultrashort Near-Infrared Fiber-Optic Sensors for Carbon Dioxide Detection," *IEEE Sens. J.*, vol. 15, no. 9, pp. 5327–5332, 2015.
- [34] R. Orghici, U. Willer, M. Gierszewska, S. R. Waldvogel, and W. Schade, "Detection of explosives and CO<sub>2</sub> dissolved in water with an evanescent field sensor," *2008 Conf. Quantum Electron. Laser Sci. Conf. Lasers Electro-Optics, CLEO/QELS*, pp. 568-569, 2008.
- [35] B. Soukup, K. S. Repasky, J. L. Carlsten, and G. Wicks, "Field demonstration of a 1  $\times$  4 fiber sensor array for subsurface carbon dioxide monitoring for carbon sequestration,"

*Journal of Applied Remote Sensing*, Vol. 8, 2014.

[36] M. V. Avdeev, A. N. Konovalov, V. N. Bagratashvili, V. K. Popov, S. I. Tsypina, M. Sokolova, J. Ke, and M. Poliakov, "The fibre optic reflectometer: A new and simple probe for refractive index and phase separation measurements in gases, liquids and supercritical fluids," *Phys. Chem. Chem. Phys.*, vol. 6, no. 6, p. 1258-1263, 2004.

[37] X. D. Wang and O. S. Wolfbeis, "Fiber-Optic Chemical Sensors and Biosensors (2013-2015)," *Anal. Chem.*, vol. 88, no. 1, pp. 203–227, 2016.

[38] T. Zhu, D. Wu, M. Liu, and D. W. Duan, "In-line fiber optic interferometric sensors in single-mode fibers," *Sensors*, vol. 12, no. 8, pp. 10430–10449, 2012.

[39] G. Rego, "A review of refractometric sensors based on long period fibre gratings," *Sci. World J.*, vol. 2013, 2013.

[40] J. Villatoro, D. Monzón-Hernández, and D. Talavera, "High resolution refractive index sensing with cladded multimode tapered optical fibre," *Electron. Lett.*, vol. 40, no. 2, 2004.

[41] N. D. Rees, S. W. James, R. P. Tatam, and G. J. Ashwell, "Optical fiber long-period gratings with Langmuir-Blodgett thin-film overlays.," *Opt. Lett.*, vol. 27, no. 9, pp. 686–688, May 2002.

[42] M. Smietana, D. Brabant, W. J. Bock, P. Mikulic, and T. Eftimov, "Refractive-Index Sensing With Inline Core-Cladding Intermodal Interferometer Based on Silicon Nitride," *Journal of Lightwave Technology*, vol. 30, no. 8, pp. 1185–1189, 2012.

[43] P. Pilla, V. Malachovska, A. Borriello, A. Buosciolo, M. Giordano, L. Ambrosio, A. Cutolo, and A. Cusano, "Transition mode long period grating biosensor with functional multilayer coatings," *Opt. Express*, vol. 19, no. 2, pp. 512–26, 2011.

- [44] Y. Sun, B. Shekunov, and P. York, "Refractive index of supercritical CO<sub>2</sub>-ethanol solvents," *Chem. Eng. Commun.*, vol. 190, no. 1, pp. 1–14, 2003.
- [45] Y. Song, M. Nishio, B. Chen, S. Someya, T. Ohsumi, "Measurement on CO<sub>2</sub> Solution Density by Optical Technology," *Journal of Visualization*, vol. 6, no. 1, 2003.
- [46] A. Z. Tasic, B. D. Djordjevic, D. K. Grozdanic, N. Radojkovic, "Use of Mixing Rules in Predicting Refractive Indices and Specific Refractivities for Some Binary Liquid Mixtures," *Journal of Chemical and Engineering Data*, vol. 37, no. 3, pp. 310–313, 1992.
- [47] NIST Chemistry WebBook. (2014, Dec. 29). [Online]. Available: <http://webbook.nist.gov/chemistry/fluid/>.
- [48] L. Melo, G. Burton, S. Warwick, and P. M. Wild, "Experimental Investigation of Long-Period Grating Transition Modes to Monitor CO<sub>2</sub> in High-Pressure Aqueous Solutions," *J. Light. Technol.*, vol. 33, no. 12, pp. 2554–2560, 2015.
- [49] M. Fujiwara, K. Toubaru, and S. Takeuchi, "Optical transmittance degradation in tapered fibers," *Opt. Express*, vol. 19, no. 9, pp. 8596–8601, 2011.
- [50] V. G. Plotnichenko, V. O. Sokolov, and E. M. Dianov, "Hydroxyl groups in high-purity silica glass," *J. Non. Cryst. Solids*, vol. 261, no. 1-3, pp. 186–194, 2000.
- [51] S. Tanaka, M. Kyoto, M. Watanabe, H. Yokota, "Hydroxyl group formation caused by hydrogen diffusion into optical-glass fiber," *Electronics Letters*, vol. 20, no. 7, pp. 3–4, 1984.
- [52] V. G. Plotnichenko, V. O. Sokolov, E. B. Kryukova, and E. M. Dianov, "Hydroxyl groups in phosphosilicate glasses for fibre optics," *J. Non. Cryst. Solids*, vol. 270, no. 1–3, pp. 20–27, 2000.
- [53] F. Ahmed, H. Joe, B. Min, and M. Jun, "Characterization of refractive index change

- and fabrication of long period gratings in pure silica fiber by femtosecond laser radiation,” *Opt. Laser Technol.*, vol. 74, pp. 119–124, 2015.
- [54] H. Y. Choi, M. J. Kim, and B. H. Lee, “All-fiber Mach-Zehnder type interferometers formed in photonic crystal fiber,” *Opt. Express*, vol. 15, no. 9, pp. 5711–5720, 2007.
- [55] S. W. James and R. P. Tatam, “Optical fibre long-period grating sensors : characteristics and application,” *Measurement Science and Technology*, vol. 49, no. 5, pp. R49-R61, 2003
- [56] D. Barrera, J. Villatoro, V. P. Finazzi, G. A. Cardenas-Sevilla, V. P. Minkovich, S. Sales, and V. Pruneri, “Low-loss photonic crystal fiber interferometers for sensor networks,” *J. Light. Technol.*, vol. 28, no. 24, pp. 3542–3547, 2010.
- [57] M. Pospisilova, G. Kuncova, and J. Trogl, “Fiber-optic chemical sensors and fiber-optic bio-sensors,” *Sensors*, vol. 15, no. 10, pp. 25208–25259, 2015.
- [58] P. Wang, G. Brambilla, M. Ding, Y. Semenova, Q. Wu, and G. Farrell, “High-sensitivity, evanescent field refractometric sensor based on a tapered, multimode fiber interference,” *Opt. Lett.*, vol. 36, no. 12, pp. 2233–2235, 2011.
- [59] M. H. Chiu, S. N. Hsu, and H. Yang, “D-type fiber optic sensor used as a refractometer based on total-internal reflection heterodyne interferometry,” *Sensors Actuators, B Chem.*, vol. 101, no. 3, pp. 322–327, 2004.
- [60] W. Jin, G. Stewart, M. Wilkinson, B. Culshaw, F. Muhammad, S. Murray, and J. Norris, “Compensation for surface contamination in a D-fiber evanescent wave methane sensor,” *J. Light. Technol.*, vol. 13, no. 6, pp. 1177–1183, 1995.
- [61] L. Bilro, N. J. Alberto, L. M. Sa, J. D. L. Pinto, and R. Nogueira, “Analytical Analysis of Side-Polished Plastic Optical Fiber as Curvature and Refractive Index Sensor,” vol. 29,

no. 6, pp. 864–870, 2011.

[62] W. J. Bock, T. A. Eftimov, and P. Mikulic, “An Inline Core-Cladding Intermodal Interferometer Using a Photonic Crystal Fiber,” *J. Light. Technol.*, vol. 27, no. 17, pp. 3933-3939, Sep. 2009.

[63] W. Xu, X. G. Huang, and J. S. Pan, “Simple fiber-optic refractive index sensor based on fresnel reflection and optical switch,” *IEEE Sens. J.*, vol. 13, no. 5, pp. 1571–1574, 2013.

[64] C. R. Biazoli, S. Silva, M. Franco, O. Frazão, and C. M. B. Cordeiro, “Multimode interference tapered fiber refractive index sensors,” *Appl. Opt.*, vol. 51, no. 24, pp. 5941-5945, 2012.

[65] T. K. Yadav, R. Narayanaswamy, M. H. Abu Bakar, Y. M. Kamil, and M. a. Mahdi, “Single mode tapered fiber-optic interferometer based refractive index sensor and its application to protein sensing,” *Opt. Express*, vol. 22, no. 19, p. 22802, 2014.

[66] S. W. James, M. L. Dockney, R. P. Tatam, “Simultaneous independent temperature and strain measurement using in-fibre Bragg grating sensors” *Electron. Lett.*, vol. 32, no. 12, pp. 1133–1134, 1996.

[67] W. Liang, Y. Huang, Y. Xu, R. K. Lee, and A. Yariv, “Highly sensitive fiber Bragg grating refractive index sensors,” *Appl. Phys. Lett.*, vol. 86, no. 15, pp. 1–3, 2005.

[68] N. J. Alberto, C. A. Marques, J. L. Pinto, and R. N. Nogueira, “Three-parameter optical fiber sensor based on a tilted fiber Bragg grating,” *Appl. Opt.*, vol. 49, no. 31, pp. 6085-6091, 2010.

[69] J. Albert, L. Y. Shao, and C. Caucheteur, “Tilted fiber Bragg grating sensors,” *Laser Photon. Rev.*, vol. 7, no. 1, pp. 83–108, 2013.

- [70] R. B. Queiros, C. Gouveia, J. R. A. Fernandes, and P. A. S. Jorge, “Evanescent wave DNA-aptamer biosensor based on long period gratings for the specific recognition of E. coli outer membrane proteins,” *Biosens. Bioelectron.*, vol. 62, pp. 227–233, 2014.
- [71] A. V. Hine, X. Chen, M. D. Hughes, K. Zhou, E. Davies, K. Sugden, I. Bennion, and L. Zhang, “Optical fibre-based detection of DNA hybridization,” *Biochem. Soc. Trans.*, vol. 37, no. 2, pp. 445–449, 2009.
- [72] J. N. Wang and J. L. Tang, “Feasibility of fiber Bragg grating and long-period fiber grating sensors under different environmental conditions,” *Sensors*, vol. 10, no. 11, pp. 10105–10127, 2010.
- [73] H. Y. Liu, D. K. Liang, J. Zeng, J. Jin, J. Wu, and J. Geng, “Design of a long-period fiber grating sensor for reinforcing bar corrosion in concrete,” *J. Intell. Mater. Syst. Struct.*, vol. 23, no. 1, pp. 45–51, 2012.
- [74] T. Wei, Y. Han, Y. Li, H. L. Tsai, and H. Xiao, “Temperature-insensitive miniaturized fiber inline Fabry-Perot interferometer for highly sensitive refractive index measurement,” *Opt. Express*, vol. 16, no. 8, pp. 5764–5769, 2008.
- [75] Y. Wang, D. N. Wang, C. R. Liao, T. Hu, J. Guo, and H. Wei, “Temperature-insensitive refractive index sensing by use of micro Fabry-Pérot cavity based on simplified hollow-core photonic crystal fiber,” *Opt. Lett.*, vol. 38, no. 3, pp. 269–71, 2013.
- [76] X. Ning, C. Zhao, F. Shi, and J. Kang, “Zeolite Thin Film-Coated Fiber Sensors Based on Fabry-Perot Interferometer for Detection of Chemical Vapors,” *Photonic sensors*, vol. 5, no. 2, pp. 137–141, 2015.
- [77] G. Zhang, M. Yang, and Y. Wang, “Optical fiber-tip Fabry-Perot interferometer for hydrogen sensing,” *Opt. Commun.*, vol. 329, pp. 34–37, 2014.

- [78] Q. Rong, X. Qiao, Y. Du, H. Sun, D. Feng, R. Wang, M. Hu, and Z. Feng, "In-fiber quasi-Michelson interferometer for liquid level measurement with a core-cladding-modes fiber end-face mirror," *Opt. Lasers Eng.*, vol. 57, pp. 53–57, 2014.
- [79] H. Meng, W. Shen, G. Zhang, X. Wu, W. Wang, C. Tan, and X. Huang, "Michelson interferometer-based fiber-optic sensing of liquid refractive index," *Sensors Actuators, B Chem.*, vol. 160, no. 1, pp. 720–723, 2011.
- [80] M. Shao, X. Qiao, H. Fu, N. Zhao, Q. Liu, and H. Gao, "An In-Fiber Mach-Zehnder Interferometer Based on Arc-Induced Tapers for High Sensitivity," *IEEE Sens. J.*, vol. 13, no. 5, pp. 2026–2031, 2013.
- [81] A. Lokman, H. Arof, and S. W. Harun, "Dumbbell shaped inline Mach-Zehnder interferometer for glucose detection," *Measurement*, vol. 59, pp. 167–170, 2015.
- [82] M. F. Jaddoa, A. A. Jasim, M. Z. A. Razak, S. W. Harun, and H. Ahmad, "Highly responsive NaCl detector based on inline microfiber Mach-Zehnder interferometer," *Sensors Actuators A Phys.*, vol. 237, pp. 56–61, 2016.
- [83] K. O. Hill and G. Meltz, "Fiber Bragg Grating Technology Fundamentals and Overview," *IEEE J. Light. Technol.*, vol. 15, no. 8, pp. 1263–1276, 1997.
- [84] T. Erdogan, "Cladding-mode resonances in short- and long- period fiber grating filters," *J. Opt. Soc. Am. A. Opt. Image Sci. Vis.*, vol. 14, no. 8, pp. 1760–1773, 1997.
- [85] H. J. Patrick, A. D. Kersey, and F. Bucholtz, "Analysis of the response of long period fiber gratings to external index of refraction," *J. Light. Technol.*, vol. 16, no. 9, pp. 1606–1612, 1998.
- [86] B. H. Lee, Y. Liu, S. B. Lee, S. S. Choi, and J. N. Jang, "Displacements of the resonant peaks of a long-period fiber grating induced by a change of ambient refractive index," *Opt.*

*Lett.*, vol. 22, no. 23, pp. 1769-1771, 1997.

[87] A. Martinez-Rios, D. Monzon-Hernandez, and I. Torres-Gomez, "Highly sensitive cladding-etched arc-induced long-period fiber gratings for refractive index sensing," *Opt. Commun.*, vol. 283, no. 6, pp. 958-962, 2010.

[88] P. Biswas, N. Basumallick, S. Bandyopadhyay, K. Dasgupta, A. Ghosh, and S. Bandyopadhyay, "Sensitivity Enhancement of Turn-Around-Point Long Period Gratings By Tuning Initial Coupling Condition," *IEEE Sens. J.*, vol. 15, no. 2, pp. 1240-1245, 2015.

[89] A. Iadicicco, S. Campopiano, M. Giordano, and A. Cusano, "Spectral behavior in thinned long period gratings: effects of fiber diameter on refractive index sensitivity," *Appl. Opt.*, vol. 46, no. 28, pp. 6945-6952, 2007.

[90] X. Shu, L. Zhang, and I. Bennion, "Sensitivity characteristics of long-period fiber gratings," *J. Light. Technol.*, vol. 20, no. 2, pp. 255-266, 2002.

[91] I. M. White and X. Fan, "On the performance quantification of resonant refractive index sensors," *Opt. Express*, vol. 16, no. 2, pp. 1020-1028, 2008.

[92] C. R. Zamarreno, I. R. Matías, and F. J. Arregui, "Nanofabrication Techniques Applied to the Development of Novel Optical Fiber Sensors Based on Nanostructured Coatings," *IEEE sens. j.*, vol. 12, no. 8, pp. 2699-2710, 2012.

[93] X. Wei, T. Wei, H. Xiao, and Y. S. Lin, "Nano-structured Pd-long period fiber gratings integrated optical sensor for hydrogen detection," *Sensors Actuators B Chem.*, vol. 134, no. 2, pp. 687-693, 2008.

[94] K. M. Tan, C. M. Tay, S. C. Tjin, C. C. Chan, and H. Rahardjo, "High relative humidity measurements using gelatin coated long-period grating sensors," *Sensors Actuators B Chem.*, vol. 110, no. 2, pp. 335-341, 2005.

- [95] L. Alwis, T. Sun, and K. V. Grattan, "Analysis of Polyimide-Coated Optical Relative Humidity Sensor," *IEEE Sens. J.*, vol. 13, no. 2, pp. 767-771, 2013.
- [96] J. Zhang, X. Tang, J. Dong, T. Wei, and H. Xiao, "Zeolite thin film-coated long period fiber grating sensor for measuring trace organic vapors," *Sensors Actuators, B Chem.*, vol. 135, no. 2, pp. 420-425, 2009.
- [97] M. Konstantaki, A. Klini, D. Anglos, and S. Pissadakis, "An ethanol vapor detection probe based on a ZnO nanorod coated optical fiber long period grating," *Opt. Express*, vol. 20, no. 8, pp. 8472-8484, 2012.
- [98] S. Korposh, R. Selyanchyn, W. Yasukochi, S. W. Lee, S. W. James, and R. P. Tatam, "Optical fibre long period grating with a nanoporous coating formed from silica nanoparticles for ammonia sensing in water," *Mater. Chem. Phys.*, vol. 133, no. 2-3, pp. 784-792, 2012.
- [99] I. Del Villar, I. Matías, F. Arregui, and P. Lalanne, "Optimization of sensitivity in Long Period Fiber Gratings with overlay deposition," *Opt. Express*, vol. 13, no. 1, pp. 56-69, 2005.
- [100] A. Cusano, A. Iadicicco, P. Pilla, L. Contessa, S. Campopiano, A. Cutolo, and M. Giordano, "Mode transition in high refractive index coated long period gratings," *Opt. Express*, vol. 14, no. 1, pp. 19-34, 2006.
- [101] A. Cusano, A. Iadicicco, P. Pilla, L. Contessa, S. Campopiano, A. Cutolo, and M. Giordano, "Cladding mode reorganization in high-refractive-index-coated long-period gratings: effects on the refractive-index sensitivity," *Opt. Lett.*, vol. 30, no. 19, pp. 2536-2538, 2005.
- [102] M. Partridge, R. Wong, S. W. James, F. Davis, S. P. J. Higson, and R. P. Tatam,

- “Long period grating based toluene sensor for use with water contamination,” *Sensors Actuators, B Chem.*, vol. 203, pp. 621–625, 2014.
- [103] I. Del Villar, M. Achaerandio, I. R. Matías, and F. J. Arregui, “Deposition of overlays by electrostatic self-assembly in long-period fiber gratings,” *Opt. Lett.*, vol. 30, no. 7, pp. 720–722, 2005.
- [104] S. Korposh, S. W. James, S. Lee, S. Topliss, S. C. Cheung, W. J. Batty, and R. P. Tatam, “Fiber optic long period grating sensors with a nanoassembled mesoporous film of SiO<sub>2</sub> nanoparticles,” *Opt. Express*, vol. 18, no. 12, pp. 13227-13238, 2010.
- [105] T. Wang, S. Korposh, S. James, R. Tatam, and S. W. Lee, “Optical fiber long period grating sensor with a polyelectrolyte alternate thin film for gas sensing of amine odors,” *Sensors Actuators B Chem.*, vol. 185, pp. 117–124, 2013.
- [106] P. Pilla, P. F. Manzillo, V. Malachovska, A. Buosciolo, S. Campopiano, A. Cutolo, L. Ambrosio, M. Giordano, and A. Cusano, “Long period grating working in transition mode as promising technological platform for label-free biosensing,” *Opt. Express*, vol. 17, no. 22, pp. 20039–20050, 2009.
- [107] P. Pilla, A. Sandomenico, V. Malachovska, A. Borriello, M. Giordano, A. Cutolo, M. Ruvo, and A. Cusano, “A protein-based biointerfacing route toward label-free immunoassays with long period gratings in transition mode,” *Biosens. Bioelectron.*, vol. 31, no. 1, pp. 486-491, 2012.
- [108] M. Smietana, W. J. Bock, and P. Mikulic, “Effect of high-temperature plasma-deposited nano-overlays on the properties of long-period gratings written with UV and electric arc in non-hydrogenated fibers,” *Meas. Sci. Technol.*, vol. 24, no. 9, 2013.
- [109] M. Smietana, J. Szmidt, M. L. Korwin-Pawłowski, W. J. Bock, and J. Grabarczyk,

“Application of diamond-like carbon films in optical fibre sensors based on long-period gratings,” *Diam. Relat. Mater.*, vol. 16, no. 4–7, pp. 1374–1377, 2007.

[110] K. Krogulski, M. Smietana, B. Michalak, A. K. Debowska, M. Dudek, B. S. Witkowski, P. Mikulic, and W. J. Bock, “Properties of diamond-like carbon nano-coating deposited with RF PECVD method on UV-induced long-period fibre gratings,” *Phys. Status Solidi*, vol. 211, no. 10, pp. 2307–2312, 2014.

[111] L. Coelho, D. Viegas, J. L. Santos, and J. Almeida, “Optical sensor based on hybrid FBG/titanium dioxide coated LPFG for monitoring organic solvents in edible oils,” *Talanta*, vol. 148, pp. 170–176, 2016.

[112] M. Smietana, M. Dominik, M. Mysliwiec, N. Kwietniewski, P. Mikulic, B. S. Witkowski, and W. J. Bock, “Properties of silicon nitride thin overlays deposited on optical fibers-Effect of fiber suspension in radio frequency plasma-enhanced chemical vapor deposition reactor,” *Thin Solid Films*, vol. 603, pp. 8–13, 2016.

[113] M. Smietana, M. Koba, P. Mikulic, R. Bogdanowicz, and W. J. Bock, “Improved diamond-like carbon coating deposition uniformity on cylindrical sample by its suspension in RF PECVD chamber,” *Phys. Status Solidi*, vol. 212, no. 11, pp. 2496–2500, 2015.

[114] M. Smietana, W. J. Bock, and P. Mikulic, “Effect of high-temperature plasma-deposited nano-overlays on the properties of long-period gratings written with UV and electric arc in non-hydrogenated fibers,” *Meas. Sci. Technol.*, vol. 24, pp. 1–8, 2013.

[115] M. Smietana, M. Mysliwiec, P. Mikulic, B. S. Witkowski, and W. J. Bock, “Capability for fine tuning of the refractive index sensing properties of long-period gratings by atomic layer deposited Al<sub>2</sub>O<sub>3</sub> overlays,” *Sensors*, vol. 13, no. 12, pp. 16372–16383, 2013.

- [116] F. Zou, Y. Liu, C. Deng, Y. Dong, S. Zhu, and T. Wang, "Refractive index sensitivity of nano-film coated long-period fiber gratings," *Opt. Express*, vol. 23, no. 2, pp. 1114-1124, 2015.
- [117] P. Pilla, C. Trono, F. Baldini, F. Chiavaioli, M. Giordano, and A. Cusano, "Giant sensitivity of long period gratings in transition mode near the dispersion turning point: an integrated design approach," *Opt. Lett.*, vol. 37, no. 19, pp. 4152-4154, 2012.
- [118] M. Smietana, M. Koba, E. Brzozowska, K. Krogulski, J. Nakonieczny, L. Wachnicki, P. Mikulic, M. Godlewski, and W. J. Bock, "Label-free sensitivity of long-period gratings enhanced by atomic layer deposited TiO<sub>2</sub> nano-overlays," *Opt. Express*, vol. 23, no. 7, pp. 8441-8453, 2015.
- [119] I. Del Villar, "Ultrahigh-sensitivity sensors based on thin-film coated long period gratings with reduced diameter, in transition mode and near the dispersion turning point," *Opt. Express*, vol. 23, no. 7, pp. 8389-8398, 2015.
- [120] T. Allsop, R. Reeves, D. J. Webb, I. Bennion, and R. Neal, "A high sensitivity refractometer based upon a long period grating Mach-Zehnder interferometer," *Rev. Sci. Instrum.*, vol. 73, no. 4, pp. 1702-1705, 2002.
- [121] Z. Tian, S. S. Yam, J. Barnes, W. Bock, P. Greig, J. M. Fraser, H. Loock, and R. D. Oleschuk, "Refractive Index Sensing With Mach-Zehnder Interferometer Based on Concatenating Two Single-Mode Fiber Tapers," vol. 20, no. 5-8, pp. 626-628, 2008.
- [122] Z. Tian, S. Yam, and H. P. Loock, "Single-Mode Fiber Refractive Index Sensor Based on Core-Offset Attenuators," *IEEE Photonics Technol. Lett.*, vol. 20, no. 13-16, pp. 1387-1389, 2008.
- [123] Q. W. Q. Wang, G. Farrell, and W. Y. W. Yan, "Investigation on Single-Mode-

Multimode-Single-Mode Fiber Structure,” *J. Light. Technol.*, vol. 26, no. 5-8, pp. 512–519, 2008.

[124] R. Huang, K. Ni, X. Wu, and Q. Ma, “Refractometer based on Mach–Zehnder interferometer with peanut-shape structure,” *Opt. Commun.*, vol. 353, pp. 27–29, 2015.

[125] Y. Wang, M. Yang, D. N. Wang, S. Liu, and P. Lu, “Fabricated By Femtosecond Laser Micromachining for Refractive Index Measurement With High Sensitivity,” *J. Opt. Soc. Am. B*, vol. 27, no. 3, pp. 370–374, 2010.

[126] J. Villatoro, V. P. Minkovich, V. Pruneri, and G. Badenes, “Simple all-microstructured-optical-fiber interferometer built via fusion splicing,” *Opt. Express*, vol. 15, no. 4, pp. 1491–1496, 2007.

[127] J. C. Knight, T. A. Birks, P. S. Russell, D. M. Atkin, "All-silica single-mode optical fiber with photonic crystal cladding", *Optics Letters*, vol. 21, no. 19, pp. 1547-1549, 1996.

[128] P. J. Roberts, F. Couny, H. Sabert, B. J. Mangan, D. P. Williams, L. Farr, M. Mason, A. Tomlinson, T. Birks, J. Knight, and P. S. J. Russell, “Ultimate low loss of hollow-core photonic crystal fibres,” *Opt. Express*, vol. 13, no. 1, pp. 236–244, 2005.

[129] V. P. Minkovich, D. Monzon-Hernandez, J. Villatoro, and G. Badenes, “Microstructured optical fiber coated with thin films for gas and chemical sensing,” *Opt. Express*, vol. 14, no. 18, pp. 8413–8418, 2006.

[130] R. Jha, J. Villatoro, G. Badenes, and V. Pruneri, “Refractometry based on a photonic crystal fiber interferometer,” *Opt. Lett.*, vol. 34, no. 5, pp. 617–619, 2009.

[131] Y. Zhao, X. Li, L. Cai, and Y. Yang, “Refractive index sensing based on photonic crystal fiber interferometer structure with up-tapered joints,” *Sensors Actuators B Chem.*, vol. 221, pp. 406–410, 2015.

- [132] J. Mathew, Y. Semenova, and G. Farrell, "Effect of coating thickness on the sensitivity of a humidity sensor based on an Agarose coated photonic crystal fiber interferometer," *Opt. Express*, vol. 21, no. 5, pp. 6313–6320, 2013.
- [133] T. Li, X. Dong, C. C. Chan, K. Ni, S. Zhang, and P. P. Shum, "Humidity Sensor With a PVA-Coated Photonic Crystal Fiber Interferometer," *IEEE Sens. J.*, vol. 13, no. 6, pp. 2214-2216, 2013.
- [134] S. Lee, S. S. Saini, and M. Jeong, "Simultaneous Measurement of Refractive Index , Temperature , and Strain Using Etched-Core Fiber Bragg Grating Sensors," *IEEE Photonics Technol. Lett.*, vol. 22, no. 19, pp. 1431-1433, 2010.
- [135] C. F. Chan, C. Chen, A. Jafari, A. Laronche, D. J. Thomson, and J. Albert, "Optical fiber refractometer using narrowband cladding-mode resonance shifts," *Appl. Opt.*, vol. 46, no. 7, pp. 1142-1149, 2007.
- [136] G. M. Rego, J. L. Santos, and H. M. Salgado, "Refractive index measurement with long-period gratings arc-induced in pure-silica-core fibres," *Opt. Commun.*, vol. 259, no. 2, pp. 598-602, 2006.
- [137] A. Singh, "Long period fiber grating based refractive index sensor with enhanced sensitivity using Michelson interferometric arrangement," *Photonic Sensors*, vol. 5, no. 2, pp. 172–179, 2015.
- [138] A. Zhou, G. Li, Y. Zhang, Y. Wang, C. Guan, J. Yang, and L. Yuan, "Asymmetrical twin-core fiber based michelson interferometer for refractive index sensing," *J. Light. Technol.*, vol. 29, no. 19, pp. 2985-2991, 2011.
- [139] L. Melo, G. Burton, B. Davies, D. Risk, and P. Wild, "Highly sensitive coated long period grating sensor for CO<sub>2</sub> detection at atmospheric pressure," *Sensors Actuators B*

*Chem.*, vol. 202, pp. 294-300, 2014.

[140] B. Bao, L. Melo, B. Davies, H. Fadaei, D. Sinton, and P. Wild, "Detecting supercritical CO<sub>2</sub> in brine at sequestration pressure with an optical fiber sensor," *Environ. Sci. Technol.*, vol. 47, no. 1, pp. 306-313, 2013.

[141] L. Melo, G. Burton, P. Kubik, and P. Wild, "Long period gratings coated with hafnium oxide by plasma-enhanced atomic layer deposition for refractive index measurements," *Opt. Express*, vol. 24, no. 7, p. 7654, 2016.

[142] H. Kim, H. B. R. Lee, and W. J. Maeng, "Applications of atomic layer deposition to nanofabrication and emerging nanodevices," *Thin Solid Films*, vol. 517, no. 8, pp. 2563-2580, 2009.

[143] D. J. Mandia, W. Zhou, M. J. Ward, H. Joress, J. J. Sims, J. B. Giorgi, J. Albert, and S. T. Barry, "The effect of ALD-grown Al<sub>2</sub>O<sub>3</sub> on the refractive index sensitivity of CVD gold-coated optical fiber sensors," *Nanotechnology*, vol. 26, no. 43, 2015.

[144] S. Zhu, F. Pang, S. Huang, F. Zou, Y. Dong, and T. Wang, "High sensitivity refractive index sensor based on adiabatic tapered optical fiber deposited with nanofilm by ALD," *Opt. Express*, vol. 23, no. 11, 2015.

[145] Y. Zhao, F. Pang, Y. Dong, J. Wen, Z. Chen, and T. Wang, "Refractive index sensitivity enhancement of optical fiber cladding mode by depositing nanofilm via ALD technology," *Opt. Express*, vol. 21, no. 22, pp. 26136-26143, 2013.

[146] L. Melo, G. Burton, P. Kubik, and P. Wild, "Refractive index sensor based on inline Mach-Zehnder interferometer coated with hafnium oxide by atomic layer deposition," *Sensors Actuators B Chem.*, vol. 236, pp. 537-545, 2016.

**Appendix A: Highly sensitive coated long period grating sensor for CO<sub>2</sub> detection at atmospheric pressure**

L. Melo, G. Burton, B. Davies, D. Risk, and P. Wild, “Highly sensitive coated long period grating sensor for CO<sub>2</sub> detection at atmospheric pressure,” *Sensors Actuators B Chem.*, vol. 202, pp. 294-300, 2014.

Reprinted, with permission, from *Sensors and Actuators B: Chemical*, Elsevier



# Highly sensitive coated long period grating sensor for CO<sub>2</sub> detection at atmospheric pressure



Luis Melo<sup>a,\*</sup>, Geoff Burton<sup>a</sup>, Benjamin Davies<sup>a</sup>, David Risk<sup>b</sup>, Peter Wild<sup>a</sup>

<sup>a</sup> Department of Mechanical Engineering and Institute for Integrated Energy Systems (IESVic), University of Victoria, P.O. Box 3055, Victoria, B.C., Canada V8W 3P6

<sup>b</sup> St. Francis Xavier University, Earth Sciences, P.O. Box 5000, Antigonish, NS, Canada

## ARTICLE INFO

### Article history:

Received 27 November 2013  
Received in revised form 23 April 2014  
Accepted 14 May 2014  
Available online 27 May 2014

### Keywords:

Optical sensor  
Gas sensor  
CO<sub>2</sub> sensor  
Long period grating  
Refractive index  
Coating

## ABSTRACT

A gas concentration sensor comprising a long period grating with a high refractive index coating is reported. The deposition of a high refractive index coating on the optical fiber allows a reorganization of the cladding modes which leads to a substantial increase in the sensitivity to the surrounding refractive index. To maximize the grating sensitivity in the vicinity of the refractive index of CO<sub>2</sub>, the grating was coated with a 365 nm layer of polystyrene. The results show that the sensor is able to distinguish between the CO<sub>2</sub> and N<sub>2</sub> gases with high reproducibility and reversibility. The sensitivity of the sensor is 1.23 pm/%CO<sub>2</sub>.

© 2014 Elsevier B.V. All rights reserved.

## 1. Introduction

A wide range of techniques for the measurement of gas concentration have been developed for applications including chemical and mining safety [1], medical diagnosis [2], design and operation of modern lasers [3] and environment monitoring [4]. Among these techniques, there are a number of well-established optical methods to measure gas concentrations, including absorption spectroscopy [5], fluorescence spectroscopy [6,7], interferometry [8], surface plasmon resonance [9] and grating-based index transduction [10–14].

With respect to optical grating-based sensors, several configurations based on the interaction between a specific gas and a coating material deposited on a long period grating (LPG) inscribed in single mode fibers have been proposed. These include a sol-gel derived SnO<sub>2</sub> film for C<sub>2</sub>H<sub>5</sub>OH detection [10], palladium films for H<sub>2</sub> sensing [15], films fabricated by nanoassembly of polyelectrolytes for ammonia sensing [16], and zeolite films for organic vapor measurements such as isopropanol and toluene [17].

The coating of an LPG with a high refractive index (RI) layer can also be applied to enhance the sensitivity of the grating to

the surrounding refractive index (SRI) [18]. The coating promotes a transition in which cladding guided modes are coupled to the coating guided mode by a phenomenon referred to as “transition mode” [18–20]. The coupling of the cladding modes to the coating mode increases the intensity of the evanescent field at the interface between the coating and the surrounding medium [20]. As a consequence, the sensitivity of a coated LPG to the SRI increases significantly when compared with a bare LPG.

For a given refractive index and coating thickness, there is a unique value of SRI at which this transition occurs [20]. Therefore, for a target SRI measurement, it is possible to tune the thickness of the coating to maximize the sensitivity of the grating. Both numerical and experimental studies of coated LPGs operating in transition mode have been conducted by Pilla et al., leading to a sensor with sensitivity of 9000 nm/RIU [21].

The transition mode phenomenon can also be used in combination with the sorption properties of the coating layer [22,23]. Sorption leads to the increase of the material density which increases the refractive index of a coating [24].

In the current study, the investigation of the transition mode in coated LPGs is extended to the case where the surrounding medium is a gas (i.e. for an SRI in the vicinity of 1.0). The thickness of the coating that enhances the sensitivity of LPGs in gas region is investigated. Experiments are performed by measuring wavelength shifts caused by different concentrations of CO<sub>2</sub> and N<sub>2</sub> gases.

\* Corresponding author. Tel.: +1 2507216292.  
E-mail address: [luismelo@uvic.ca](mailto:luismelo@uvic.ca) (L. Melo).

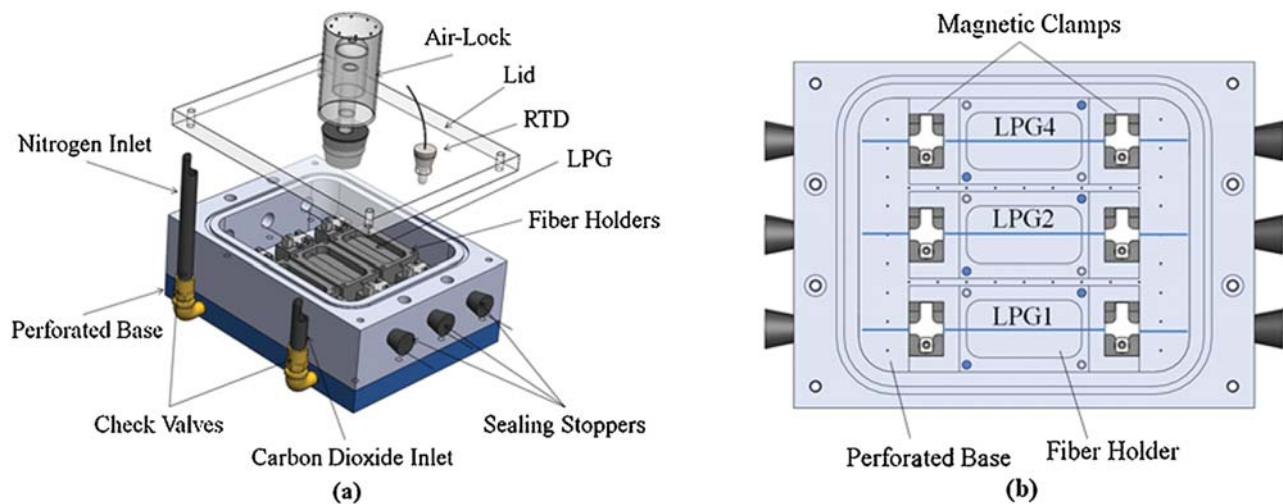


Fig. 1. (a) The test chamber, (b) a top view of the chamber.

## 2. Experimental methods

### 2.1. Fabrication and characterization of coated LPGs

Four commercial gratings (LPG1, LPG2, LPG3, LPG4), each with a period of  $450\ \mu\text{m}$  and a length of 10 mm (Technica S.A., Beijing) inscribed in Corning single mode fiber, SMF-28e were used in this work. LPG1 was not coated whereas LPG2, LPG3 and LPG4 were coated with atactic polystyrene (molecular weight 280,000; Sigma–Aldrich) using a dip coating technique. The RI of the bulk polystyrene is 1.59, as specified by the supplier. The coating thickness was measured with a scanning electron microscope (Hitachi S-4800). The details of these measurements are reported elsewhere [25].

The response to SRI of each of the coated LPGs was characterized using glycerin solutions over a refractive index range from 1.3328 to 1.4720. These RI measurements were made with an Abbe refractometer at 589 nm with a resolution of  $1 \times 10^{-4}$  RI units.

A broadband light source (ASLD-CWDM-5-B-FA, Amonics, China) provided light to the grating. The transmission spectrum was interrogated with an optical spectrum analyzer (Yokogawa, AQ 6331) over the range 1250–1650 nm with a resolution of 0.5 nm.

The temperature responses of LPG1 and the three coated LPGs were characterized by placing the gratings in an oven and incrementing the temperature in steps of  $3\ ^\circ\text{C}$ . The temperature was measured with an RTD (RTD-NPT-72-E, Omega, USA) providing a resolution of  $0.1\ ^\circ\text{C}$ . For the temperature characterization, the resonant wavelength of the LPGs was monitored using ENLIGHT software and a Micron Optics sm125 interrogator with a resolution of 1 pm and a scan frequency of 2 Hz. The four LPGs were tested at the same time and two trials were performed to ensure the reproducibility of the results.

### 2.2. Gas testing

A test chamber was fabricated with a volume of 783 ml, as shown in Fig. 1. The gratings were held under constant tension using magnetic clamps. The fibers pass through holes in the chamber wall which are sealed using rubber stoppers. Gases are introduced to the chamber through the perforated base. The chamber has a transparent lid that is sealed with an O-ring. A water-filled air lock is used to maintain atmospheric pressure and prevent backflow of air into the chamber.

The resonant wavelength of the LPGs was monitored during the gas testing with the Micron Optics interrogator. The temperature

in the test chamber was measured with the same RTD as in the temperature characterization of the gratings.

In the first experiment, pure  $\text{N}_2$  and pure  $\text{CO}_2$  (industrial purity, Praxair, Canada) gases were used. Each of the gases was introduced into the test chamber in sufficient volume to ensure that all of the preceding gas was purged from the chamber. Two trials were performed. In the first trial, LPG1, LPG2 and LPG4 were interrogated. In the second trial LPG1, LPG3 and LPG4 were interrogated. A step-by-step description of the procedure is shown in Table 1.

A second experiment was conducted using prepared industrial mixtures of  $\text{CO}_2/\text{N}_2$  (Praxair, Canada) having 24.93%, 49.92% and 74.98% (nominally, 25%, 50% and 75%, respectively)  $\text{CO}_2$  by mass, respectively. Only LPG4 was used in this experiment. Each of these prepared mixtures was introduced into the test chamber in sufficient volume to ensure that all of the preceding mixture was purged from the chamber. Between tests with each of the prepared mixtures, the chamber was purged with 100%  $\text{CO}_2$ . At the end of the trial, the rig was purged with  $\text{N}_2$  and a second trial was performed. A step-by-step description of the procedure is shown in Table 2.

## 3. Results and discussion

### 3.1. Characterization of coated LPGs

The mean thickness of the coatings for LPG2, LPG3 and LPG4, as measured by SEM, are 204 nm, 249 nm and 365 nm, respectively.

**Table 1**  
Experimental procedure used in the detection of pure  $\text{N}_2$  and  $\text{CO}_2$  gases.

| Step # | Duration                        | Injection gas               | Injection volume (ml) (at $25\ ^\circ\text{C}$ and 1 atm) |
|--------|---------------------------------|-----------------------------|---|
| 1      | 10 min                          | Air                         | 0   |
| 2      | 30 s                            | $\text{N}_2$                | $2360 \pm 118$  |
| 3      | 30 s                            | None                        | 0   |
| 4      | Repeat steps 2 and 3; six times |                             | $14,160 \pm 708$  |
| 5      | 4 min, 30 s                     | None – stabilization period | 0   |
| 6      | 30 s                            | $\text{CO}_2$               | $2360 \pm 118$  |
| 7      | 30 s                            | None                        | 0   |
| 8      | Repeat steps 6 and 7; six times |                             | $14,160 \pm 708$  |
| 9      | 4 min, 30 s                     | None – stabilization period |   |
| 10     | Repeat steps 2–9; six times     |                             |   |

**Table 2**  
Experimental procedure used to measure different concentrations of CO<sub>2</sub> with LPG4.

| Step # | Duration  | Injection gas               | Injection volume (ml) (±177 ml) |
|--------|---|-----------------------------|---------------------------------|
| 1      | 45 s  | 100% CO <sub>2</sub>        | 3538                            |
| 2      | 15 s  | None                        | 0                               |
| 3      | 45 s  | 100% CO <sub>2</sub>        | 3538                            |
| 4      | 3 min, 15 s   | None – stabilization period | 0                               |
| 5      | 45 s  | 75% CO <sub>2</sub>         | 3538                            |
| 6      | 15 s  | None                        | 0                               |
| 7      | 45 s  | 75% CO <sub>2</sub>         | 3538                            |
| 8      | 3 min, 15 s   | None – stabilization period | 0                               |
| 9      | Repeat steps 1–8; three times   |                             |                                 |
| 10     | Repeat steps 1–8 but with injection of 50% CO <sub>2</sub> in steps 5 and 7; repeat three times |                             |                                 |
| 11     | Repeat steps 1–8 but with injection of 25% CO <sub>2</sub> in steps 5 and 7; repeat three times |                             |                                 |
| 12     | Repeat steps 1–8 but with injection of N <sub>2</sub> in steps 5 and 7; repeat three times      |                             |                                 |

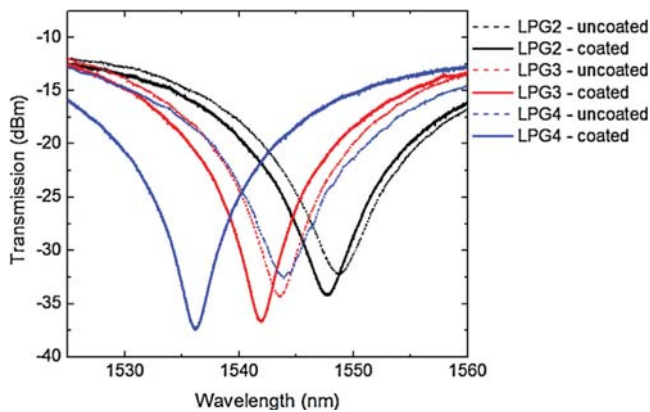


**Fig. 2.** Spectra of the coated LPGs before and after coating.

**Fig. 2** shows the transmission spectra of these LPGs in air before and after coating. LPG2, LPG3 and LPG4 exhibit blue shifts of 1.1 nm, 1.6 nm and 7.9 nm, respectively, due to coating.

The transmission spectra of LPG2 were recorded, during immersion in glycerin solutions over a range of concentrations and the associated SRI values. The transmission spectra of the grating were normalized by subtracting the spectrum of the light source. For each SRI, four attenuation bands associated with the linear polarized modes LP<sub>02</sub>, LP<sub>03</sub>, LP<sub>04</sub> and LP<sub>05</sub> are shown in **Fig. 3**. These attenuation bands are labeled by superscript. For example, 75<sup>05</sup> is mode LP<sub>05</sub> for a solution concentration of 75%. Note the mode LP<sub>05</sub> is initially out of the wavelength range of the OSA and only appears at an SRI of 1.4348. As the SRI increases, the resonance wavelength of

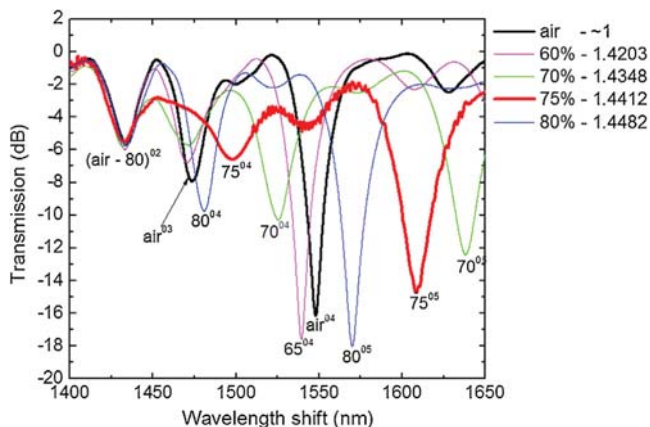


**Fig. 3.** Transition mode of LPG2 for a coating thickness of 204 nm. The first column of the legend shows the concentrations of glycerin solutions (in percentage); the second column of the legend shows the refractive index of glycerin solutions (SRI).

mode LP<sub>05</sub> decreases until it reaches the original resonance wavelength of mode LP<sub>04</sub> (i.e. air<sup>04</sup>). Similarly, the attenuation band of mode LP<sub>04</sub> decreases until it approaches the resonance wavelength of mode LP<sub>03</sub> that corresponds to the SRI of air (i.e. air<sup>03</sup>).

Also shown in **Fig. 3**, the attenuation band of mode LP<sub>03</sub> disappears when the SRI changes from 1.4348 (green line) to 1.4412 (red line). This corresponds to the transition point of mode LP<sub>03</sub>, at which point this mode is propagating in the coating. This transition causes a reorganization of the cladding modes in which cladding modes of higher order than that guided by the coating shift their wavelengths toward adjacent lower order cladding modes.

For LPG3, the amplitude of the attenuation band of mode LP<sub>03</sub> for a 55% solution (i.e. 55<sup>03</sup>) is significantly reduced at an SRI of 1.4132, as shown in **Fig. 4**. This corresponds to the transition point of mode LP<sub>03</sub>. To facilitate comparison with **Fig. 3**, the spectrum of LPG3 in the vicinity of the transition point is represented by the red line and the spectra at lower and higher concentrations, adjacent to transition, are represented by the green and blue lines, respectively.

For LPG4, shown in **Fig. 5**, the SRI at transition lies between 1.0 (air) and 1.3328 (water). Tests were not conducted for SRI values between those of air and water as substances with RIs in this range are not readily available. As LPG4 is moved from immersion in air to immersion in water, mode LP<sub>03</sub> disappears because it is coupled to the coating and mode LP<sub>04</sub> shifts to a wavelength that is close to the original resonance wavelength of mode LP<sub>03</sub> (i.e. air<sup>03</sup>). Transition mode behavior is also evident in mode LP<sub>05</sub>. As the SRI increases from the RI of water (0<sup>05</sup>) to 1.3920 (40<sup>05</sup>), the wavelength shift of mode LP<sub>05</sub> approaches the original wavelength of LP<sub>04</sub> (air<sup>04</sup>).

The phenomenon of transition mode was originally described as the coupling of the lowest order mode (i.e. LP<sub>02</sub>) to the coating

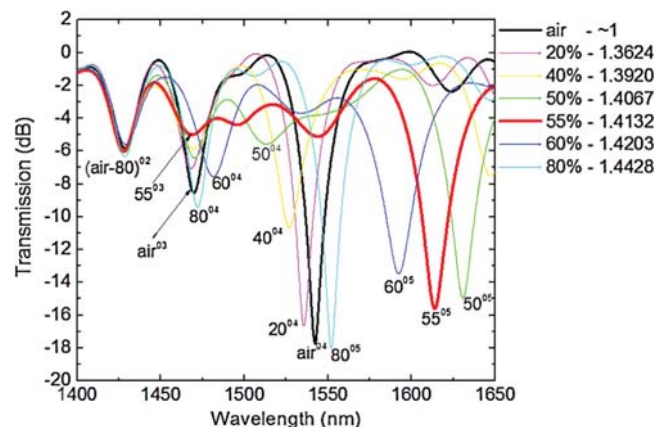


**Fig. 4.** Transition mode of LPG3 with a coating thickness of 249 nm. The first column of the legend shows the concentrations of glycerin solutions (in percentage); the second column of the legend shows the refractive index of glycerin solutions (SRI).

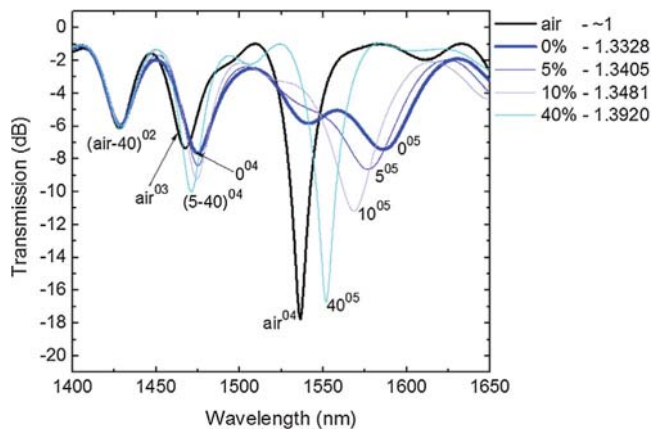


Fig. 5. Transition mode of LPG4 with a coating thickness of 365 nm. The first column of the legend shows the concentrations of glycerin solutions (in percentage); the second column of the legend shows the refractive index of glycerin solutions (SRI).

[19]. However, the lowest order mode,  $LP_{02}$ , in Figs. 3–5 does not change significantly with increasing SRI, indicating that this mode remains coupled to the cladding for all tested values of SRI. Villar et al. also observed the non-transition of mode  $LP_{02}$  to the coating for an LPG coated with PDDA<sup>+</sup>/PolyR-47<sup>-</sup> [26]. The authors conclude that, when the coating is characterized by an imaginary RI component (i.e. in addition to the real component of the RI) the mode guided by the coating is not necessarily the lowest order mode [26].

The resonance wavelengths of modes  $LP_{04}$  and  $LP_{05}$  for the coated LPGs are plotted as a function of the SRI in Fig. 6. Mode  $LP_{04}$  is of interest because, at the SRI of typical gases (i.e. close to 1.0), its resonance wavelength is within the spectral range of the optical interrogator used in these experiments.

In order to determine SRI sensitivity of the LPG2 and LPG3, a Lorentz fit was applied to the data for  $LP_{04}$  of LPG2 and LPG3, as shown in Fig. 6. The Lorentz fits are based on Equation (1),

$$\lambda(SRI) = \lambda_0 + \frac{2A}{\pi} \frac{w}{4(SRI - SRI_t)^2 + w^2} \quad (1)$$

where,  $\lambda_0$ , is the offset resonance wavelength of the LPG for a given mode ( $LP_{04}$ );  $SRI_t$ , is the value of SRI at which the transition occurs; and,  $w$ , and,  $A$ , are the full width at half maximum and the area of the Lorentzian curve, respectively. The absolute value of the first derivative of each Lorentz fit,  $|d\lambda/dSRI|$ , is then calculated for LPG2 and LPG3 and plotted in Fig. 7. This first derivative represents the sensitivity of the LPG to SRI.

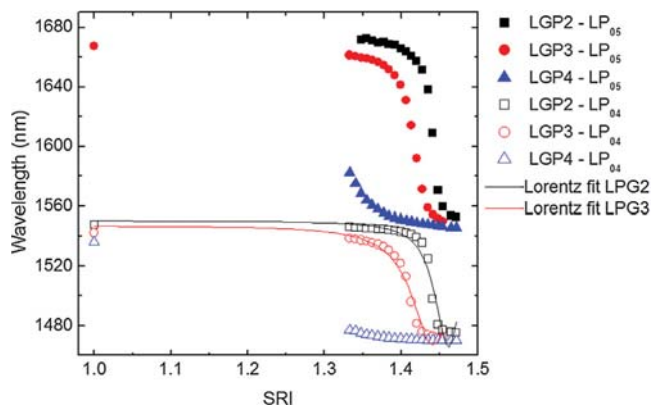


Fig. 6. Resonance wavelength as a function of surrounding refractive index (SRI) for LPG2, LPG3 and LPG4. Full marks represent the  $LP_{05}$  and open marks represent the  $LP_{04}$ .

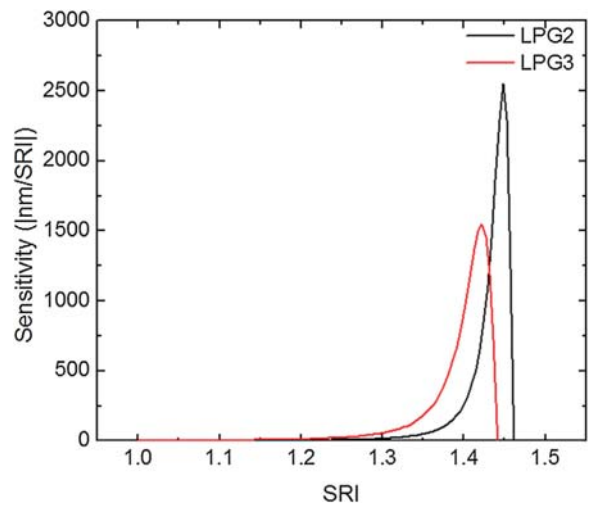


Fig. 7. Sensitivity curves of the  $LP_{04}$  for the LPG2 and LPG3.

The maximum sensitivities of LPG2 and LPG3, which correspond to the transition point, occur at SRI values of 1.4482 and 1.4224, respectively. The sensitivity curve for LPG4 cannot be obtained due to the lack of data in the transition region. However, assuming that the response of LPG4 is similar in form to that of LPG2 and LPG3, Fig. 6 suggests that LPG4 provides a region of high sensitivity (i.e. transition) at relatively low SRI.

The temperature sensitivity of the gratings is shown in Table 3. These values are within the temperature sensitivities reported in the literature for LPGs inscribed in SMF-28e fiber when surrounded by air [27,28].

### 3.2. Gas testing

Data from the first and second trials of the experiment with pure  $N_2$  and  $CO_2$  gases is shown in Figs. 8 and 9, respectively (step-by-step description is shown in Table 1). The vertical dashed lines represent the beginning of each gas injection (Table 1, steps 2 and 6). Both figures show that the resonance wavelength of LPG1 remains approximately constant during injections (black line). The resonance wavelength of LPG2 (Fig. 8, green line) increases 28 pm after the first injection of  $N_2$ . During subsequent injections, the resonance wavelength varies over a range of 30 pm but these variations do not coincide with gas injections. The resonance wavelength of LPG3 (Fig. 9, green line) shows a small correlation with the injection of the gases, however, the signal-to-noise ratio of LPG3 is low.

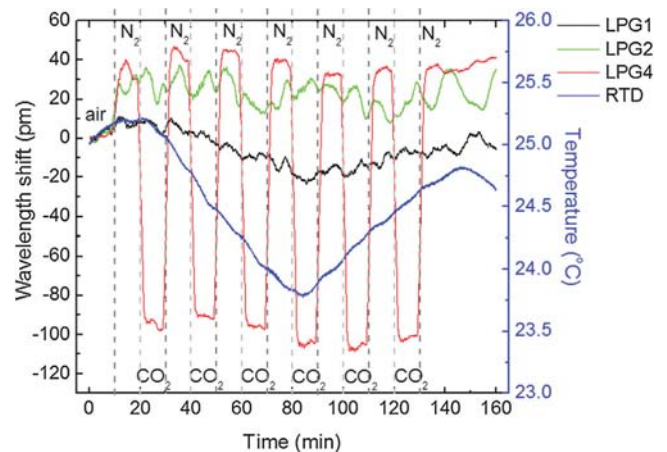


Fig. 8. Detection between pure  $N_2$  and  $CO_2$  with LPG1 and LPG2 and LPG4.

**Table 3**

Temperature sensitivity of the LPGs.

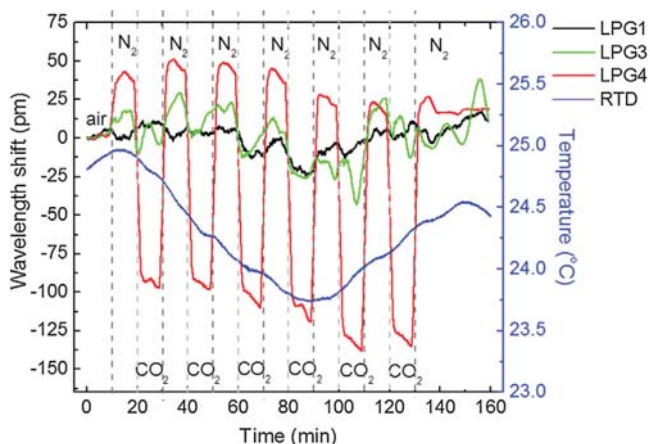
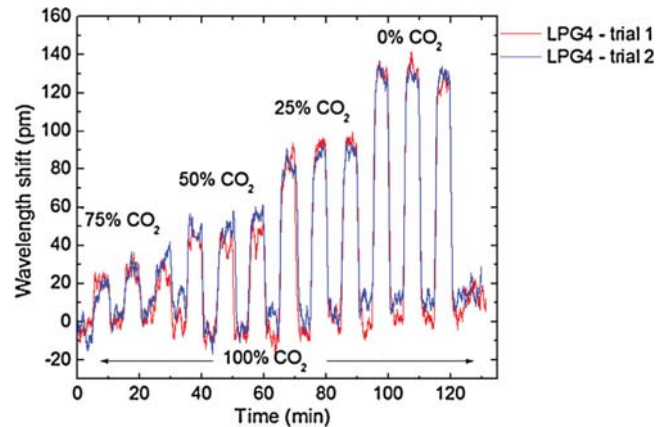
| LPG  | Trial 1 (pm/°C) | $r^2$   | Trial 2 (pm/°C) | $r^2$   | Mean of the sensitivity (pm/°C) |
|------|-----------------|---------|-----------------|---------|---------------------------------|
| LPG1 | 32.17           | 0.98778 | 33.57           | 0.99525 | 32.87                           |
| LPG2 | 36.75           | 0.99677 | 35.92           | 0.999   | 36.34                           |
| LPG3 | 34.64           | 0.99826 | 34.57           | 0.99838 | 34.61                           |
| LPG4 | 49.26           | 0.99321 | 49.44           | 0.99775 | 49.35                           |

The shifts in resonance wavelength of LPG4 (red line in Figs. 8 and 9) are coincident with injections of  $N_2$  and  $CO_2$ . The mean of the resonance wavelength of LPG4 was calculated for the stabilization period of each gas (Table 1, steps 5 and 9). These values were used to determine the magnitudes of a total of 24 wavelength shifts between  $N_2$  and  $CO_2$  and between  $CO_2$  and  $N_2$  from both trials. For LPG4, the mean of these wavelength shifts and its standard deviation are  $138 \pm 8$  pm.

The resonance wavelength of the coated LPGs used in this work decreases as SRI increases, as shown in Fig. 6. Noting that the RIs of  $N_2$  and  $CO_2$  are 1.00027 and 1.00029 (at  $1.55 \mu\text{m}$ ) [26], respectively, the wavelength shifts that occur at the transitions between  $CO_2$  and  $N_2$  (Figs. 8 and 9) for LPG4 are as expected. These figures also show that the resonance wavelength of LPG4 increases as air is displaced by  $N_2$  at the start of each trial. The RI of air, assuming 78%  $N_2$  and 21%  $O_2$ , is 1.00044 at  $1.55 \mu\text{m}$  [26]. Therefore, the resonance wavelength is expected to decrease, rather than increase as air is displaced by  $N_2$ . This result suggests that another phenomenon contributes to the wavelength shift of LPG4. This phenomenon may be sorption of gases into the polystyrene coating.

The use of polystyrene as a sorption coating layer on an LPG working in transition mode has been reported in previous studies [24,29]. These authors used a structural form of polystyrene (i.e.  $\delta$  syndiotactic polystyrene or s-PS) which has a crystalline domain characterized by a nanoporous structure with regularly spaced nanocavities. The authors conclude that compounds such as chloroform can be reversibly adsorbed by the nanocavities at the surface of the coating. The adsorption leads to the increase of the material density which increases the refractive index of the coating [24,29].

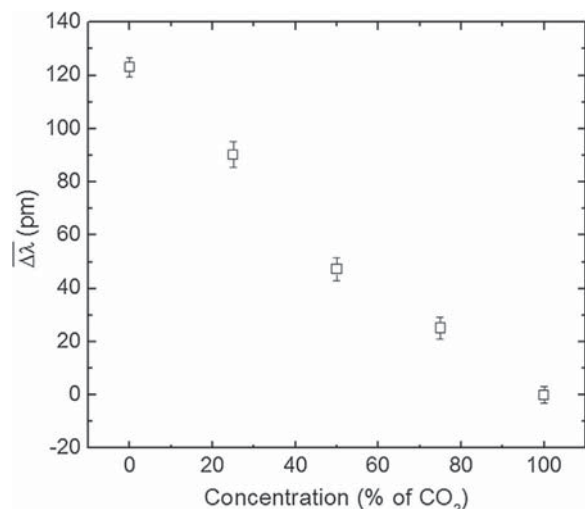
The coating used in this work is the amorphous phase of polystyrene, atactic polystyrene (a-PS), which is characterized by a smooth surface. Previous studies report that sorption into a-PS occurs by diffusion of the analyte through the polymer matrix whereas the sorption into s-PS occurs mainly at nanocavity sites on the surface of the polymer [30]. The authors observed that a-PS enables a lower level of sorption compared to s-PS [30]. Under pressures between 5 and 10 Torr and temperatures between 35 and

**Fig. 9.** Detection between pure  $N_2$  and  $CO_2$  with LPG1 and LPG3 and LPG4.**Fig. 10.** Wavelength shifts due to the change of  $CO_2$  concentration with time.

$56^\circ\text{C}$ , the sorption level of chloroform in a-PS is between 4 and 6 times lower than that for the s-PS [30,31].

The resonance wavelength shift between  $N_2$  and  $CO_2$  ( $138 \pm 8$  pm) shown in Figs. 8 and 9 may be, in part, due to the sorption of  $O_2$ ,  $N_2$  and/or  $CO_2$  into the a-PS matrix. This result confirms that the proposed  $CO_2$  sensor is based on the combination of the transition mode phenomenon with the sorption properties of a non-functionalized coating. In addition to previous work that investigated the same mechanism of detection [22,23], the work reported in this article shows that a measurable signal between different gases is only obtained if the transition point is tuned to relatively low range of SRI. Further investigation is needed to determine the amounts of each gas that are absorbed by the a-PS and their respective contributions to the observed wavelength shift.

The performance of LPG4 as a  $CO_2$  sensor was determined by observing the response of the LPG4 to a range of concentrations of  $CO_2$  (step-by-step description is shown in Table 2), as shown in Fig. 10. The wavelength shifts between each injection of pure  $CO_2$

**Fig. 11.**  $CO_2$  sensor characterization.

and each of the lower CO<sub>2</sub> concentrations were measured during the stabilization period (Table 2, steps 4 and 8). For each gas concentration, the mean wavelength shift and its standard deviation were determined by averaging the six wavelength shifts between the baseline/purge gas (*i.e.* 100% CO<sub>2</sub>) and the four test gases over the two trials. This data is presented in Fig. 11.

Based on a linear regression of the data presented in Fig. 11, the wavelength shift of LPG4 as a function of CO<sub>2</sub> concentration is  $-1.23 \pm 0.08$  pm/%CO<sub>2</sub> with  $r^2 = 0.985$ . The standard deviation of the data taken during the 3 min 15 s stabilization period at each concentration level is between 1 pm and 5 pm. Therefore, the worst case wavelength resolution is  $\pm 5$  pm. Using the measured sensitivity of 1.23 pm/%CO<sub>2</sub>, the sensor resolution is calculated as  $\pm 4.07\%$ CO<sub>2</sub>.

#### 4. Conclusions

The phenomenon of transition modes in LPGs was investigated experimentally. Three LPGs (LPG2, LPG3 and LPG4) were coated with polystyrene with coating thicknesses of 204 nm, 249 nm and 365 nm, respectively. The results of the SRI characterizations show that the transition points of LPG2 and LPG3 occur at RI values of 1.4482 and 1.4224, respectively. The coating thickness of LPG4 was tuned to provide transition at a lower SRI and, as a result, higher sensitivity at the RI of gases.

The experiments show that LPG4 was able to distinguish between N<sub>2</sub> and CO<sub>2</sub> with a resonance wavelength shift of  $138 \pm 8$  pm. The sensitivity of LPG4 to CO<sub>2</sub> concentration was shown to be  $1.23 \pm 0.08$  pm/%CO<sub>2</sub>.

The wavelength shift observed for the transition from air to N<sub>2</sub> is not consistent with the SRI effects alone. It is believed that this result is due to sorption of the gases into the polystyrene coating.

The high sensitivity of LPG4 to N<sub>2</sub> and CO<sub>2</sub>, relative to the sensitivities of LPG2 and LPG3, shows that, to achieve an effective concentration sensor, it is critical to promote a transition mode that occurs at an RI that is close to the RI's of the target gases. This allows high sensitivity to both SRI and RI changes of the coating.

#### Acknowledgments

The authors gratefully acknowledge funding provided by the Natural Sciences and Engineering Research Council of Canada (NSERC), and Carbon Management Canada.

#### References

- [1] J.C. Hower, K. Henke, J.M.K. O'Keefe, M.A. Engle, D.R. Blake, G.B. Stracher, The Tiptop coal-mine fire, Kentucky: preliminary investigation of the measurement of mercury and other hazardous gases from coal-fire gas vents, *Int. J. Coal Geol.* 80 (2009) 63–67.
- [2] S. Ryabtsev, A. Shaposhnick, A. Lukin, E. Domashevskaya, Application of semiconductor gas sensors for medical diagnostics, *Sens. Actuators, B Chem.* 59 (1999) 26–29.
- [3] Á. Börzsönyi, Z. Heiner, A.P. Kovács, M.P. Kalashnikov, K. Osvay, Measurement of pressure dependent nonlinear refractive index of inert gases, *Opt. Express.* 18 (2010) 25847–25854.
- [4] D. Risk, L. Kellman, H. Beltrami, A new method for in situ soil gas diffusivity measurement and applications in the monitoring of subsurface CO<sub>2</sub> production, *J. Geophys. Res.* 113 (2008) G02018.
- [5] D. Liu, S. Fu, M. Tang, P. Shum, D. Liu, Comb filter-based fiber-optic methane sensor system with mitigation of cross gas sensitivity, *J. Light. Technol.* 30 (2012) 3103–3109.
- [6] P.-L. Ong, I.A. Levitsky, Fluorescent gas sensors based on nanoporous optical resonators (microcavities) infiltrated with sensory emissive polymers, *IEEE Sens. J.* 11 (2011) 2947–2951.
- [7] J. Zaharieva, M. Milanova, D. Todorovsky, SiO<sub>2</sub>/polyester hybrid for immobilization of Ru(II) complex as optical gas-phase oxygen sensor, *J. Mater. Chem.* 21 (2011) 4893.
- [8] J. Liu, Y. Sun, X. Fan, Highly versatile fiber-based optical Fabry-Pérot gas sensor, *Opt. Express.* 17 (2009) 2731–2738.

- [9] P.R. Ohodnicki, M.P. Buric, T.D. Brown, C. Matranga, C. Wang, J. Baltrus, et al., Plasmonic nanocomposite thin film enabled fiber optic sensors for simultaneous gas and temperature sensing at extreme temperatures, *Nanoscale* 5 (2013) 9030–9039.
- [10] Z. Gu, Y. Xu, K. Gao, Optical fiber long-period grating with sol-gel coating for gas sensor, *Opt. Lett.* 31 (2006) 2405–2407.
- [11] X. Jiang, Z. Gu, Design of a gas sensor based on a sensitive film coated phase-shifted long-period fiber grating, *J. Opt.* 12 (2010) 075401.
- [12] F. Tian, Z. He, H. Du, Numerical and experimental investigation of long-period gratings in photonic crystal fiber for refractive index sensing of gas media, *Opt. Lett.* 37 (2012) 380–382.
- [13] F. Tian, J. Kanka, H. Du, Long-period grating and its cascaded counterpart in photonic crystal fiber for gas phase measurement, *Opt. Express.* 20 (2012) 20951–20961.
- [14] J. Kanka, Design of turn-around-point long-period gratings in a photonic crystal fiber for refractometry of gases, *Sens. Actuators, B Chem.* 182 (2013) 16–24.
- [15] X. Wei, T. Wei, H. Xiao, Y.S. Lin, Nano-structured Pd-long period fiber gratings integrated optical sensor for hydrogen detection, *Sens. Actuators, B Chem.* 134 (2008) 687–693.
- [16] T. Wang, S. Korposh, S. James, R. Tatam, S.-W. Lee, Optical fibre long period grating sensor with a polyelectrolyte alternate thin film for gas sensing of amine odors, *Sens. Actuators, B Chem.* 185 (2013) 117–124.
- [17] J. Zhang, X. Tang, J. Dong, T. Wei, H. Xiao, Zeolite thin film-coated long period fiber grating sensor for measuring trace organic vapors, *Sens. Actuators, B Chem.* 135 (2009) 420–425.
- [18] N.D. Rees, S.W. James, R.P. Tatam, G.J. Ashwell, Optical fiber long-period gratings with Langmuir-Blodgett thin-film overlays, *Opt. Lett.* 27 (2002) 686–688.
- [19] I. Del Villar, I. Matías, F. Arregui, P. Lalanne, Optimization of sensitivity in long period fiber gratings with overlay deposition, *Opt. Express.* 13 (2005) 56–69.
- [20] A. Cusano, P. Pilla, L. Contessa, A. Iadicicco, S. Campopiano, A. Cutolo, et al., High-sensitivity optical chemosensor based on coated long-period gratings for sub-ppm chemical detection in water, *Appl. Phys. Lett.* 87 (2005) 234105.
- [21] P. Pilla, C. Trono, F. Chiavaioli, M. Giordano, A. Cusano, Giant sensitivity of long period gratings in transition mode near the dispersion turning point: an integrated design approach, *Opt. Lett.* 37 (2012) 4152–4154.
- [22] A. Cusano, A. Iadicicco, P. Pilla, L. Contessa, S. Campopiano, A. Cutolo, et al., Cladding mode reorganization in high-refractive-index-coated long-period gratings: effects on the refractive-index sensitivity, *Opt. Lett.* 30 (2005) 2536–2538.
- [23] S.M. Topliss, S.W. James, F. Davis, S.P.J. Higson, R.P. Tatam, Optical fibre long period grating based selective vapour sensing of volatile organic compounds, *Sens. Actuators, B Chem.* 143 (2010) 629–634.
- [24] M. Giordano, M. Russo, A. Cusano, A. Cutolo, G. Mensitieri, L. Nicolais, Optical sensor based on ultrathin films of  $\delta$ -form syndiotactic polystyrene for fast and high resolution detection of chloroform, *Appl. Phys. Lett.* 85 (2004) 5349.
- [25] L. Melo, G. Burton, S. Warwick, P. Wild, Experimental investigation of long period grating working in transition mode, *SPIE - 23rd Int. Conf. Opt. Fiber Sensors OFS23* 9157 (2012), <http://dx.doi.org/10.1117/12.2059464> (in press).
- [26] I. Del Villar, I.R. Matias, S. Member, F.J. Arregui, M. Achaerandio, Nanodeposition of Materials With Complex Refractive Index in Long-Period Fiber Gratings, *23, 2005*, pp. 4192–4199.
- [27] V. Bhatia, A.M. Vengsarkar, Optical fiber long-period grating sensors, *Opt. Lett.* 21 (1996) 692–694.
- [28] G. Humbert, A. Malki, Electric-arc-induced gratings in non-hydrogenated fibres: fabrication and high-temperature characterizations, *J. Opt. A Pure Appl. Opt.* 4 (2002) 194–198.
- [29] P. Pilla, A. Iadicicco, L. Contessa, S. Campopiano, A. Cutolo, M. Giordano, et al., Optical chemo-sensor based on long period gratings coated with  $\delta$ -form syndiotactic polystyrene, *IEEE Photonics Technol. Lett.* 17 (2005) 1713–1715.
- [30] G. Mensitieri, D. Larobina, G. Guerra, V. Venditto, M. Fermeiglia, S. Priel, Chloroform Sorption in Nanoporous Crystalline and Amorphous Phases of Syndiotactic Polystyrene, *J. Polym. Sci. Pol. Phys.* 46 (2008) 8–15.
- [31] G. Mensitieri, V. Venditto, G. Guerra, Polymeric sensing films absorbing organic guests into a nanoporous host crystalline phase, *Sens. Actuators, B Chem.* 92 (2003) 255–261.

#### Biographies

**Luis Melo** received his M.Sc. degree in Physics Engineering from the University of Aveiro, Portugal in 2010. Currently, he is pursuing his Ph.D. degree in Mechanical Engineering at the University of Victoria in British Columbia, Canada, conducting his research in fiber optic sensors for detection of CO<sub>2</sub>. His areas of research include optoelectronic sensors for the detection of chemical species and materials characterization by scanning electron microscopy.

**Geoff Burton** received his Bachelor's degree in mechanical engineering in 2012 from the University of Victoria, Canada. Since then, he has worked as a research engineer at IESVIC, the Institute for Integrated Energy Systems at the University of Victoria. His research is focused on fiber optic sensor design for the detection of chemical species.

**Benjamin Davies** received his B.Sc. in Biological Engineering from the University of Guelph in Ontario, Canada in 2006. Currently, he is pursuing his M.Sc. degree in Mechanical Engineering at the University of Victoria in British Columbia, Canada.

conducting his research in polymeric gas separation membranes for optical liquid/gas sensors. His areas of research include: optical fiber sensors for chemical species detection; polymeric membranes for CO<sub>2</sub> separation; and composite gas separating membranes.

**David Risk** is a Professor in the Department of Earth Sciences at the St. Francis Xavier University. He is a young Discovery-award-winning scientist whose training and interests lie within the ecological sciences, at the interface between physics and biogeochemistry. He is methodologically focused, and most of his research funding (>90%) is for applied industrial research that involves gas analysis, instrument and gas sensor design, and innovative monitoring strategies. Dr. Risk has expertise in

greenhouse gas emissions from soils. He had developed a new method for gas diffusivity measurements in soils with application to the monitoring of subsurface CO<sub>2</sub> flux.

**Peter Wild** is a Professor in the Department of Mechanical Engineering at the University of Victoria. He holds the Natural Sciences and Engineering Research Council (NSERC) Chair in Sustainable Energy Systems Design and is the Director of the Institute for Integrated Energy Systems at UVic (IESVic). Dr. Wild's research interests include: optical sensors for industrial, environmental and biomedical applications; impacts of integration of renewable energy generation into existing grids; and renewable energy generation technologies.

## **Appendix B: Experimental Investigation of Long-Period Grating Transition Modes to Monitor CO<sub>2</sub> in High-Pressure Aqueous Solutions**

L. Melo, G. Burton, S. Warwick, and P. M. Wild, “Experimental Investigation of Long-Period Grating Transition Modes to Monitor CO<sub>2</sub> in High-Pressure Aqueous Solutions,” *J. Light. Technol.*, vol. 33, no. 12, pp. 2554–2560, 2015.

Reprinted, with permission, from *Journal of Lightwave Technology*, © 2015 IEEE and  
The Optical Society (OSA)

In reference to IEEE copyrighted material which is used with permission in this thesis, the IEEE does not endorse any of [university/educational entity's name goes here]'s products or services. Internal or personal use of this material is permitted. If interested in reprinting/republishing IEEE copyrighted material for advertising or promotional purposes or for creating new collective works for resale or redistribution, please go to:

[http://www.ieee.org/publications\\_standards/publications/rights/rights\\_link.html](http://www.ieee.org/publications_standards/publications/rights/rights_link.html)

to learn how to obtain a License from RightsLink

# Experimental Investigation of Long-Period Grating Transition Modes to Monitor CO<sub>2</sub> in High-Pressure Aqueous Solutions

Luis Melo, Geoff Burton, Stephen Warwick, and Peter M. Wild

**Abstract**—An experimental investigation of transition modes of long-period gratings (LPG) is reported. Coating LPGs with a material of high refractive index causes a reorganization of the cladding modes, leading to a substantial increase in sensitivity to changes in the surrounding refractive index (SRI). The sensitivity of a coated LPG to SRI over a given range of SRI is a function of coating thickness. In this study, the thickness of polystyrene coatings applied by dip coating was measured by scanning electron microscopy. The LPG sensors were used to monitor dissolution of liquid CO<sub>2</sub> in deionized water at high pressure, simulating use of the sensors to monitor geologically sequestered CO<sub>2</sub> in a deep aquifer.

**Index Terms**—Carbon dioxide, long period grating, sensor, transition mode.

## I. INTRODUCTION

CARBON capture and sequestration (CCS) has been identified as an attractive solution for large-scale reduction of CO<sub>2</sub> emissions [1]. CCS comprises the capture of CO<sub>2</sub> from major emission sources, such as coal power plants, and its subsequent injection and long term storage in underground storage reservoirs, such as saline aquifers. Saline aquifers deeper than 800 m are suitable for CO<sub>2</sub> storage because at these depths, the pressure is sufficient so that CO<sub>2</sub> can be stored in a high density state (i.e., either liquid or supercritical state) [1]. However, there are legitimate concerns that sequestered CO<sub>2</sub> may leak into groundwater or to the surface leading to increased atmospheric CO<sub>2</sub> concentrations as well as possible adverse health impacts [2].

Current methods to monitor underground CO<sub>2</sub> storage sites are based on subsurface, near-surface, and atmospheric measurements. Subsurface monitoring systems include seismic, gravimetric, electromagnetic methods, and downhole fluid sampling analysis [3], [4]. Subsurface fluid sampling is challenging because as samples are collected from these geological formations, CO<sub>2</sub>, brine, and hydrocarbons density-separate; properties such as temperature and solubility change; and CO<sub>2</sub> degas from the liquid phase [4]. Near-surface and atmospheric methods include groundwater chemistry monitoring, soil gas

isotopic analysis, and remote sensing of surface deformations [3], [4]. Common limitations of subsurface, near-surface, and atmospheric monitoring methods include relatively low resolution, high cost, and the inability to monitor continuously over the long time scales of CCS projects [3]–[5]. Fiber optic sensors (FOS) have emerged as an attractive solution to overcome these limitations.

A number of FOS have been developed to measure concentrations of CO<sub>2</sub> at atmospheric pressure. These sensors are based on three different detection methods, namely fluorescence [6], [7], absorption [8], [9] and refractive index (RI) [10]–[13].

Fluorescence based sensors use pH sensitive dyes coated onto the core [6] or tip [7] of an optical fiber. When CO<sub>2</sub> dissolves in water, it forms carbonic acid which interacts with the pH sensitive dyes. The result is a reduction in the fluorescence intensity at a specific wavelength. Constraints associated with fluorescence based measurements for downhole applications include storage of the sensor in buffer solutions and leaching of the dye [7].

Absorption based sensors use an optical fiber to direct the light from the laser source to interact with CO<sub>2</sub>. CO<sub>2</sub> has a strong absorption band at the wavelength region of 2 μm, therefore, the intensity of the transmitted signal is a function of gas concentration [8], [9]. Soukup *et al.* demonstrated an absorption based sensor to monitor concentration of CO<sub>2</sub> gas in a controlled release field test in Montana, USA [8].

Recently, a number of RI sensors have been developed to detect or monitor CO<sub>2</sub> gas. Pevec and Donlagic. report a sensor based on a Fabry–Perot interferometer which comprises a nanowire spliced onto the tip of an optical fiber [10]. Shivananju *et al.* report a CO<sub>2</sub> sensor using carbon nanotubes coated on the core of a Bragg grating [11]. Sensors that require reduction of the fiber diameter [10], [11], are not well-suited for CCS applications because the fiber becomes brittle. Melo *et al.* demonstrated a coated long period grating (LPG) with increased sensitivity in the RI region of gases for monitoring concentrations of CO<sub>2</sub>/N<sub>2</sub> [12].

None of the sensors described above has been used to measure liquid or supercritical CO<sub>2</sub> at high pressure (i.e., the conditions of subsurface monitoring in deep saline aquifers [1]).

Measurement of CO<sub>2</sub> at high pressure has been demonstrated using fiber optic tips based on Fresnel reflection [13]. This type of sensors has only been applied to distinguish between different phases (i.e., gas, liquid or supercritical). The utilization of fiber tip sensors to monitor CO<sub>2</sub> concentrations in aqueous solutions is a challenge due to the low sensitivity of these devices to the surrounding refractive index (SRI).

Manuscript received September 14, 2014; revised November 11, 2014; accepted December 12, 2014. Date of publication December 17, 2014; date of current version April 29, 2015. This work was supported by the Natural Sciences and Engineering Research Council of Canada, by the Carbon Management Canada, and by the Korean Carbon Capture and Sequestration R&D Center.

The authors are with the Department of Mechanical Engineering, University of Victoria, Victoria, BC V8W 3P6, Canada (e-mail: luismelo@uvic.ca; burtong@uvic.ca; swarwick@uvic.ca; pwild@uvic.ca).

Color versions of one or more of the figures in this paper are available online at <http://ieeexplore.ieee.org>.

Digital Object Identifier 10.1109/JLT.2014.2383356

0733-8724 © 2014 IEEE. Personal use is permitted, but republication/redistribution requires IEEE permission.

See [http://www.ieee.org/publications\\_standards/publications/rights/index.html](http://www.ieee.org/publications_standards/publications/rights/index.html) for more information.

Recently, a FOS based on an LPG was reported by Bao *et al.* for detection of CO<sub>2</sub> at high pressure for carbon sequestration applications [14]. The sensor is able to distinguish between brine and supercritical CO<sub>2</sub>, as well as between brine and supercritical CO<sub>2</sub>-saturated brine. However, the low SRI sensitivity of LPGs in the vicinity of water [15] limits the applicability of LPGs as a monitoring tool for sequestered CO<sub>2</sub>.

The SRI sensitivity of LPGs can be enhanced by coating the grating region with a material that has a higher RI than the fiber cladding [16], [17]. The coating promotes a transition in which cladding guided modes are coupled to the coating guided mode by a phenomenon referred to as *transition modes* [18]. At a given thickness and RI of the coating, there is a unique SRI value at which a lower order cladding mode is guided by the coating (i.e., transition point) [17]. This causes a reorganization of the cladding modes, which leads to significant wavelength shifts of the attenuation bands in the range of the SRIs around the transition point (i.e., transition region) [19].

This article presents an expanded study, based on our previous work [20], dealing with transition modes of LPGs coated by the dip-coating technique with a focus on increased sensitivity for CO<sub>2</sub> detection at high pressure. The relationship between the concentration of polystyrene in the coating solution and the coating thickness is investigated. LPGs with coatings of different thickness are then tested, and the wavelength shift of the attenuation bands is analyzed. A highly sensitive LPG is used to monitor dissolution of liquid CO<sub>2</sub> in water at 1400 lbf/in<sup>2</sup> and 25 °C. This work presents a novel contribution of FOS for application in subsurface monitoring of CO<sub>2</sub> storage sites.

## II. EXPERIMENTAL METHODS

### A. Coating Method

The dip-coating method was used to coat standard single mode optical fibers (SMF-28e) with atactic polystyrene (Molecular weight 280 000, Sigma-Aldrich, USA). A dip-coating apparatus was designed which allowed vertical withdrawal of the fiber through a polystyrene solution. The withdrawal velocity used in this work was 10 cm/min. Several solutions of polystyrene in chloroform were prepared: 6%, 7%, 8%, 8.5%, 9%, 9.5% and 10% by weight.

### B. Measurement of Coating Thickness

Optical fiber, without an LPG, was cleaned with boiling chloroform to remove the acrylate coating. Three fiber samples were coated using each of the seven polystyrene solutions. In each case, the coating was applied to 10 cm of fiber length. After dip-coating, the fibers were cured at room temperature for 24 h. Each fiber sample was cleaved using a mechanical cleaver at three different sections, at the mid-point of the coated region (5 cm) and at points located 2 cm on either side of the mid-point (3 and 7 cm).

The fiber sections were mounted in a 90° stub configuration that allows imaging of the cleaved end by scanning electron microscopy (SEM) (Hitachi S-4800). The SEM imaging

was performed at a voltage of 1 keV, emission current of 10 μA, working distance of 4 mm and magnifications between 150 000–200 000 times, depending on the coating thickness.

For each fiber section, images of the coating cross-section were acquired at eight different positions around the circumference of the cleaved fiber surface. Within each image, the coating thickness was measured at five different locations. The mean coating thickness of each fiber section ( $D_{\text{section}}$ ) and its standard deviation ( $\sigma_{\text{section}}$ ) were calculated from the five measurements taken from each of the eight SEM images (i.e., a total of 40 measurements).

The mean coating thickness and its standard deviation from each percentage of polystyrene solutions were calculated from a total of 360 measurements per solution. For each polystyrene solution, the measurements came from the three fiber samples, each with three cleaved fiber sections. Each fiber section had eight SEM images from which five thickness measurements were made per image.

### C. Sensor Fabrication and Characterization

Commercial LPGs with a period of 450 μm and a length of 10 mm (Technica S.A, Beijing) inscribed in Corning single mode fiber, SMF-28e, were used in these experiments. Five LPGs were coated with polystyrene solutions having concentrations of 8.0%, 8.5%, 9.0%, 9.5% and 10%, respectively. The LPGs were characterized after coating with glycerin solutions over an SRI range from 1.3328 to 1.4720, as measured by an Abbe refractometer at 589 nm. The full transmission spectrum of the LPGs was obtained with a white light source (Yokogawa, AQ4305) and an optical spectrum analyzer (Yokogawa, AQ 6331) over the range 1200 nm – 1700 nm with a resolution of 0.5 nm. To obtain a spectrum with higher resolution over a narrower bandwidth, an optical interrogator (sm 125, Micron Optics, USA) with a resolution of 1 pm over the wavelength range of 1510–1590 nm was used.

### D. Monitoring Carbon Dioxide Dissolution in Water at High Pressure

A schematic of the experimental setup for CO<sub>2</sub> testing is shown in Fig. 1. The main unit is a custom-built high pressure test chamber which is shown in a close up in Fig. 2(a). The test chamber consists of a top and a bottom section made of anodized aluminum, with a cylindrical section made of 316 stainless steel. Independent spools made of anodized aluminum (see Fig. 2(b)) were built which allow installation of two FOS in each spool.

Referring to Fig. 1, the inlet line consists of a siphon with drawn CO<sub>2</sub> cylinder (Praxair, Industrial purity 99.5%) which stores CO<sub>2</sub> in a liquid state at approximately 800 lbf/in<sup>2</sup>, and a manual high pressure pump 1 (87-6-5, High Pressure Company). The outlet line consists of a helium (He) cylinder (Praxair, 5.0 Purity) which stores He at 1400 lbf/in<sup>2</sup>, and manual high pressure pump 2 (87-6-5, High Pressure Company). The He cylinder was used to keep the pressure constant during the experiments. This cylinder is connected to valve 3 using a long and narrow tube (i.e., 9.25 m length of 1/16" [1.589 mm] outer diameter [OD] stainless tube) to avoid diffusion of He into the test cham-

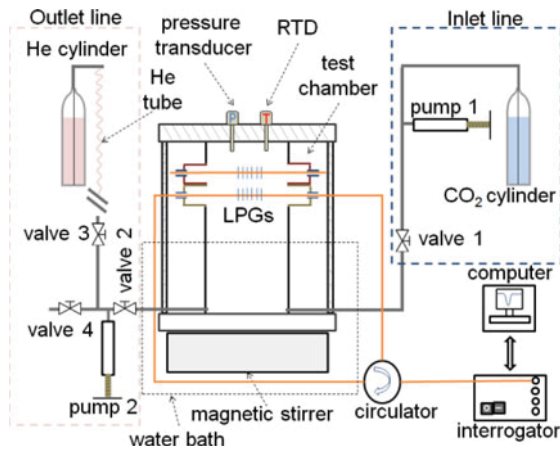


Fig. 1. Experimental setup for CO<sub>2</sub> testing.

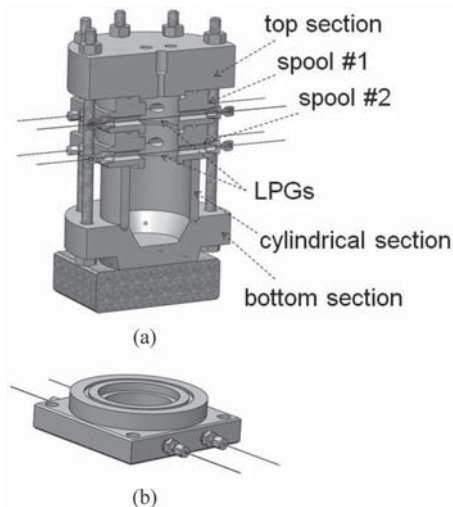


Fig. 2. (a) Drawing of the test chamber for CO<sub>2</sub> testing. (b) Close up of a spool.

ber (see He tube in Fig. 1). Pump 1 and pump 2 are manual piston pumps with a rotary crank actuator which can be used to pressurize a liquid inside the pump. All the connection lines are 1/8" (3.175 mm) OD 316 stainless steel tube (gray lines in Fig. 1).

A bare and a coated LPG were installed in the spools of the test chamber, as shown in Fig. 2(a). The LPGs were spliced into Corning single mode fibers with polyamide coating. The fiber was fed through the spool with two PEEK sleeves (1/16" [1.588 mm] OD and 0.01" [0.254 mm] ID) fitted on either end of the spool. A manual stage was used to keep the fiber tension constant by approximately 500  $\mu\epsilon$  during its installation. The PEEK sleeve was compressed into Swagelok fittings using 1/16" (1.588 mm) stainless ferrules (Swagelok). After this, the fiber was epoxied to the PEEK sleeve to ensure constant fiber tension. When the epoxy was fully cured, the manual stage was released and the spool was inserted into the test chamber (see Fig. 2(a)).

The chamber was partially submerged in a water bath (2837, Thermo Scientific) at  $25 \pm 0.1$  °C to minimize temperature

fluctuations. Temperature was monitored in the center of the chamber with a high pressure RTD (RTD-NPT-72-E, Omega) providing a resolution of  $\pm 0.1$  °C. The water bath was also used in experiments to characterize the temperature response of the LPGs. This characterization was performed by monitoring the LPGs while increasing the temperature in the chamber from 25 to 35 °C.

Pressure was monitored with a pressure transducer (PX309-2KG5V, Omega) with a resolution of 5 lbf/in<sup>2</sup>. The LPG signals were acquired by an optical interrogator (sm 125, Micron Optics, USA). LPGs are monitored in transmission; therefore, this unit was connected to each LPG by an optical circulator (6015-3-APC, Thorlabs) which provides light to one end of the fiber and receives the light from the other end.

The test chamber was filled with deionized water and pressurized to 1400 lbf/in<sup>2</sup> using pump 2. Data was acquired for a duration of one hour to establish a baseline. During this time, valves 2 and 3 were open to provide constant pressure in the chamber via the He cylinder. Before injection, CO<sub>2</sub> was drawn into pump 1 and was pressurized to 1400 lbf/in<sup>2</sup>. During this process, valve 3 was closed. During CO<sub>2</sub> injection, valve 1 and valve 2 were open. CO<sub>2</sub> was injected by performing full revolutions of pump 1 whereas pump 2 was used to keep the pressure constant by rotating the same amount in the opposite direction. The amount of CO<sub>2</sub> introduced in the test chamber can be calculated by the number of revolutions of pump 1. A total of 70 full revolutions of pump 1 were performed, corresponding to 40 g of CO<sub>2</sub>, to ensure saturation of water with CO<sub>2</sub>. The mass of CO<sub>2</sub> corresponding to the saturation level is obtained from the solubility value of CO<sub>2</sub> expressed as a mole fraction. At 293 K (20 °C) and 9.87 Pa (1432 lbf/in<sup>2</sup>), the mole fraction of CO<sub>2</sub> is 0.0259 [21]. Finally, valve 1 was closed and the He cylinder was connected to the test chamber to keep pressure constant as CO<sub>2</sub> dissolved in the water. The dissolution of CO<sub>2</sub> in water was monitored by the LPG sensors during 24 hours. A magnetic stirrer (50088142, Thermo Scientific Cimerac) was used during the full experiment to agitate the fluid and promote the dissolution of CO<sub>2</sub>.

### III. RESULTS

#### A. Measurement of Coating Thickness

Fig. 3 shows the mean and standard deviation of the coating thickness corresponding to 9% polystyrene solution (see measurement of coating thickness description in Section II-B).

On the X-axis, the numbers 1, 2, 3, represent the fiber samples. The letters A, B, C, represent the fiber sections at 7, 5 and 3 cm, respectively. Fig. 3 shows that the values of  $\sigma_{\text{section}}$  differ between measured sections (i.e., between  $\pm 4.4$  nm to  $\pm 22.9$  nm). The same figure also shows that  $D_{\text{section}}$  along the fiber length (A-B-C) has different values without a visible trend. Similar results were obtained for each of the seven polystyrene solution concentrations.

Fig. 4 shows the mean values for each concentration of polystyrene solution with its standard deviation. The minimum and maximum standard deviations are  $\pm 10$  and  $\pm 29$  nm, respectively.

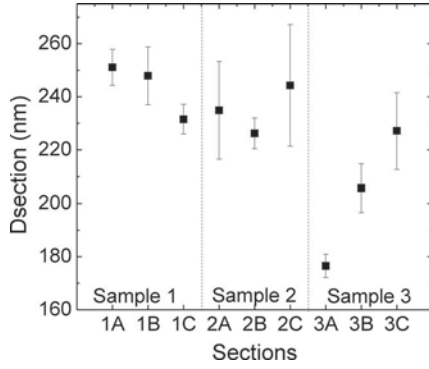


Fig. 3. Experimental value of SEM measurements for the 9.0% polystyrene solution.

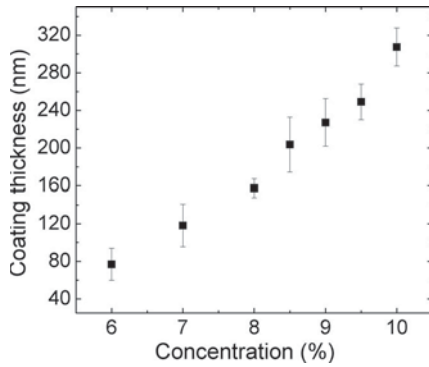


Fig. 4. Mean values of the coating thickness obtained by different concentrations of the polystyrene solutions.

TABLE I  
COATING INFORMATION FOR THE FIVE LPGS USED TO INVESTIGATE THE TRANSITION MODES

| LPG label | Polystyrene solution (%) | Coating thickness (nm) |
|-----------|--------------------------|------------------------|
| LPG1      | 8.0                      | 157.5 ± 10.0           |
| LPG2      | 8.5                      | 203.7 ± 29.1           |
| LPG3      | 9.0                      | 227.2 ± 25.3           |
| LPG4      | 9.5                      | 249.1 ± 19.0           |
| LPG5      | 10.0                     | 307.5 ± 20.2           |

### B. Investigation of Transition Modes With Coated LPGs

The phenomenon of transition modes was investigated experimentally by coating five LPGs with different concentrations of polystyrene (see Table I). Each of the coating thickness values presented in Table I was determined as in the manner presented in Section III-A.

Fig. 5 shows the resonance wavelength of LPGs 1 to 5 when immersed in solutions with different RI (i.e., characterization curves). The resonance wavelengths of the attenuation bands associated with the linear polarized modes LP<sub>04</sub> and LP<sub>05</sub> are represented by the open symbols and solid symbols, respectively. For each LPG, as the SRI increases, it can be observed that the wavelength of mode LP<sub>05</sub> decreases until it reaches the original wavelength of LP<sub>04</sub> (i.e., wavelength of LP<sub>04</sub> at SRI = 1). This phenomenon is referred to as transition modes

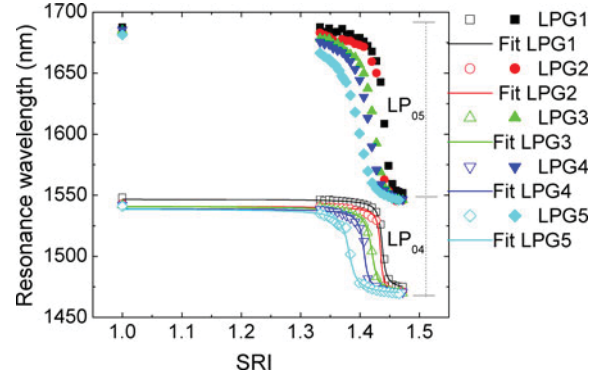


Fig. 5. Experimental characterization of modes LP<sub>04</sub> and LP<sub>05</sub> for LPGs 1–5.

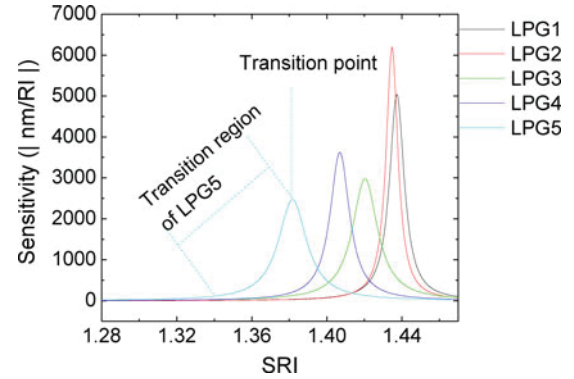


Fig. 6. Sensitivity curves for mode LP<sub>04</sub> of LPGs 1–5.

and is due to the coupling of a lower order cladding mode (i.e., LP<sub>03</sub>) to the coating [22]. This causes a reorganization of the cladding modes in which higher order cladding modes than that guided by the coating shift their resonance wavelength towards the immediate lower order cladding mode.

The cumulative Lorentz equation (see [23], eq. (1)) is the fit to experimental data and is presented in Fig. 5. For each mode,  $\lambda_{\text{on\_offset}}$  is the offset wavelength,  $S_{\text{on\_max}}$  is the maximum sensitivity,  $\Delta\text{SRI}_{3\text{dB\_on}}$  is the sensitivity bandwidth and  $\text{SRI}_{\text{tr\_on}}$  corresponds to the transition point. Cumulative Lorentz fits were only applied to the experimental points of mode LP<sub>04</sub> because its wavelength is within the spectral range of the optical interrogator used for CO<sub>2</sub> experiments.

$$\lambda(\text{SRI}) = \lambda_{\text{on\_offset}} + \frac{S_{\text{on\_max}} \Delta\text{SRI}_{3\text{dB\_on}}}{2} \times \left[ \arctan \left( 2 \frac{\text{SRI}_{\text{tr\_on}} - \text{SRI}}{\Delta\text{SRI}_{3\text{dB\_on}}} \right) + \frac{\pi}{2} \right]. \quad (1)$$

Fig. 6 shows the sensitivity curves for the LPGs, which are obtained from the absolute values of the first derivative of the cumulative Lorentz fit shown in Fig. 5. It can be observed in Fig. 6 that the transition point of each grating occurs at progressively lower SRI as a thicker coating is considered. This is a key aspect of the transition mode phenomenon which has been explored by a number of authors [17], [18], [23], [24]. When a coating material of higher RI than that of the fiber is applied in

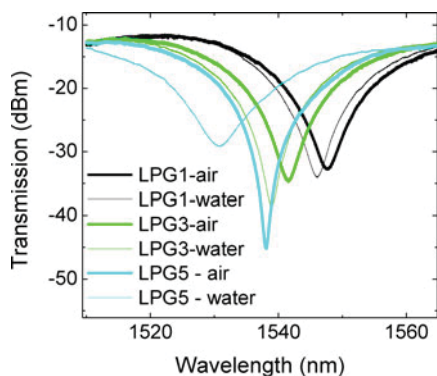


Fig. 7. Transmission spectrum of LPG1, LPG3 and LPG5 in air (thicker line) and water (thinner line).

the region of the LPG, the effective RI of the cladding modes increases. As a consequence, the resonance wavelengths of the attenuation bands decrease (see Fig. 5). As more material is deposited, there is a threshold thickness beyond which the coating is able to guide a lower order cladding mode causing the reorganization of the cladding modes [17]. The threshold thickness is a function of SRI and RI of the coating. Higher coating RIs and/or SRIs decrease the thickness required to promote the cladding mode reorganization.

Transition mode behavior can also be described in terms of the response of the resonance wavelength of the LPG to SRI, for given values of coating RI and thickness. As the SRI increases, there is an SRI value at which transition occurs, causing reorganization of the cladding modes. The SRI value at transition decreases as the thickness and/or the RI of the coating increases.

In previous work, it was observed that the depth of the attenuation band of a coated LPG at the transition decreases significantly [20]. This phenomenon was originally reported by Rees *et al.* [16] and a more detailed description was reported by Villar *et al.* [22], [24]. The RI of polymer materials has an imaginary component which describes the attenuation of electromagnetic waves in the material due to absorption of light. The imaginary component of the RI can cause the light absorbance by the coating, decreasing the depth of the attenuation bands at the transition region [24]. The challenge with coated LPGs is to establish the coating thickness that gives the maximum sensitivity to the grating at a target SRI while the depth of the attenuation band is readily detectable.

Fig. 7 shows the transmission spectrum of LPG1, LPG3, and LPG5 in air and immersed in water. For clarity, the spectra of LPG2 and LPG4 are not depicted in Fig. 7. This Figure shows that the depth of the attenuation bands of LPG1 and LPG3 increase between air (i.e., SRI = 1) and water (i.e., SRI = 1.333). This behavior was also observed for LPG2 and LPG4. However, Fig. 7 also shows that the depth of the attenuation band of LPG5 decreases by 16 dB between air and water which is consistent with transition behaviour observed by other researchers [24]. Therefore, we conclude that LPG5 is operating at the transition region at the SRI of water, whereas the transition region of LPGs 1 to 4 initiates at higher SRI than that of water.

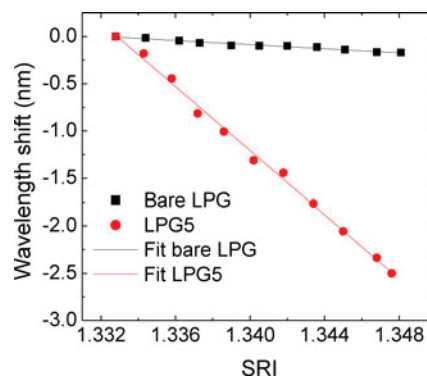


Fig. 8. Experimental characterization of bare LPG and LPG5.

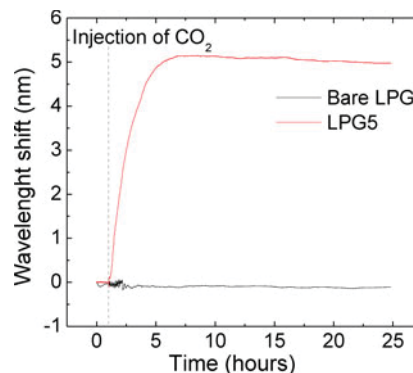


Fig. 9. Monitoring CO<sub>2</sub> injection at 1400 lbf/in<sup>2</sup> and 25 °C with LPGs.

Data for LPGs coated with 10.4% and 10.6% polystyrene solutions were not included in this article because the attenuation band of these LPGs vanished when the gratings were immersed in water. This means that the transition points of these LPGs occur between air and water and, therefore, the gratings are not suitable to operate in aqueous environments. Note that concentrations of polystyrene solutions between 10.0–10.4% could potentially result in coating thicknesses that would further improve the SRI sensitivity of the LPGs while retaining a detectable attenuation band at the SRI of water. Further investigation is needed to assess the response of LPGs coated with this concentration range of polystyrene solutions.

Fig. 8 shows the SRI characterization of an uncoated LPG (i.e., bare LPG) and LPG5. Data presented in Fig. 8 was acquired by the optical interrogator. A narrow range of SRI was selected (i.e., between 1.333 and 1.348) to calculate the sensitivity of the sensors in the vicinity of the RI of water. The sensitivity of the bare LPG and LPG5 are 10.9 and 169.1 nm/SRI, respectively. The coefficients of determination for these linear regressions are 0.965 and 0.996, respectively.

### C. Monitoring Carbon Dioxide Dissolution in Water at High Pressure

Fig. 9 shows the response of the bare LPG and LPG5 with injection of 40 g of CO<sub>2</sub> into 500 ml of water. The vertical dashed line corresponds to the injection time (see injection description in Section II-D). Prior to injection, the wavelength of both LPGs

remains virtually constant, with standard deviations of 25 and 6 pm for the bare LPG and LPG5, respectively. After injection, the wavelength of the bare LPG remains constant whereas the wavelength of LPG5 increases. From  $t = 1$  h to  $t = 8$  h, the wavelength of LPG5 (red line in Fig. 9) increases by 5.144 nm. After this, the wavelength of LPG5 levels off with a standard deviation of 53 pm between  $t = 8$  h and  $t = 24$  h.

The temperature variation in the test chamber measured by the RTD (schematic of the setup is shown in Fig. 1) was 0.5 °C. The temperature sensitivities of the bare LPG and LPG5 are 37 and 40 pm/°C, respectively. Therefore, the maximum wavelength shifts due to temperature variation for the bare LPG and LPG5 are 18.5 and 20 pm, respectively.

The maximum pressure variation in the test chamber measured by a pressure transducer (see test chamber setup in Fig. 1) is 33 lbf/in<sup>2</sup>. The pressure sensitivity of the LPGs used in this work is 0.3 pm/lbf/in<sup>2</sup>. The wavelength shift due to the pressure variation is, therefore, only 10 pm for both LPGs.

The RI of water after dissolution of CO<sub>2</sub> is a function of temperature, pressure and CO<sub>2</sub> concentration. The Abbe refractometer cannot be used in this experiment to measure RIs because a sample cannot be taken from the test chamber at high pressure conditions. Therefore, the Lorentz–Lorenz equation [25] was used to predict the RI of the water/CO<sub>2</sub> mixture by the following expression:

$$\frac{n_{12}^2 - 1}{n_{12}^2 + 2} = \phi_1 \left( \frac{n_1^2 - 1}{n_1^2 + 2} \right) + \phi_2 \left( \frac{n_2^2 - 1}{n_2^2 + 2} \right). \quad (2)$$

where  $n_{12}$  is the RI of the water/CO<sub>2</sub> mixture,  $\phi_i = w_i \rho_{12} / \rho_i$ ,  $w_i = m_i / (m_1 + m_2)$ , and  $i = 1, 2$  for water and CO<sub>2</sub>, respectively. The densities of pure water and pure CO<sub>2</sub> at 1400 lbf/in<sup>2</sup> and 25 °C are 1.0013 and 0.81180 g/ml, respectively [26]. The RI of pure water and pure CO<sub>2</sub> under this temperature and pressure conditions are 1.335 and 1.18, respectively [27], [28].

The RI of the CO<sub>2</sub> saturated water (at 1400 lbf/in<sup>2</sup> and 25 °C) is 1.3205, based on the Lorentz–Lorenz Law. Using this value and the SRI sensitivity of LPG5 presented in Fig. 8 (i.e., 169.1 nm/SRI), the theoretical wavelength shift of LPG5 between water and CO<sub>2</sub> saturated water is 2.5 nm. The experimental wavelength shift observed in Fig. 9 (i.e., 5.144 nm) is approximately twice this theoretical value. This result suggests that the wavelength shift of LPG5 in the CO<sub>2</sub> experiment presented in Fig. 9 is due not only to the change in SRI but also to a change in the RI of the polystyrene coating due to sorption of CO<sub>2</sub> at high pressure. Note that the SRI sensitivity was calculated by immersing LPG5 in glycerin solutions at ambient pressure and evidence of sorption of glycerin into polystyrene under testing conditions was not found in the literature.

Sorption of CO<sub>2</sub> at high pressure into various polymers including polystyrene has been investigated in a number of studies [29], [30]. This is a reversible mechanism in which CO<sub>2</sub> diffuses into the polymer matrix and causes both swelling and a change in the RI of the polymer [30]. Swelling of polystyrene caused by sorption of CO<sub>2</sub> has been measured [29], [30] but measurements of the associated RI change have not been reported. For the case of chloroform diffusing into polystyrene, RI change has been calculated using the Lorentz–Lorenz Law [31]. Based

on this approach, sorption of CO<sub>2</sub> (RI of 1.18 at 1400 lbf/in<sup>2</sup> and 25 °C) into polystyrene (RI of 1.59 as specified by the supplier, Sigma-Aldrich, USA) is expected to decrease the RI of the polystyrene coating. The resonance wavelength of a coated LPG increases as the RI of the coating decreases. Additionally, the SRI decreases as CO<sub>2</sub> dissolves in water (see Equation (2)), which leads to the increase of the resonance wavelength of a coated LPG. The combination of the two effects, SRI and RI change of the coating due to presence of CO<sub>2</sub> at high pressure, is expected to lead to the enhanced experimental wavelength shift observed in Fig. 9.

The resolution of LPG5 as a high pressure CO<sub>2</sub> sensor is calculated based on sensitivity determined from the wavelength shift between water and CO<sub>2</sub> saturated water (Fig. 9). For this calculation, the wavelength response of LPG5 to intermediate concentrations is assumed to vary linear. A linear regression is calculated between 0 ppm (i.e., pure water) and  $7.820 \times 10^4$  ppm (i.e., CO<sub>2</sub> saturated water) using the experimental wavelength shift between these two values (i.e., 5.144 nm). The slope of this linear regression is  $6.578 \times 10^{-5}$  nm/ppm. The wavelength resolution provided by the Micron Optics interrogator is 1 pm. Therefore, the resolution for the CO<sub>2</sub> sensor, based on the results of LPG5, is estimated to be 15 ppm. The mini-pro CO<sub>2</sub> (Pro Oceanus, Canada) is a commercial CO<sub>2</sub> sensor that uses infrared light to measure the partial pressure of CO<sub>2</sub>. This sensor has a resolution of 10 ppm between 0–5000 ppm. Although the sensor proposed in this work shows lower resolution, the operating range is wider than the specifications provided by this commercial sensor. Further tests are required to evaluate the performance of the coated LPGs under difference concentration ranges of CO<sub>2</sub> and to assess linearity.

The results of this section confirm that a coated LPG is suitable to monitor dissolution of CO<sub>2</sub> in water at carbon sequestration pressure present in saline aquifers. The sensing principle is based on the combination of SRI and sorption of CO<sub>2</sub> by the polystyrene coating. For downhole applications, the LPG sensor will require mounting in a protective enclosure which allows fluid access to the LPG.

#### IV. CONCLUSION

This work presents an experimental investigation of LPG transition modes. A relationship is established between the thickness of a polystyrene coating on an optical fiber that is applied using the dip-coating technique and the concentration of polystyrene/chloroform solution used in the coating process. A scanning electron microscope was used to measure the coating thickness. Transition modes were investigated with the objective to increase the sensitivity of LPGs for values of SRI in the vicinity of the RI of water. A sensitivity of 169.1 nm/SRI was obtained for coated LPG with a coating thickness of  $307.5 \pm 20.2$  nm. Finally, this LPG was used to monitor dissolution of CO<sub>2</sub> in water at carbon sequestration conditions. A wavelength shift of 5.144 nm was obtained for the coated LPG whereas the bare LPG had no measureable shift. The wavelength shift of the coated LPG is believed to be caused by both the SRI change and the sorption of CO<sub>2</sub> by the polystyrene which changes the RI of the coating.

## REFERENCES

- [1] IPCC Special Report on Carbon Capture and Storage, Prepared by Working Group III of the Intergovernmental Panel on Climate Change. Cambridge, U.K.: Cambridge Univ. Press, 2005.
- [2] K. Pruess, "On CO<sub>2</sub> fluid flow and heat transfer behavior in the subsurface, following leakage from a geologic storage reservoir," *Environ. Geol.*, vol. 54, no. 8, pp. 1677–1686, Jul. 2007.
- [3] R. A. Chadwick, R. Arts, M. Bentham, O. Eiken, S. Holloway, G. A. Kirby, J. M. Pearce, J. P. Williamson, and P. Zweigel, "Review of monitoring issues and technologies associated with the long-term underground storage of carbon dioxide," *Geol. Soc. London, Spec. Publ.*, vol. 313, pp. 257–275, 2009.
- [4] DOE/NETL, Best practices for monitoring, verification, and accounting of CO<sub>2</sub> stored in deep geologic formations—2012 Update, 2012.
- [5] X. Jiang, W. A. A. Hassan, and J. Gluyas, "Modelling and monitoring of geological carbon storage: A perspective on cross-validation," *Appl. Energy*, vol. 112, pp. 784–792, Dec. 2013.
- [6] H. Segawa, E. Ohnishi, Y. Arai, and K. Yoshida, "Sensitivity of fiber-optic carbon dioxide sensors utilizing indicator dye," *Sens. Actuators B Chem.*, vol. 94, no. 3, pp. 276–281, Oct. 2003.
- [7] C. S. Chu and Y. L. Lo, "Highly sensitive and linear optical fiber carbon dioxide sensor based on sol-gel matrix doped with silica particles and HPTS," *Sens. Actuators B Chem.*, vol. 143, no. 1, pp. 205–210, Dec. 2009.
- [8] B. Soukup, K. S. Repasky, J. L. Carlsten, and G. Wicks, "Field demonstration of a 1×4 fiber sensor array for subsurface carbon dioxide monitoring for carbon sequestration," *J. Appl. Remote Sens.*, vol. 8, pp. 1–12, Jan. 2009.
- [9] J. A. Nwaboh, J. Hald, J. K. Lyngso, J. C. Petersen, and O. Werhahn, "Measurements of CO<sub>2</sub> in a multipass cell and in a hollow-core photonic bandgap fiber at 2 μm," *Appl. Phys. B*, vol. 110, no. 2, pp. 187–194, May 2012.
- [10] S. Pevec and D. Donlagic, "Nanowire-based refractive index sensor on the tip of an optical fiber," *Appl. Phys. Lett.*, vol. 102, no. 21, pp. 213114-1–213114-4, May 2013.
- [11] B. N. Shivananju, S. Yamdagni, R. Fazuldeen, A. K. S. Kumar, G. M. Hegde, M. M. Varma, and S. Asokan, "CO<sub>2</sub> sensing at room temperature using carbon nanotubes coated core fiber Bragg grating," *Rev. Sci. Instrum.*, vol. 84, no. 6, pp. 065002-1–065002-7, Jun. 2013.
- [12] L. Melo, G. Burton, B. Davies, D. Risk, and P. Wild, "Highly sensitive coated long period grating sensor for CO<sub>2</sub> detection at atmospheric pressure," *Sens. Actuators B Chem.*, vol. 202, pp. 294–300, Oct. 2014.
- [13] M. V. Avdeev, A. N. Kononov, V. N. Bagratashvili, V. K. Popov, S. I. Tsygina, M. Sokolova, J. Ke, and M. Poliakov, "The fibre optic reflectometer: A new and simple probe for refractive index and phase separation measurements in gases, liquids and supercritical fluids," *Phys. Chem. Chem. Phys.*, vol. 6, no. 6, pp. 1258–1263, Feb. 2004.
- [14] B. Bao, L. Melo, B. Davies, H. Fadaei, D. Sinton, and P. Wild, "Detecting supercritical CO<sub>2</sub> in brine at sequestration pressure with an optical fiber sensor," *Environ. Sci. Technol.*, vol. 47, no. 1, pp. 306–313, Jan. 2013.
- [15] S. W. James and R. P. Tatam, "Optical fibre long-period grating sensors: Characteristics and application," *Meas. Sci. Technol.*, vol. 49, no. 5, pp. R49–R61, Mar. 2003.
- [16] N. D. Rees, S. W. James, R. P. Tatam, and G. J. Ashwell, "Optical fiber long-period gratings with Langmuir-Blodgett thin-film overlays," *Opt. Lett.*, vol. 27, no. 9, pp. 686–688, May 2002.
- [17] I. Del Villar, I. Matias, F. Arregui, and P. Lalanne, "Optimization of sensitivity in long period fiber gratings with overlay deposition," *Opt. Exp.*, vol. 13, no. 1, pp. 56–69, Jan. 2005.
- [18] A. Cusano, A. Iadicicco, P. Pilla, L. Contessa, S. Campopiano, A. Cutolo, and M. Giordano, "Mode transition in high refractive index coated long period gratings," *Opt. Exp.*, vol. 14, no. 1, pp. 19–34, Jan. 2006.
- [19] P. Pilla, C. Trono, F. Baldini, F. Chiavaioli, M. Giordano, and A. Cusano, "Giant sensitivity of long period gratings in transition mode near the dispersion turning point: An integrated design approach," *Opt. Lett.*, vol. 37, no. 19, pp. 4152–4154, Oct. 2012.
- [20] L. Melo, G. Burton, S. Warwick, and P. Wild, "Experimental investigation of long period grating working in transition mode," *Proc. SPIE*, vol. 9157, pp. 1–4, Jun. 2014.
- [21] H. Teng and A. Yamasaki, "Solubility of liquid CO<sub>2</sub> in water at temperatures from 278 K to 293 K and pressures from 6.44 MPa to 29.49 MPa and densities of the corresponding aqueous solutions," *J. Chem. Thermodyn.*, vol. 29, no. 11, pp. 1301–1310, Nov. 1997.
- [22] I. del Villar, I. R. Matias, S. Member, F. J. Arregui, and M. Achaerandio, "Nanodeposition of materials with complex refractive index in long-period fiber gratings," *J. Lightw. Technol.*, vol. 23, no. 12, pp. 4192–4199, Dec. 2005.
- [23] A. Cusano, A. Iadicicco, P. Pilla, A. Cutolo, M. Giordano, and S. Campopiano, "Sensitivity characteristics in nanosized coated long period gratings," *Appl. Phys. Lett.*, vol. 89, no. 20, pp. 201116-1–201116-3, Nov. 2006.
- [24] I. Del Villar, M. Achaerandio, I. R. Matias, and F. J. Arregui, "Deposition of overlays by electrostatic self-assembly in long-period fiber gratings," *Opt. Lett.*, vol. 30, no. 7, pp. 720–722, Apr. 2005.
- [25] A. Z. Tasic, B. Djordjevic, D. K. Grozdanic, and N. Radojkovic, "Use of mixing rules in predicting refractive indices and specific refractivities for some binary liquid mixtures," *J. Chem. Eng. Data*, vol. 37, no. 3, pp. 310–313, 1992.
- [26] NIST Chemistry WebBook. (2014, Dec. 29). [Online]. Available: <http://webbook.nist.gov/chemistry/fluid/>.
- [27] Y. Sun, B. Y. Shekunov, and P. York, "Refractive index of supercritical CO<sub>2</sub> - ethanol solvents," *Chem. Eng. Commun.*, vol. 190, no. 1, pp. 1–14, Jan. 2003.
- [28] Y. Song, M. Nishio, B. Chen, S. Someya, and T. Ohsumi, "Measurement on CO<sub>2</sub> solution density by optical technology," *J. Vis.*, vol. 6, no. 1, pp. 41–51, 2003.
- [29] Y. Sato, T. Takikawa, S. Takishima, and H. Masuoka, "Solubilities and diffusion coefficients of carbon dioxide in poly (vinyl acetate) and polystyrene," *J. Supercrit. Fluids*, vol. 19, pp. 187–198, 2001.
- [30] S. Hilic, S. Boyer, A. Padua, and J. Grolier, "Simultaneous measurement of the solubility of nitrogen and carbon dioxide in polystyrene and of the associated polymer swelling," *J. Polym. Sci.*, vol. 39, no. 17, pp. 2063–2070, Sep. 2001.
- [31] M. Giordano, M. Russo, A. Cusano, and G. Mensitieri, "An high sensitivity optical sensor for chloroform vapours detection based on nanometric film of δ-form syndiotactic polystyrene," *Sens. Actuators B Chem.*, vol. 107, no. 1, pp. 140–147, May 2005.

**Luis Melo** received the M.Sc. degree in physics engineering from the University of Aveiro, Aveiro, Portugal in 2010. He is currently working toward the Ph.D. degree in mechanical engineering with the University of Victoria, Victoria, BC, Canada, conducting the research in fiber optic sensors for detection of CO<sub>2</sub>. His research interests include optoelectronic sensors for the detection of chemical species and materials characterization by scanning electron microscopy.

**Geoff Burton** received the bachelor's degree in mechanical engineering from the University of Victoria, Victoria, BC, Canada, in 2012. Since 2012, he has been working as a Research Engineer with the Institute for Integrated Energy Systems, University of Victoria. His research interest includes fiber optic sensor design for the detection of chemical species.

**Stephen Warwick** received the bachelor's degree in mechanical engineering from the University of Victoria, Victoria, BC, Canada, in 2012. Since 2012, he has been working as a Research Engineer with the Institute for Integrated Energy Systems and the Centre for Aerospace Research, University of Victoria. His research interests include instrumentation and control with a focus in fiber optic sensors.

**Peter M. Wild** is currently a Professor with the Department of Mechanical Engineering, University of Victoria (UVic), Victoria, BC, USA. He is the Chair of the Natural Sciences and Engineering Research Council in Sustainable Energy Systems Design and is the Director of the Institute for Integrated Energy Systems, (IESVic), University of Victoria. His research interests include optical sensors for industrial, environmental, and biomedical applications; impacts of integration of renewable energy generation into existing grids; and renewable energy generation technologies.

**Appendix C: Long period gratings coated with hafnium oxide by plasma-enhanced atomic layer deposition for refractive index measurements**

L. Melo, G. Burton, P. Kubik, and P. Wild, "Long period gratings coated with hafnium oxide by plasma-enhanced atomic layer deposition for refractive index measurements," Opt. Express, vol. 24, no. 7, p. 7654, 2016.

Reprinted, with permission, from Optics Express, The Optical Society (OSA)

# Long period gratings coated with hafnium oxide by plasma-enhanced atomic layer deposition for refractive index measurements

Luis Melo,<sup>1,\*</sup> Geoff Burton,<sup>1</sup> Philip Kubik,<sup>2</sup> and Peter Wild<sup>1</sup>

<sup>1</sup>Department of Mechanical Engineering, University of Victoria, P.O. Box 3055, Victoria, B.C., V8W 3P6, Canada

<sup>2</sup>4D Labs, Simon Fraser University, 8888 University Drive, Burnaby, B.C., V5A 1S6, Canada

\*luismelo@uvic.ca

**Abstract:** Long period gratings (LPGs) are coated with hafnium oxide using plasma-enhanced atomic layer deposition (PEALD) to increase the sensitivity of these devices to the refractive index of the surrounding medium. PEALD allows deposition at low temperatures which reduces thermal degradation of UV-written LPGs. Depositions targeting three different coating thicknesses are investigated: 30 nm, 50 nm and 70 nm. Coating thickness measurements taken by scanning electron microscopy of the optical fibers confirm deposition of uniform coatings. The performance of the coated LPGs shows that deposition of hafnium oxide on LPGs induces two-step transition behavior of the cladding modes.

©2016 Optical Society of America

**OCIS codes:** (310.0310) Thin films; (060.2370) Fiber optics sensors; (350.2770) Gratings.

---

## References and links

1. C. Caucheteur, T. Guo, and J. Albert, "Review of plasmonic fiber optic biochemical sensors: improving the limit of detection," *Anal. Bioanal. Chem.* **407**(14), 3883–3897 (2015).
2. X. D. Wang and O. S. Wolfbeis, "Fiber-Optic Chemical Sensors and Biosensors (2008-2012)," *Anal. Chem.* **85**(2), 487–508 (2013).
3. L. Melo, G. Burton, S. Warwick, and P. M. Wild, "Experimental Investigation of Long-Period Grating Transition Modes to Monitor CO<sub>2</sub> in High-Pressure Aqueous Solutions," *J. Lightwave Technol.* **33**(12), 2554–2560 (2015).
4. S. W. James and R. P. Tatam, "Optical fibre long-period grating sensors: characteristics and application," *Meas. Sci. Technol.* **14**(5), R49–R61 (2003).
5. P. Biswas, N. Basumallick, S. Bandyopadhyay, K. Dasgupta, A. Ghosh, and S. Bandyopadhyay, "Sensitivity Enhancement of Turn-Around-Point Long Period Gratings By Tuning Initial Coupling Condition," *IEEE Sens. J.* **15**(2), 1240–1245 (2015).
6. A. Martinez-Rios, D. Monzon-Hernandez, and I. Torres-Gomez, "Highly sensitive cladding-etched arc-induced long-period fiber gratings for refractive index sensing," *Opt. Commun.* **283**(6), 958–962 (2010).
7. N. D. Rees, S. W. James, R. P. Tatam, and G. J. Ashwell, "Optical fiber long-period gratings with Langmuir-Blodgett thin-film overlays," *Opt. Lett.* **27**(9), 686–688 (2002).
8. A. Cusano, A. Iadicicco, P. Pilla, L. Contessa, S. Campopiano, A. Cutolo, and M. Giordano, "Mode transition in high refractive index coated long period gratings," *Opt. Express* **14**(1), 19–34 (2006).
9. I. Del Villar, I. Matías, F. Arregui, and P. Lalanne, "Optimization of sensitivity in Long Period Fiber Gratings with overlay deposition," *Opt. Express* **13**(1), 56–69 (2005).
10. I. Del Villar, M. Achaerandio, I. R. Matías, and F. J. Arregui, "Deposition of overlays by electrostatic self-assembly in long-period fiber gratings," *Opt. Lett.* **30**(7), 720–722 (2005).
11. S. Korposh, S. W. Lee, S. W. James, and R. P. Tatam, "Refractive index sensitivity of fibre-optic long period gratings coated with SiO<sub>2</sub> nanoparticle mesoporous thin films," *Meas. Sci. Technol.* **22**(7), 075208 (2011).
12. L. Melo, G. Burton, B. Davies, D. Risk, and P. Wild, "Highly sensitive coated long period grating sensor for CO<sub>2</sub> detection at atmospheric pressure," *Sens. Actuators B Chem.* **202**, 294–300 (2014).
13. M. Smietana, W. J. Bock, and P. Mikulic, "Temperature sensitivity of silicon nitride nanocoated long-period gratings working in various surrounding media," *Meas. Sci. Technol.* **22**(11), 115203 (2011).
14. M. Smietana, M. L. Korwin-Pawlowski, W. J. Bock, G. R. Pickrell, and J. Szmids, "Refractive index sensing of fiber optic long-period grating structures coated with a plasma deposited diamond-like carbon thin film," *Meas. Sci. Technol.* **19**(8), 085301 (2008).
15. L. Coelho, D. Viegas, J. Santos, and J. Almeida, "Enhanced refractive index sensing characteristics of optical fibre long period grating coated with titanium dioxide thin films," *Sens. Actuators B Chem.* **202**, 929–934

- (2014).
16. M. Śmietana, M. Koba, P. Mikulic, R. Bogdanowicz, and W. J. Bock, "Improved diamond-like carbon coating deposition uniformity on cylindrical sample by its suspension in RF PECVD chamber," *Phys. Status Solidi* **212**(11), 2496–2500 (2015).
  17. M. Śmietana, M. Koba, E. Brzozowska, K. Krogulski, J. Nakonieczny, L. Wachnicki, P. Mikulic, M. Godlewski, and W. J. Bock, "Label-free sensitivity of long-period gratings enhanced by atomic layer deposited TiO<sub>2</sub> nano-overlays," *Opt. Express* **23**(7), 8441–8453 (2015).
  18. M. Śmietana, W. J. Bock, and P. Mikulic, "Effect of high-temperature plasma-deposited nano-overlays on the properties of long-period gratings written with UV and electric arc in non-hydrogenated fibers," *Meas. Sci. Technol.* **24**(9), 094016 (2013).
  19. S. M. George, "Atomic layer deposition: an overview," *Chem. Rev.* **110**(1), 111–131 (2010).
  20. H. Kim, H. Lee, and W. Maeng, "Applications of atomic layer deposition to nanofabrication and emerging nanodevices," *Thin Solid Films* **517**(8), 2563–2580 (2009).
  21. J. W. Elam, M. D. Groner, and S. M. George, "Viscous flow reactor with quartz crystal microbalance for thin film growth by atomic layer deposition," *Rev. Sci. Instrum.* **73**(8), 2981–2987 (2002).
  22. O. Sneh, R. B. Clark-Phelps, A. R. Londergan, J. Winkler, and T. E. Seidel, "Thin film atomic layer deposition equipment for semiconductor processing," *Thin Solid Films* **402**(1–2), 248–261 (2002).
  23. M. D. Groner, F. H. Fabreguette, J. W. Elam, and S. M. George, "Low-Temperature Al<sub>2</sub>O<sub>3</sub> Atomic Layer Deposition," *Chem. Mater.* **16**(4), 639–645 (2004).
  24. H. Profijt, S. Potts, M. Van de Sanden, and W. Kessels, "Plasma-Assisted Atomic Layer Deposition: Basics, Opportunities, and Challenges," *J. Vac. Sci. Technol. A* **29**(5), 050801 (2011).
  25. E. M. Dianov, V. I. Karpov, A. S. Kurkov, and M. V. Grekov, "Long-period fiber gratings and mode-field converters fabricated by thermodiffusion in phosphosilicate fibers," In *Proceedings of the IEEE 24th European Conference on Optical Communication, Madrid, Spain, 20–24 September 1998*; pp. 395–396.
  26. M. Śmietana, M. Myśliwiec, P. Mikulic, B. S. Witkowski, and W. J. Bock, "Capability for fine tuning of the refractive index sensing properties of long-period gratings by atomic layer deposited Al<sub>2</sub>O<sub>3</sub> overlays," *Sensors (Basel Switzerland)* **13**(12), 16372–16383 (2013).
  27. F. Zou, Y. Liu, C. Deng, Y. Dong, S. Zhu, and T. Wang, "Refractive index sensitivity of nano-film coated long-period fiber gratings," *Opt. Express* **23**(2), 1114–1124 (2015).
  28. G. Rego, O. Okhotnikov, E. Dianov, and V. Sulimov, "High-temperature stability of long-period fiber gratings produced using an electric arc," *J. Lightwave Technol.* **19**(10), 1574–1579 (2001).
  29. Y. Widjaja and C. B. Musgrave, "Atomic layer deposition of hafnium oxide: A detailed reaction mechanism from first principles," *J. Chem. Phys.* **117**(5), 1931–1934 (2002).
  30. C. R. Zamarrano, I. R. Matias, and F. J. Arregui, "Nanofabrication Techniques Applied to the Development of Novel Optical Fiber Sensors Based on Nanostructured Coatings," *IEEE Sens. J.* **12**(8), 2699–2710 (2012).
  31. I. Del Villar, I. R. Matias, and F. J. Arregui, "Influence on cladding mode distribution of overlay deposition on long-period fiber gratings," *J. Opt. Soc. Am. A* **23**(3), 651–658 (2006).
  32. L. Melo, G. Burton, P. Wild, Dep. Mech. Eng. Univ. Victoria, P.O. Box 3055, Victoria, B.C., Canada V8W 3P6, and P. Kubik, 4D Labs, Simon Fraser Univ. 8888 Univ. Drive, Burn. B.C., Canada V5A 1S6. are preparing a manuscript to be called "Refractive index sensor based on inline Mach-Zehnder interferometer coated with hafnium oxide by atomic layer deposition,"
  33. O. Buiu, Y. Lu, I. Z. Mitrovic, S. Hall, P. Chalker, and R. J. Potter, "Spectroellipsometric assessment of HfO<sub>2</sub> thin films," *Thin Solid Films* **515**(2), 623–626 (2006).
  34. M. Śmietana, W. J. Bock, and J. Szmidi, "Evolution of optical properties with deposition time of silicon nitride and diamond-like carbon films deposited by radio-frequency plasma-enhanced chemical vapor deposition method," *Thin Solid Films* **519**(19), 6339–6343 (2011).
  35. P. Pilla, P. F. Manzillo, V. Malachovska, A. Buosciolo, S. Campopiano, A. Cutolo, L. Ambrosio, M. Giordano, and A. Cusano, "Long period grating working in transition mode as promising technological platform for label-free biosensing," *Opt. Express* **17**(22), 20039–20050 (2009).
  36. S. W. James, C. S. Cheung, and R. P. Tatam, "Experimental observations on the response of 1(st) and 2(nd) order fibre optic long period grating coupling bands to the deposition of nanostructured coatings," *Opt. Express* **15**(20), 13096–13107 (2007).
  37. T. Erdogan, "Cladding-mode resonances in short- and long- period fiber grating filters," *J. Opt. Soc. Am. A* **14**(8), 1760–1773 (1997).
  38. A. Cusano, A. Iadicicco, P. Pilla, A. Cutolo, M. Giordano, and S. Campopiano, "Sensitivity characteristics in nanosized coated long period gratings," *Appl. Phys. Lett.* **89**(20), 201116 (2006).
  39. M. A. Alam and M. L. Green, "Mathematical description of atomic layer deposition and its application to the nucleation and growth of HfO<sub>2</sub> gate dielectric layers," *J. Appl. Phys.* **94**(5), 3403–3413 (2003).
  40. P. Pilla, C. Trono, F. Baldini, F. Chiavaioli, M. Giordano, and A. Cusano, "Giant sensitivity of long period gratings in transition mode near the dispersion turning point: an integrated design approach," *Opt. Lett.* **37**(19), 4152–4154 (2012).
  41. I. Del Villar, "Ultrahigh-sensitivity sensors based on thin-film coated long period gratings with reduced diameter, in transition mode and near the dispersion turning point," *Opt. Express* **23**(7), 8389–8398 (2015).

## Introduction

Over the past two decades, fiber-optic based refractive index (RI) sensors have been widely investigated for chemical [1], biological [2] and environmental applications [3]. Long period gratings have attracted particular attention due to their intrinsic sensitivity to the RI of the surrounding medium (SRI), and the possibility of producing sensors with low insertion loss and low polarization dependence [4]. The SRI sensitivity of conventional LPGs is relatively low when the devices operate in a media with low SRI, such as water (i.e. SRI of 1.33), and increases as the SRI approaches the RI of silica (i.e. RI of 1.45) [4]. However, a number of approaches have been proposed to develop LPG sensors with high sensitivity at low SRIs. These include designing LPGs that promote coupling between the core mode and a specific cladding mode near the dispersion turning point [5], etching the fiber [6], and coating the fiber [7].

Coating an LPG with a material that has a higher RI than silica promotes a phenomenon referred to as the *transition mode* [8]. For a fixed coating thickness of a material with a given RI, there is a value of SRI at which a lower order cladding guided mode is coupled to the coating (i.e. the coating acts as a waveguide) [7–9]. As a consequence, higher order cladding modes than that guided by the coating shift their resonance wavelength towards the original wavelength of the adjacent lower order cladding mode, causing a redistribution of the cladding modes. This leads to a significant increase of the SRI sensitivity of coated LPGs, especially in the SRI range corresponding to the transition of cladding modes to the coating (i.e. transition region) [8]. For a coating material with a given RI, it is possible to tune the transition region to low SRIs by selecting an appropriate coating thickness [7–9].

Various coating techniques and materials have been investigated to promote transition modes in LPGs. Rees *et al.* coated an LPG with tricosenoic acid using the Langmuir-Blodgett technique [7]. Villar *et al.* and Korposh *et al.* used electrostatic self-assembly to deposit polymers [10] and silica nanoparticles [11], respectively, on LPGs. Although these techniques allow control of coating thickness, the coatings show weak adhesion to the optical fiber. The dip-coating technique has also been investigated to coat LPGs with polystyrene [8,12]. This method enables high RI sensitivities but with poor control of coating thickness.

Advanced coating techniques have also been investigated to promote transition mode behavior in LPGs with materials that show good adhesion to optical fibers. Radio-frequency plasma-enhanced chemical vapor deposition (RF PECVD) has been used to deposit silicon nitride [13] and diamond-like carbon coatings on LPGs [14]. Thermal evaporation has been used to deposit titanium dioxide (TiO<sub>2</sub>) on LPGs [15]. Chemical vapor deposition (CVD) and thermal evaporation are directional deposition methods and, thus, must be adapted to coat the cylindrical surface of optical fibers by rotating the fiber [15] or by suspending the fiber above the substrate Table [16]. Although, significant progress has been made to achieve uniform depositions with CVD by suspending the optical fibers above the substrate Table [16], control of coating thickness at the nanometer scale remains challenging using these directional deposition methods [17]. Additionally, it has been shown that CVD can cause thermal degradation of UV-written LPGs due to the high deposition temperatures [18].

Atomic layer deposition (ALD) has become an important technique in the semiconductor industry to deposit uniform layers of metal oxides with high dielectric constants, such as aluminum oxide (Al<sub>2</sub>O<sub>3</sub>) and hafnium oxide (HfO<sub>2</sub>), in MOSFET devices [19]. Metal oxide deposition by ALD uses two gas precursors: the *metal precursor* is the source of the reactive metal and the *oxygen precursor* is the source of oxygen. The film is grown in a cyclic process comprising injection of the metal precursor, purge of the metal precursor, injection of the oxygen precursor and purge of the oxygen precursor. Inert gases, such as argon (Ar) or nitrogen (N<sub>2</sub>), are typically used to carry the gas precursors from an external reservoir to the process chamber and to purge the process chamber between injections.

Each precursor is injected into the process chamber in a sufficient amount to ensure that the gas reaches all active sites on the substrate. The purge time is selected to ensure removal of unreacted precursors and by-products from the process chamber. If both of these conditions are met, then each gas precursor is present in the process chamber individually and undergoes gas-solid reactions solely on the surface of the substrate (*i.e.* self-limiting surface reactions). As a result, ALD is non-directional and is, therefore, well suited for deposition of conformal coatings on complex substrates [20]. The main disadvantage of ALD is its low deposition rate compared with other deposition methods such as CVD. The deposition rates of ALD are typically less than 100 nm/hr and are strongly dependent on the deposition temperature.

The deposition temperature of ALD depends on the type of process that is used to activate the gas precursors. The reactions in ALD can be thermally activated at various temperatures (*i.e.* typically 150 - 350 °C) and, therefore, this process is commonly referred to as *thermal* ALD. Process parameters such as pulse and purge times are optimized for each deposition temperature [21,22]. In thermal ALD, lower deposition temperatures require considerably longer purge times, due primarily to the slower desorption of the oxygen precursor (*e.g.* H<sub>2</sub>O) from the internal surfaces of the process chamber [23]. If purge times are not extended, incomplete purging of the oxygen precursor will occur and this will cause CVD-type reactions between the metal precursor and the residual oxygen precursor [23]. This can result in deposition of a non-uniform coating thickness [23].

ALD can also be performed with the aid of oxygen plasma following the metal precursor pulse, replacing the oxygen precursor used in the thermal process [24]. This process is referred to as *plasma-enhanced* ALD (PEALD). The plasma produces oxygen radicals that react with the metal precursor to form the metal oxide. The oxygen radicals have higher chemical reactivity than the oxygen precursors used in the thermal process. For this reason, as the deposition temperature decreases, the purge time of the oxygen precursor in thermal ALD becomes longer whereas the purge time of the oxygen in PEALD remains constant. Thus, as deposition temperature decreases, the deposition time of thermal ALD becomes longer than the deposition time of PEALD.

Deposition temperature and deposition time are important parameters when coating LPGs by ALD because, depending on the writing process, gratings can degrade at elevated temperatures and the rate of degradation increases with temperature. Thermal degradation of an LPG is manifest as a permanent decrease of the depth of the attenuation bands [18]. This decreased depth is undesirable for coated LPGs working as SRI sensors because the attenuation bands can become difficult to detect [18].

The most common process to write LPGs is by UV irradiation of hydrogen loaded germanium doped fibers. Dianov et al. showed that thermal degradation of UV-written LPGs in this type of fiber starts at temperatures between 300 °C and 400 °C [25]. The study was conducted by increasing the annealing temperature in steps of 100 °C with a waiting period of 5 minutes at each step. However, the coating of LPGs by ALD requires significantly longer exposure durations (*i.e.* hours) at temperatures between 150 - 350 °C to achieve coating thicknesses that promote transition mode behavior, assuming typical ALD deposition rates of less than 100 nm/hr. Studies of thermal degradation of UV-written LPGs in hydrogen loaded fibers at temperatures and over durations typically used in ALD are not available in the literature.

The development of ALD coating of LPGs to promote transition mode behavior is, relatively speaking, at an early stage. Śmietana *et al.* investigated the coating of LPGs, written by electric arc-discharge, with Al<sub>2</sub>O<sub>3</sub> by thermal ALD at 150 °C [26]. Zou *et al.* investigated the coating of LPGs, written by CO<sub>2</sub> laser, with Al<sub>2</sub>O<sub>3</sub> by thermal ALD at 210 °C [27]. Śmietana et al. report a sensitivity value of 1850 nm/SRI in the SRI range between 1.3330 – 1.342 [26], and Zou et al. report a sensitivity value of 1500 nm/SRI in the SRI range between 1.3622 – 1.39 [27]. In these studies, thermal degradation is not expected because gratings

written by either electric-arc discharge [28] or CO<sub>2</sub> laser [25] are stable at these ALD temperatures.

Both of Smietana and Zou provide limited coating thicknesses data based on scanning electron microscopy (SEM) measurements [26,27]. This data suggests that, as expected, thermal ALD at 210 °C results in higher coating uniformity than thermal ALD at 150 °C. However, as noted by Smietana, non-uniformity may be due to a lack of precision of the SEM measurements [26].

Smietana *et al.* also report UV-written LPGs coated with TiO<sub>2</sub> by thermal ALD at 85 °C [17]. The authors selected this low deposition temperature to avoid removing the polymer layer that protects the optical fiber. Purge times and coating thickness uniformity are not reported.

PEALD is a promising alternative method for coating UV-written LPGs. As noted above, this process is non-directional and can be performed at low temperatures, thereby avoiding degradation of UV-written LPGs, while also maintaining shorter purge times than are required in thermal ALD to achieve uniform coating thickness. In this work, the first use of PEALD to coat a UV-written LPG with a metal oxide (HfO<sub>2</sub>) film is presented. HfO<sub>2</sub> is a promising candidate for optical coatings because it has a high RI (*i.e.* approximately 2.0 at 1550 nm) and high transmission coefficient [29]. Additionally, HfO<sub>2</sub> has higher density (*i.e.* greater than 9.0 g/cm<sup>3</sup>) compared with other materials used in ALD such as Al<sub>2</sub>O<sub>3</sub> (*i.e.* between 2.5 - 3 g/cm<sup>3</sup>) and TiO<sub>2</sub> (*i.e.* between 3 - 4 g/cm<sup>3</sup>). This is important because high-density films can prevent the penetration of chemical species such as water and hydrogen into the optical fiber. The presence of these species in the optical fiber leads to the formation of hydroxyl groups which may increase optical losses. Therefore, HfO<sub>2</sub> has the potential to increase the stability of SRI sensors for long-term monitoring in harsh environments [30].

It is shown in this work that PEALD enables deposition of a uniform coating of a metal oxide on a UV-written LPG without causing significant thermal degradation of the LPG. The RI sensitivity of the coated LPG is investigated and it is shown that the high RI of the HfO<sub>2</sub> coating leads to a two-step transition of the cladding modes which is explained using hybrid mode formulation (*i.e.* HE and EH modes). The depth of the attenuation band of the EH modes increases in the SRI range corresponding to the transition region and both HE and EH modes remain readily detectable at the transition point. This finding agrees with the numerical work conducted by Villar *et al.* [31] and is important because it enables the design of LPG sensors that operate close to the transition point, where the sensitivity of coated LPGs is high.

## Methods

This work is performed using UV-written LPGs. Prior to deposition of the HfO<sub>2</sub> coating, tests are conducted to determine a deposition temperature at which the rate of LPG degradation is acceptably low. LPGs and, for reference, silicon wafers are then coated with HfO<sub>2</sub> using PEALD. Various coating thicknesses are investigated to determine the thickness range that promotes transition modes at low SRI, such as the RI of water. Coating thickness and uniformity are measured by SEM on coated optical fiber samples. As a reference, film thickness is measured by ellipsometry on a coated silicon wafer. For each deposition, the RI of the HfO<sub>2</sub> coating is also determined by ellipsometry on a coated silicon wafer. Two LPGs coated in the same deposition are characterized to investigate the performance of PEALD for tuning the transition point of different LPGs at a given SRI. This data is compared with the response of a coated LPG modeled using the software Optigrating.

### 2.1 High-temperature stability of LPGs

Commercial LPGs with a period of 450 μm and a length of 20 mm (Technica S.A, Beijing) inscribed in Corning single mode fiber, SMF-28e, were used in this work. One LPG was held at 150 °C for 18 hrs and a second LPG was held at 200 °C for 6.5 hrs. The gratings were fixed to a glass slide using epoxy, to keep fiber tension relatively constant during the experiment.

The wavelength shift and intensity of the attenuation band was monitored using a Micron Optics sm125 interrogator with a scan rate of 2 Hz and a resolution of 1 pm. Transmission spectra were acquired before and after high-temperature stability tests.

### 2.2 Deposition of HfO<sub>2</sub> by PEALD

Depositions were performed using the Fiji F200 (Cambridge NanoTech Inc., USA) ALD system equipped with a remote inductively coupled plasma source. HfO<sub>2</sub> was grown using TDMAHf as the metal precursor and O<sub>2</sub> plasma as the oxidizer. The deposition temperature was 150 °C and the external reservoir of the precursor TDMAHf was maintained at 75 °C. Rationale for the selection of this deposition temperature is presented in Section 3.1.

The deposition of HfO<sub>2</sub> comprised four steps: (1) TDMAHf pulse with Ar flow set at 60 standard cubic centimetres per minute (sccm); (2) TDMAHf purge with Ar flow set at 60 sccm; (3) plasma generated at 300 W, O<sub>2</sub> flow set at 20 sccm, and Ar flow set at 200 sccm; (4) O<sub>2</sub> purge with Ar flow set at 60 sccm. The pulse times for (1) and (3) are 0.25 s and 20 s, respectively. The purge times for (2) and (4) are 60 s and 10 s. These purge times are twice the duration specified by the system manufacturer for deposition on flat substrates [32].

Three depositions were conducted targeting coating thicknesses of 30 nm, 50 nm and 70 nm, referred to as Deposition 30, Deposition 50 and Deposition 70, respectively. Note that these labels correspond to nominal values, exact thickness measurements are obtained using characterization techniques described in Section 2.3.

The deposition growth rate provided by the manufacturer is approximately 0.108 nm/cycle; therefore, the number of cycles required to achieve the coating thicknesses of 30 nm, 50 nm and 70 nm are 279, 464 and 649, respectively. The time to complete each deposition was 7.7 hrs, 12.6 hrs and 17.6 hrs, respectively. The deposition times include initial waiting periods for the heaters to stabilize and for the substrates to achieve thermal equilibrium in the process chamber.

One LPG was coated with HfO<sub>2</sub> in Deposition 30 and is labeled as LPG30. Similarly, one LPG was coated in Deposition 70, labeled as LPG70. For Deposition 50, two LPGs were coated with HfO<sub>2</sub>, labeled as LPG50 and LPG50\*. Additionally, for Deposition 50, two optical fibers with no gratings were coated with HfO<sub>2</sub> and coating thickness was determined by scanning electron microscopy (SEM). For each deposition, a 2 inch diameter silicon wafer was placed near the LPGs and film thickness and RI were measured by ellipsometry.

### 2.3 Characterization of coatings

The thickness and RI of the coatings applied to the silicon wafers were determined by ellipsometry (Uvisel, Horiba Scientific, US). The ellipsometer acquires spectral data over the wavelength range between 245 - 2100 nm to which the Cauchy dispersion model is fit [33]. Thickness is a direct output of this model and RI is determined as a function of wavelength  $n(\lambda)$  using Eq. (1),

$$n(\lambda) = A + \frac{B \times 10^4}{\lambda^2} + \frac{C \times 10^9}{\lambda^4}, \quad (1)$$

where A, B and C are optical coefficients that are also direct outputs of the Cauchy dispersion model.

For each silicon wafer, the optical coefficients were obtained at the center of the wafer by a single measurement. Film thickness was measured at five locations, one point at the center of the wafer and four points located at the corners of a 15 mm square, centered on the first location.

Coating thickness was measured on two optical fibers, referred to as fiber 1 and fiber 2, both of which were coated in Deposition 50. Each fiber was cleaved into three sections

labeled as sections A, B and C. For each section, a total of 40 film thickness measurements were taken from 8 SEM images using the method described in [3].

#### 2.4 LPG characterization after deposition

After deposition, LPGs were placed in custom fixtures that allow immersion of the grating in glycerin solutions while maintain constant tension (see Fig. 1). The RI of the solutions was measured with a commercial Abbe refractometer (Leica, Mark II plus, Canada) at 589 nm with a resolution of  $1 \times 10^{-4}$  RI units.

The transmission spectrum of LPGs was obtained using a white light source (Yokogawa, AQ4305) and an optical spectrum analyzer (Yokogawa, AQ 6331) providing a wavelength range between 1200 - 1700 nm with a resolution of 0.5 nm. To acquire spectra with higher resolution, the interrogator sm125 was used.

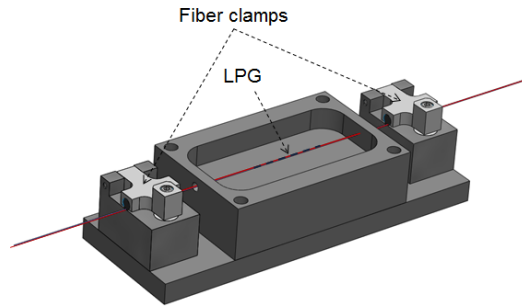


Fig. 1. Fixture used to hold LPGs during characterization tests.

#### 2.5 Modeling

Modeling was carried out using the software Optigrating (Optiwave, Canada). The linear polarized modes ( $LP_{0m}$ ) with  $m \geq 1$  are calculated based on the assumption that the difference between the RI of the core and cladding is small (*i.e.* weak guiding fibers).

The fiber parameters of the Corning SMF-28e used in this work are not fully disclosed by the manufacturer. The diameter of the core is defined as the mode-field diameter, the cladding diameter is given with an accuracy of  $\pm 7 \mu\text{m}$ , and the value of the core and cladding refractive indices vary with dopant concentration. Therefore, the refractive index of the core is slightly adjusted to achieve a modeled spectrum that was equivalent to the measured spectrum of the physical grating. The core and cladding radii used in the model are  $4.5 \mu\text{m}$  and  $62.5 \mu\text{m}$ , respectively. The core and cladding refractive indices are 1.4683 and 1.4628, respectively. The grating period and length are as specified by the LPG manufacturer for the physical grating (see Section 2.1) and index modulation was assumed to be  $3.8 \times 10^{-4}$ .

The model was used to simulate transition mode behavior of an LPG with a 60 nm coating with an RI of 1.932. The thickness and RI of the coating for the model were obtained by SEM and ellipsometry presented in Section 3.2, respectively.

### Results

#### 3.1 High-temperature stability of LPGs

The spectra of two LPGs in air at room temperature, before and after high-temperature stability tests, are shown in Fig. 2. For the LPG tested at  $150^\circ\text{C}$ , the resonance wavelength decreases by 10.2 nm. The depth of the attenuation band increases from 25 dB before the test to 27 dB after the test, corresponding to coupling efficiencies between core-cladding modes of 99.7% and 99.8%, respectively. The shape of the attenuation band after the test remains similar to the original spectrum. The full width at half maximum (FWHM) decreases from 2.0 nm before the test to 1.5 nm after the test.

For the LPG tested at 200 °C, the resonance wavelength decreases by 21 nm and the depth of the attenuation band decreases by 25 dB. The coupling efficiency between core-cladding modes decreases from 99.98% to 89%. Most notably, the shape of the attenuation band changes significantly and the FWHM increases from 0.90 nm to 13 nm.

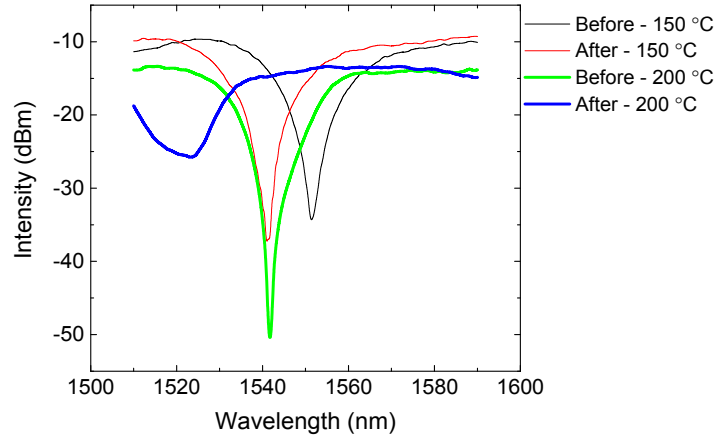


Fig. 2. Spectrum of LPG before and after high-temperature stability test at 150 °C and 200 °C.

It can be concluded from these results that long-term (*i.e.* 6.5 hours) exposure to temperatures at or above 200 °C will lead to significant thermal degradation of UV-written LPGs. This exposure time is on the order of magnitude required to increase the RI sensitivity of LPGs coated with HfO<sub>2</sub> by thermal ALD.

Based on results presented in Fig. 2, thermal degradation of UV-written LPGs at 150 °C over 18 hrs is relatively low. This exposure time is longer than the deposition time required to coat optical fibers with HfO<sub>2</sub> by PEALD at the targeted coating thicknesses tested in this work (*i.e.* between 30 - 70 nm). Therefore, the temperature of 150 °C was selected as the deposition temperature to coat LPGs with HfO<sub>2</sub> by PEALD.

### 3.2 Characterization of films

Ellipsometry measurements of thickness and RI for films deposited on flat silicon wafers are shown in Table 1. Non-uniformity was calculated as the difference between extreme values normalized by twice the mean, based on five measurement points.

For each deposition,  $n(\lambda)$  was calculated using Eq. (1), and the RI value at 1550 nm is shown in Table 1. The data shows that the RI of the film increases as the film thickness increases. The increase of RI with film thickness on silicon wafers has also been observed in the deposition of silicon nitride and diamond-like carbon by RF PECVD [34], as well as in the deposition of TiO<sub>2</sub> by thermal ALD [17]. However, there are also studies that report the opposite trend, for instance, the deposition of Al<sub>2</sub>O<sub>3</sub> on silicon wafers by thermal ALD [26]. Where the RI increases with film thickness, this phenomenon is attributed to an increase in film density and/or by the stress that the substrate induces in the film [17,34].

Growth per cycle (GPC) for the ALD process is calculated by a linear regression of the experimental film thickness data, expressed as a function of number of deposition cycles. Based on the three data points obtained in this work, the calculated GPC is 0.108 nm/cycle. This value is in agreement with the expected GPC provided by the ALD manufacturer.

The results of the SEM-based coating thickness measurements taken on fiber 1 and fiber 2 after Deposition 50 are shown in Fig. 3. For each section, the standard deviation was calculated from a total of 40 thickness measurements taken from 8 SEM images (see Section 2.3).

The relative standard deviation presented in Fig. 3 for Section A, B, C of Fiber 1 is 6.7%, 9.5%, and 6.4%, respectively, and for Section A, B, C of Fiber 2 is 4.4%, 5.3%, and 4.5%, respectively.

**Table 1. Thickness and RI of HfO<sub>2</sub> for different depositions measured on silicon wafers by ellipsometry**

|               | Depositions cycles | Film thickness (nm) | Non-uniformity (%) | RI ( $\lambda$ 155nm) (RIU) |
|---------------|--------------------|---------------------|--------------------|-----------------------------|
| Deposition 30 | 279                | 30.933              | 0.8                | 1.912                       |
| Deposition 50 | 464                | 50.616              | 0.8                | 1.932                       |
| Deposition 70 | 649                | 71.033              | 0.9                | 1.953                       |

The coating thickness and standard deviation calculated from measurements taken on the three fiber sections of fiber 1 and fiber 2 is  $59.7 \pm 5$  nm, and  $59.5 \pm 3$  nm, respectively.

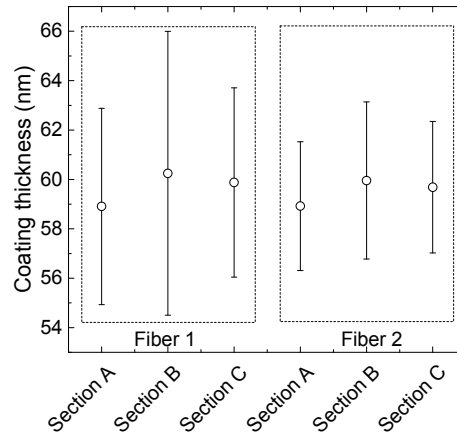


Fig. 3. Coating thickness measured by scanning electron microscopy on fibers coated by Deposition 50.

### 3.3 LPG characterization after deposition

Figure 4 shows the transmission spectra of LPG30, LPG50 and LPG70 in air, before (*i.e.* bare LPGs) and after deposition. The wavelength shifts after deposition for LPG30, LPG50 and LPG70 are 9.9 nm, 11.5 nm, and 11.5 nm, respectively. The depth of the attenuation band of LPG30 decreases by 6.3 dB and increases by 6.0 dB and 4.0 dB for LPG50 and LPG70, respectively. The coupling efficiency between core-cladding modes for all coated LPGs is higher than 99.0%. Additionally, for all LPGs investigated in this work, the shape of the attenuation band is preserved after the depositions. As expected, degradation of the transmission spectrum of the LPGs after deposition at 150 °C is acceptably low.

The wavelength shifts and the changes in the depth of the attenuation bands shown in Fig. 4 are believed to result both from exposure to elevated temperatures, as discussed earlier, and from the presence of the coating. The deposition of a coating material with an RI higher than silica is also expected to affect the transmission spectra of the LPGs [35]. The coating increases the effective RI of the cladding modes which leads to a decrease of the resonance wavelength. The effect of the coating on the depth of the attenuation bands is less clear. Results in the literature show that the coating of LPGs can lead both to an increase [8] and to a decrease in the depth of the attenuation band [12,35].

Figure 5 shows the characterization curves for LPG30, LPG50 and LPG70 based on immersion in solutions having a range of RI values. The characterization of a bare LPG is also depicted in Fig. 5. To help data visualization, the experimental data of the bare LPG was offset to the value of the coated LPGs, where the SRI is 1.0.

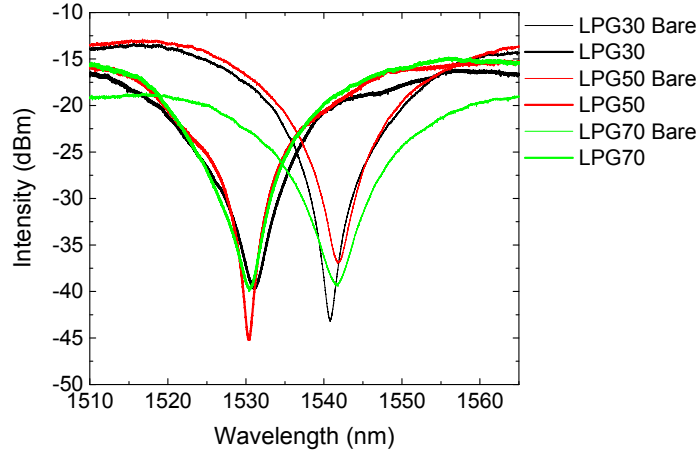


Fig. 4. Transmission spectrum of LPG30, LPG50 and LPG70 in air, before and after deposition.

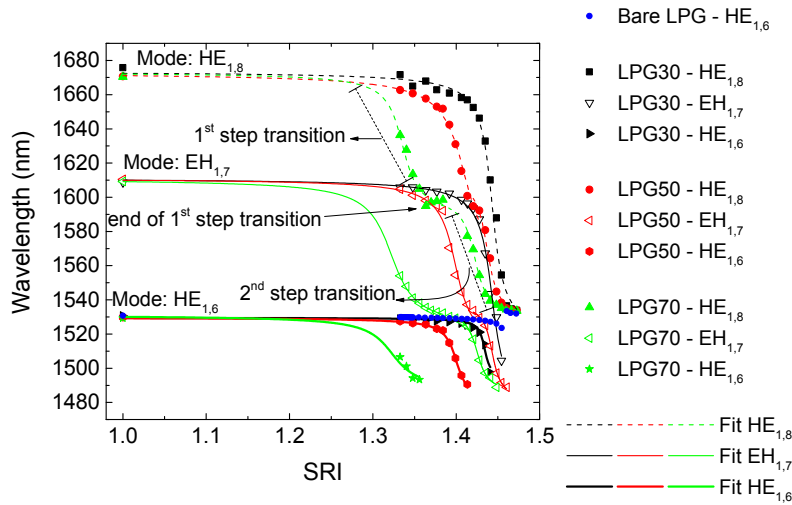


Fig. 5. Characterization curves of a bare LPG, LPG30, LPG50, and LPG70.

The modes depicted in Fig. 5 are hybrid modes (*i.e.*  $HE_{1,j}$  and  $EH_{1,j}$ ). In the absence of a coating, linearly polarized (LP) mode approximation (*i.e.*  $LP_{0,j}$  modes) is typically used, based on the assumption that the contrast between the RI of the core and cladding is small (*i.e.* weak guiding fibers). However, when LPGs are coated with a material of high RI, the contrast between the RI of the cladding and the coating becomes large and hybrid mode formulation is adopted [31,36,37]. The notation used to label the modes is based on the transmission spectra of the LPGs in air. The first attenuation band centered at the lowest wavelength is labeled as the  $HE_{1,2}$  mode. The  $HE_{1,2}$  mode is equivalent to the  $LP_{0,2}$  mode described by the LP mode approximation. The attenuation band of the  $HE_{1,2}$  mode is centered at a wavelength which is approximately equal to the center wavelength of the modeled  $LP_{0,2}$  mode. The second attenuation band with significant depth is labeled as the  $HE_{1,4}$  mode which is equivalent to the  $LP_{0,3}$  mode, and so on. Between each HE mode, an attenuation band with significantly reduced depth is labeled as EH mode. For example, the  $EH_{1,7}$  mode is located between the  $HE_{1,6}$  and the  $HE_{1,8}$  modes. The depth of the attenuation bands of the  $EH_{1,j}$  modes increases with the increase of SRI, as described later.

Figure 5 shows a phenomenon referred to as the *two-step transition* [31]. As the SRI increases, the resonance wavelength of the  $HE_{1,8}$  mode of LPG70 decreases until it approaches the original wavelength of the  $EH_{1,7}$  mode at an SRI of 1.365 (see *end of 1st step transition* in Fig. 5), at which point the data plateaus. As SRI increases above 1.384, the resonance wavelength of  $HE_{1,8}$  mode of LPG70 continues to decrease until it approaches the original wavelength of the  $HE_{1,6}$  mode.

The two-step transition is a behavior of transition modes that can be explained using the hybrid mode formulation. As the SRI increases, cladding modes (e.g. HE) higher than that guided by the coating (e.g.  $HE_{1,j}$ ) shift their resonance wavelength towards  $EH_{1,j-1}$  mode (i.e. first-step transition), followed by another transition of  $HE_{1,j}$  towards  $HE_{1,j-2}$  mode (i.e. second-step transition). The same is true for EH modes, i.e. there is a first-step transition of  $EH_{1,j}$  to  $EH_{1,j-1}$  mode, followed by a second-step transition of  $EH_{1,j}$  to  $EH_{1,j-2}$ . This phenomenon has been theoretically investigated by Villar *et al.* [31] and experimentally observed by Tatam *et al.* [36].

The two-step transition is less pronounced for LPGs with thinner coatings. For instance, the plateau between the first and second steps of the transition of the  $HE_{1,8}$  mode of LPG30 is not apparent in Fig. 5.

Figure 6 shows the change of wavelength and intensity of the transmission spectrum of LPG 70 as a function of SRI. It can be observed that, as the SRI increases, the intensity of the  $HE_{1,8}$  mode decreases until the resonance wavelength of this mode approaches the original wavelength of the  $EH_{1,7}$  mode. At this point the intensity of the  $HE_{1,8}$  is approximately 0 dB which is approximately the intensity of the  $EH_{1,7}$  mode at an SRI of 1.0. As the SRI increases above 1.4100, the intensity of the  $HE_{1,8}$  mode increases until the resonance wavelength of this mode approaches the original wavelength of the  $HE_{1,6}$  mode. At this point, the intensity of the  $HE_{1,8}$  mode is  $-15$  dB which is similar to the intensity of  $HE_{1,6}$  mode at an SRI of 1.0. The intensity of the  $EH_{1,7}$  mode undergoes an opposite trend. As the SRI increases, the intensity of the  $EH_{1,7}$  mode increases and reaches a maximum when the wavelength of this mode approaches the wavelength of the  $HE_{1,6}$  mode. After this, the intensity of the  $EH_{1,7}$  mode decreases until reaching approximately 0 dB. This behavior is discussed further in Section 4.

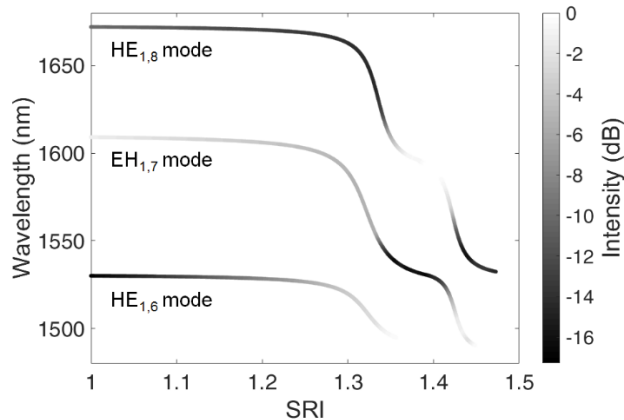


Fig. 6. Wavelength and intensity as a function of SRI for LPG70.

Figure 7 shows the spectrum of the LPG70 at different SRIs for additional visualization of the behavior shown in Fig. 6. In this figure, the  $HE_{1,6}$  mode is represented by letters A and B, the  $EH_{1,7}$  mode is represented by letters B' to G', and the  $HE_{1,8}$  mode is represented by G'' and H''. Each letter is associated with a different SRI, for example, B and B' correspond to the spectrum of LPG70 when surrounded by water (SRI of 1.3327).

Figure 7 shows that the depth of the attenuation band corresponding to the  $HE_{1,6}$  mode is significantly reduced when the SRI increases from 1.0 (see label A) to 1.3327 (see label B).

This occurs because the  $HE_{1,6}$  mode is operating in the transition region at the SRI of 1.3327 and the coupling coefficient of the  $HE_{1,6}$  mode decreases in this region (see Section 4).

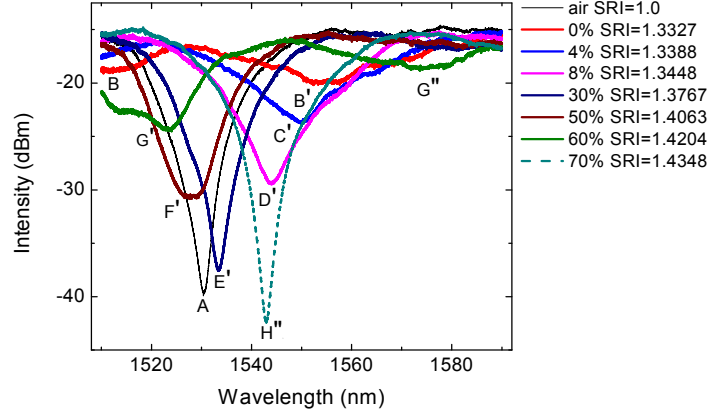


Fig. 7. Spectrum of LPG70 at different SRIs. The information is organized by (label, mode, SRI) as following: (A,  $HE_{1,6}$ , air), (B,  $HE_{1,6}$ , 0%), (B',  $EH_{1,7}$ , 0%), (C',  $EH_{1,7}$ , 4%), (D',  $EH_{1,7}$ , 8%), (E',  $EH_{1,7}$ , 30%), (F',  $EH_{1,7}$ , 50%), (G',  $EH_{1,7}$ , 60%), (G'',  $HE_{1,8}$ , 60%), and (H'',  $HE_{1,8}$ , 70%).

Similarly, the  $HE_{1,8}$  mode is operating in the second transition region at the SRI of 1.4204 (see label G''). When the SRI increases from 1.4204 to 1.4348, the  $HE_{1,8}$  mode shifts away of the transition region and the depth of the attenuation band increases (see label G'' and H'').

The depth of the attenuation band of the  $EH_{1,7}$  mode in Fig. 7 shows a different behavior with the variation of the SRI in the transition region than the  $HE_{1,6}$  and  $HE_{1,8}$  modes. Between an SRI of 1.3327 (see label B') and 1.3448 (see label D') the depth of the attenuation band of  $EH_{1,7}$  mode increases. In this SRI range, this mode is operating in the transition region. The depth of the attenuation band reaches a maximum value at approximately 1533 nm (see label E'). The region of maximum depth corresponds to the end of the 1st step transition of the  $EH_{1,7}$  mode of LPG70. After this, the depth of the  $EH_{1,7}$  mode decreases with further increase of SRI (see trend E' - G').

Experimental data presented in Fig. 5 is fitted by the Cumulative Lorentz equation, expressed as following [38]:

$$\lambda(SRI) = \lambda_0 + \frac{S_{\max} \Delta SRI}{2} \times \left[ \arctan \left( 2 \frac{SRI_{tp} - SRI}{\Delta SRI} \right) + \frac{\pi}{2} \right]. \quad (2)$$

For each mode,  $\lambda_0$  is the original resonance wavelength,  $S_{\max}$  is the maximum sensitivity,  $\Delta SRI$  represents the bandwidth at half maximum of the curve fits depicted in Fig. 8 and  $SRI_{tp}$  is the SRI of the transition point. For LPG30, only one curve fit was calculated for each mode because the characterization curves presented in Fig. 5 only show one-step transition. For LPG50 and LPG70, one curve fit was calculated for the  $HE_{1,6}$  and two curve fits were calculated for each  $EH_{1,7}$  and  $HE_{1,8}$  modes due to the two-step transition behavior of these modes.

Sensitivity data for coated LPGs are calculated as the absolute value of the first derivative of the Cumulative Lorentz fits. Sensitivity curves of LPG30, LPG50 and LPG70 are depicted in Figs. 8(a)-8(c), respectively.

For LPG30, Fig. 8(a) shows that the transition point (*i.e.* maximum sensitivity) of  $HE_{1,6}$ ,  $EH_{1,7}$  and  $HE_{1,8}$  modes occurs at SRIs of 1.4340, 1.4430, and 1.4430, respectively. For LPG 50, Fig. 8(b) shows that first-step transition of modes  $EH_{1,7}$  and  $HE_{1,8}$  is located at lower SRI, relative to second-step transitions. Figures 8(b) and 8(c) show that with the increase of coating thickness, the separation between the curves of first-step transition and second-step

transition increases. For instance, for the  $HE_{1,8}$  mode of LPG50, the first and second step transition occurs at the SRI of 1.4100 and 1.4371, respectively, whereas for the same mode of LPG70, the first and second step transition occurs at the SRI of 1.3355 and 1.4222, respectively.

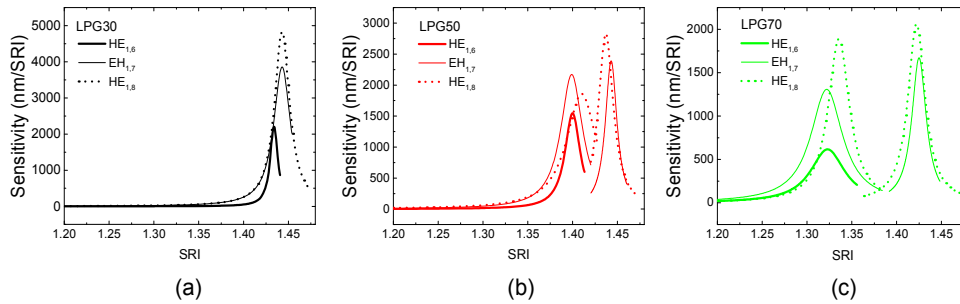


Fig. 8. Sensitivity curves of (a) LPG30, (b) LPG50, and (c) LPG70. Peaks correspond to transitions identified in Fig. 5.

Figure 9 shows the characterization curves of LPG50 and LPG50\*. Additionally, the figure shows the modeling of an LPG with a coating thickness of 60 nm and an RI of 1.932. The value of coating thickness was determined from thickness measurements taken on fiber 1 and fiber 2. The RI was measured by ellipsometry on the silicon wafer of Deposition 50 (see Section 3.2). The dispersion of the RI of  $HfO_2$  was calculated in the wavelength range between 1450 - 1700 nm using Eq. (1). The maximum RI variation is only 0.002 RI units. Therefore, the approximation of a constant RI value for a coating thickness of 60 nm is reasonable due to the low dispersion of the coating in the wavelength range investigated in this work. For comparison between the model and experimental results, data for LPG 50 and LPG50\* were offset to the value of the  $LP_{04}$  mode of the modeled LPG, where SRI is equal to 1.0.

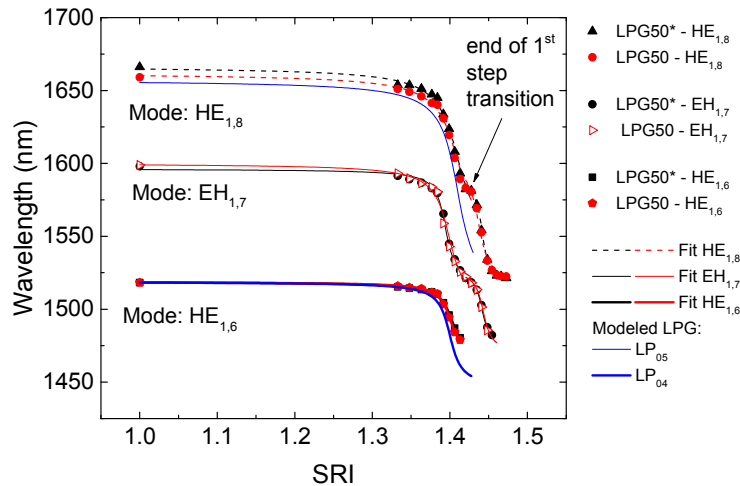


Fig. 9. Characterization curves of LPG50, LPG50\*, and modeled LPG.

Figure 9 shows that the behavior of LPG50 is identical to LPG50\* for all the modes monitored in this work. For the modeled LPG, the  $LP_{04}$  mode follows the same trend of the experimental LPGs; however, the  $LP_{04}$  mode undergoes a wider wavelength shift relative to the experimental data. Figure 9 also shows that the  $LP_{05}$  mode agrees with the  $HE_{1,8}$  mode at

the first-step transition. Model and experimental results differ for higher SRIs than that corresponding to end of first-step transition.

Figure 10 shows the sensitivity curves of the  $HE_{1,6}$  mode for LPG50 and LPG50\*, and the  $LP_{04}$  mode for the modeled LPG. The values of sensitivity predicted by the model are higher than the experimental results. The transition points of LPG50, LPG50\*, and  $LP_{04}$  mode occur at the SRI of 1.4000.

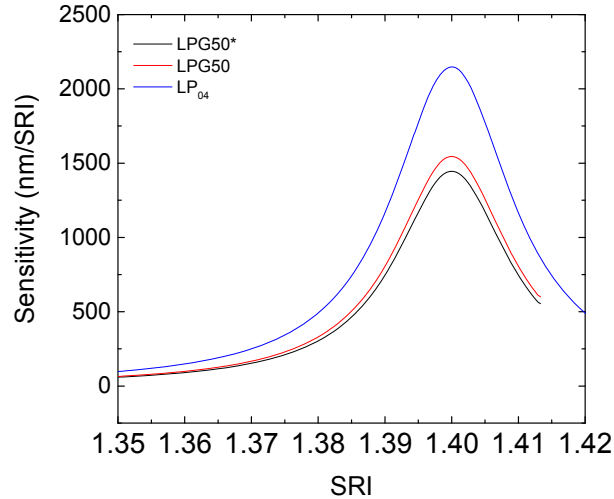


Fig. 10. Sensitivity curves of LPG50, LPG50\* and  $LP_{04}$  mode.

## Discussion

In this work, the first use of PEALD to coat UV-written LPGs is reported. This method allows deposition of conformal and uniform coating thicknesses on optical fibers. The measurements of coating thickness taken by SEM show low variability for two optical fibers coated in the same deposition. The mean coating thickness and standard deviation of fiber 1 and fiber 2 coated in Deposition 50 are  $59.7 \pm 5$  nm, and  $59.5 \pm 3$  nm, respectively.

As a result of this uniform deposition, two LPGs coated in the same deposition process exhibit identical behavior as a function of SRI. Both sensors show the transition point at the same SRI (*i.e.* 1.4000). This result suggests that multiple LPGs can be coated simultaneously with highly uniform coating thickness and with consistent thickness from fiber to fiber. This finding suggests that PEALD will allow scaling the production of sensors and thus reduce the deposition cost per sensor.

Film thickness measured on the silicon wafer coated by deposition 50 is lower than coating thickness measured by SEM on fiber 1 and 2 (see Table 1). This difference may be due to the initial growth of  $HfO_2$  on each substrate. In an ideal ALD process, GPC is constant during the deposition. However, in practice, GPC at the start of the deposition may differ due to the initial growth of  $HfO_2$  on a substrate, which is referred to as *nucleation* [39]. Nucleation depends on the concentration of reactive sites available on a substrate. In the case of  $HfO_2$ , the reactive sites are hydroxyl groups (OH). Therefore, the amount of  $HfO_2$  that is deposited during the initial cycles is proportional to the concentration of OH groups on the surface of the substrate [39]. Optical fibers used in this work are comprised primarily of silicon dioxide which provides more sites to which the OH groups can bond than is the case for the wafers, which are made of pure silicon. Therefore, optical fibers provide a higher concentration of nucleation sites and initial GPC is expected to be higher than on silicon wafers. Once the substrate is fully covered with  $HfO_2$ , GPC is expected to be relatively

constant, regardless of the substrate material because the growth takes place on the  $\text{HfO}_2$  film [39].

The major advantage of PEALD over thermal ALD is that the deposition temperature can be reduced, so as to avoid thermal degradation of the grating, without a significant increase in the purge times. The cycle durations specified by the ALD manufacturer for PEALD and thermal ALD at 150 °C are 55.3 s and 60.3 s, respectively. Considering a target coating thickness of 70 nm and assuming purge times with twice the duration specified by the ALD manufacturer, the times to complete each deposition for PEALD and thermal ALD are 16.2 hrs and 21.7 hrs, respectively, excluding time for thermal stabilization. The difference between deposition times of PEALD and thermal ALD becomes even more significant at lower deposition temperatures. For example, the recommended cycle durations for PEALD and thermal ALD at 90 °C are 145.3 s and 240.3 s, respectively. These cycle times correspond to deposition times of 43.8 hrs for PEALD and 86.5 hrs for thermal ALD to achieve a coating thickness of 70 nm, assuming purge times with twice the duration specified by the ALD manufacturer. Depositions at temperatures in the range of 85 °C may be needed in applications that require retention of the polymer coating that protects the optical fiber [17].

In this work, the use of PEALD was demonstrated to coat UV-written LPGs by selecting a deposition temperature that avoids significant thermal degradation (*i.e.* 150 °C). The spectra of LPGs before and after deposition show that the depth of the attenuation bands is not significantly reduced. This is important because it improves the detection of the attenuation bands, especially at the transition region where there is an intrinsic reduction of the depth of the attenuation bands.

Coating of LPGs with  $\text{HfO}_2$  promotes a two-step transition behavior, due to the high RI of  $\text{HfO}_2$ , which can be explained using the hybrid mode formulation. The depth of the attenuation band of an EH mode increases within the transition region, whereas this depth decreases for an HE mode.

The change of the depth of the attenuation bands in two-step transition behavior has been numerically investigated by Villar et al. [31]. Similar to the wavelength shift of the  $\text{HE}_{1,j}$  mode towards the  $\text{EH}_{1,j-1}$  mode at the first-step transition, the coupling coefficient of the  $\text{HE}_{1,j}$  mode also approaches the coupling coefficient of the  $\text{EH}_{1,j-1}$  mode [31]. At the second-step transition, the coupling coefficient of the  $\text{HE}_{1,j}$  mode approaches the coupling coefficient of the  $\text{HE}_{1,j-2}$  mode. This behavior is also observed for the transition of the coupling coefficient in the EH modes. The coupling coefficient of the HE modes is higher than that of the EH modes. This leads to a decrease in the depth of the attenuation bands when the HE modes approach the resonance wavelength of the EH modes, and an increase in the depth of the attenuation bands when the EH modes approach the resonance wavelength of the HE modes [31]. This behavior is illustrated in Fig. 6.

There is an important difference in the intensity of the attenuation bands in two-step transitions relative to the intensity of the attenuation bands in one-step transitions. In the latter case, the region of reduced intensity coincides with the region of higher sensitivity (*i.e.* transition point). In the former case, the region of the reduced intensity coincides with a region of lower sensitivity (see Fig. 6).

In this work, it is shown experimentally that the attenuation band of the  $\text{EH}_{1,7}$  mode of LPG70 reaches a significant depth (*i.e.* higher than 10 dB) when operating within the transition region (see Fig. 7). This is important because the EH modes can be tuned to operate closer to the transition point, relative to LP modes, with amplitudes that are readily detectable by commercial optical interrogators.

The transition region of LPG70 is located at low SRIs which leads to enhanced sensitivity of this grating at the SRI of water. The sensitivities of the  $\text{HE}_{1,6}$ ,  $\text{EH}_{1,7}$  and  $\text{HE}_{1,8}$  modes are 525 nm/SRI, 1050 nm/SRI and 1820 nm/SRI, respectively, at an SRI of 1.3327. The sensitivity of the  $\text{HE}_{1,6}$  mode of a bare LPG in the vicinity of water is 12 nm/SRI. These results show that the deposition of  $\text{HfO}_2$  on an LPG with a coating thickness of 70 nm leads to

an increase in sensitivity of 43 times at an SRI in the vicinity of water. Note that the sensitivity of a coated LPG is highly dependent on the cladding mode. Therefore, the sensitivity of LPGs coated by PEALD can be further improved by tuning the grating parameters to promote cladding modes of higher order, or by etching the fiber to combine the transition mode behavior with the dispersion turning point [17,40,41].

The LP modes of a coated LPG are modeled using Optigrating software and compared with data of the HE modes that were obtained experimentally. Although this approach is not suitable to model the response of both hybrid modes (HE and EH modes), we show that it can be used to estimate the SRI at which the transition point of the HE mode occurs.

## Conclusions

PEALD is investigated for coating of LPGs with HfO<sub>2</sub>. This method allows lower deposition temperatures relative to thermal ALD to enable coating of UV-written LPGs without thermal degradation.

Depositions were performed at 150 °C and the process parameters, pulse time and purge time, were selected to ensure only ALD-type reactions. As a result, excellent film uniformity was achieved on silicon wafers measured by ellipsometry (*i.e.* non-uniformity between 0.8% - 0.9%). Consistent wavelength shifts, as a function of SRI, were also achieved on LPGs coated by the same deposition. The transition point of both LPG50 and LPG50\* occurs at 1.4000. The maximum sensitivity of LPG50 and LPG50\* is 1545 nm/SRI and 1445 nm/SRI, respectively.

Coating of LPGs with HfO<sub>2</sub> promotes two-step transitions due to the high RI of the coating material. These transitions can be explained using hybrid mode formulation. The attenuation bands of the HE and EH modes are readily detectable at the transition point. The results obtained in this work suggest that two-step transition behavior can be used to monitor SRI changes while operating closer to the transition point compared to one-step transitions.

## Acknowledgments

The authors gratefully acknowledge funding provided by the Natural Sciences and Engineering Research Council of Canada (NSERC), Carbon Management Canada (CMC), and the Korean Carbon Capture and Sequestration R&D Center (KCRC). This work made use of the shared facilities of 4D LABS, which are supported by the Canada Foundation for Innovation (CFI), British Columbia Knowledge Development Fund (BCKDF), Western Economic Diversification Canada, and Simon Fraser University.

**Appendix D: Refractive index sensor based on inline Mach-Zehnder interferometer coated with hafnium oxide by atomic layer deposition**

L. Melo, G. Burton, P. Kubik, and P. Wild, “Refractive index sensor based on inline Mach-Zehnder interferometer coated with hafnium oxide by atomic layer deposition,” *Sensors Actuators B Chem.*, vol. 236, pp. 537–545, 2016

Reprinted, with permission, from *Sensors and Actuators B: Chemical*, Elsevier



# Refractive index sensor based on inline Mach-Zehnder interferometer coated with hafnium oxide by atomic layer deposition



Luis Melo<sup>a,\*</sup>, Geoff Burton<sup>a</sup>, Philip Kubik<sup>b</sup>, Peter Wild<sup>a</sup>

<sup>a</sup> Department of Mechanical Engineering and Institute for Integrated Energy Systems (IESVic), University of Victoria, P.O. Box 3055, Victoria, BC, V8W 3P6, Canada

<sup>b</sup> 4D Labs, Simon Fraser University, 8888 University Drive, Burnaby, BC, V5A 1S6, Canada

## ARTICLE INFO

### Article history:

Received 16 February 2016

Received in revised form 2 June 2016

Accepted 3 June 2016

Available online 7 June 2016

### Keywords:

Photonic crystal fiber

Mach-Zehnder

Interferometer

Atomic layer deposition

Coating

Refractive index

## ABSTRACT

A fiber-optic interferometer based on a Mach-Zehnder configuration is coated with hafnium oxide by atomic layer deposition (ALD) to increase the sensitivity to the refractive index of the surrounding medium (SRI). The sensor is based on the intermodal interference between the core and a cladding mode of a photonic crystal fiber (*i.e.* PCF interferometer). Prior to coating of PCF interferometers, the purge time, a process parameter of ALD is investigated to achieve precise control over coating thickness. Three different depositions with purge times of 10 s, 20 s, and 30 s were selected. The coating thickness and uniformity were measured by scanning electron microscopy on standard single-mode optical fibers. As a reference, the film thickness was measured by ellipsometry on a silicon wafer. The results show that control of coating thickness on optical fibers is achieved by selecting longer purge times, compared to conventional depositions on flat substrates. The suitable process parameters to coat standard single-mode fibers were selected for the coating of the PCF interferometers. The effect of coating thicknesses on the sensitivity of these sensors was investigated by depositions targeting coating thicknesses of 30 nm, 40 nm, 50 nm, 60 nm, 70 nm and 90 nm. Sensitivity of 1307 nm/SRI at an SRI range in the vicinity of water was achieved for an interferometer coated by a deposition targeting a coating thickness of 60 nm. This sensitivity value is the highest reported in the literature for a PCF interferometer.

© 2016 Elsevier B.V. All rights reserved.

## 1. Introduction

Refractive index (RI) measurements are important in various applications including biochemical analysis to understand mechanisms of drug actions [1] and environmental sensing to measure concentrations of carbon dioxide in water [2], levels of salinity in water [3] and gas concentrations in the atmosphere [4].

A number of fiber-optic sensors have been developed to monitor refractive index changes in the surrounding medium (SRI) based on the interaction between the fraction of light guided in an optical fiber that extends beyond the fiber (*i.e.* the evanescent field) and the medium surrounding the fiber. Examples of evanescent field sensors include tilted fiber Bragg gratings (TFBGs) [5], long period gratings (LPGs) [6], fiber tapers [7], and fiber-optic interferometers [8]. Fiber-optic interferometers with sensitivity to SRI are divided into different configurations namely Fabry-Perot

interferometers, Michelson interferometers, and Mach-Zehnder interferometers (MZIs) [8].

Over the last decade, MZIs based on the interference between the core and a cladding mode of a photonic crystal fiber (PCF) have been investigated to measure SRI due to the possibility of producing low-cost sensors using a simple fabrication method [9,10]. This type of sensor will be referred in this article as *PCF interferometer*. A schematic of a PCF interferometer is shown in Fig. 1.

A PCF interferometer is fabricated by splicing a segment of a PCF between a lead-in and a lead-out single-mode fiber (SMF). The electric arc of a fusion splicer is used to collapse the holes of the PCF at the splicing regions. At the first splice, the core mode of the SMF is diffracted by the region of the collapsed holes and couples to the core mode and cladding mode of the PCF [10]. At the second splice, the SMF acts as a spatial filter because it only supports a core mode, and thus the core mode and the cladding mode of the PCF are recombined and coupled to the core mode of the SMF [10].

The core mode and the cladding mode of the PCF accumulate a phase difference due to the difference between the effective refractive indices of each mode ( $n_{\text{eff}}$ ). This phase difference leads to an interferometric behaviour between the two modes and, as

\* Corresponding author.

E-mail address: [luismelo@uvic.ca](mailto:luismelo@uvic.ca) (L. Melo).

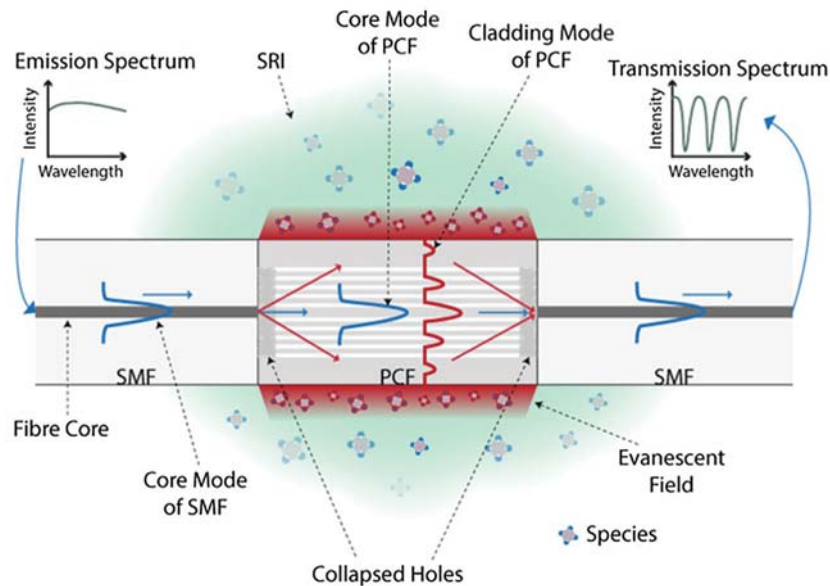


Fig. 1. Illustration of a PCF interferometer monitoring SRI changes caused by the presence of species within the evanescent field of the sensor.

a consequence, the transmission spectrum exhibits a sinusoidal interference pattern.

The value of  $n_{\text{eff}}$  of the cladding mode of the PCF is sensitive to the SRI in the region into which the evanescent field of this mode extends [9]. As a consequence, changes in the SRI can be determined by monitoring the wavelength shift of the interference pattern. The sensitivity of a PCF interferometer increases with the increase of the SRI. At an SRI range between 1.33–1.38 the sensitivity is approximately 100 nm/SRI and at an SRI range between 1.38–1.46 the sensitivity is approximately 700 nm/SRI [9].

The sensitivity of PCF interferometers at a target SRI can be enhanced by coating the sensor with a material that has a RI greater than the RI of silica. This was shown by Smietana et al. using radio frequency plasma enhanced chemical vapor deposition to coat PCF interferometers with silicon nitride [11]. The coating shifts the distribution of the light field of the cladding mode towards the radial edge of the PCF, increasing the energy density in this region [11]. This leads to an increase in the intensity of the evanescent wave that penetrates in the surrounding medium which increases the SRI sensitivity of a coated PCF interferometer relative to a bare device.

The sensitivity of a coated PCF interferometer at a given SRI is a function of the thickness and RI of the coating [11]. Therefore, precise control over coating thickness is an important parameter when designing PCF interferometers to operate at a target SRI. Directional deposition methods, such as chemical vapor deposition (CVD), are not well suited to this application as it is difficult to control coating thickness and uniformity over the cylindrical geometry of the fiber [12].

Atomic layer deposition (ALD) has been identified as one of the primary candidates to achieve conformal (*i.e.* full step coverage) and uniform coatings on complex substrates with precise control of the coating thickness [13]. A material is deposited by ALD by reacting two precursors (*i.e.* gaseous reactants) in a four-step process comprising 1) exposure to the first precursor, 2) purging the process chamber using nitrogen or argon, 3) exposure to the second precursor, and 4) purging the process chamber with nitrogen or argon. These four steps comprise one cycle, and the growth-per-cycle (GPC) is calculated by dividing the film thickness by the number of cycles.

Recently, ALD has been investigated for the application of coatings on fiber-optic sensors. Examples include LPGs [14,15],

TFBGs [16], fiber tapers [17], and interferometers based on double cladding fiber coated with  $\text{Al}_2\text{O}_3$  [18], as well as LPGs coated with  $\text{TiO}_2$  [19]. Metal oxides deposited by ALD are potentially useful as coatings for optical fibers because they have high RI, low optical losses, and strong adhesion to optical fibers [15].

These previous studies of ALD coatings on optical fibers focus mainly on the optical performance of the coated sensors. Determination of the deposition process parameters for precise control of coating thickness is not described in detail.

In commercial ALD systems, the precursor pulse times and purge times are optimized for each type of precursor and deposition temperature. The pulse time is selected to ensure saturation (*i.e.* the precursors must reach all the active sites on the substrate) [20,21]. If the precursor dose is below the saturation level, the GPC decreases, and this may result in thickness gradients along the deposited film on the substrate [20,21]. The purge time is selected to provide sufficient flow to remove unreacted precursors and by-products from the process chamber [20,21]. Short purge times lead to an increase in the GPC as a result of reactions occurring between removal of the first precursor and injection of the second precursor. The GPC increase is an indication that the self-limiting characteristic of ALD is not fulfilled and instead, CVD takes place, which also may result in thickness gradients along the film on the substrate [22].

ALD on surfaces that are not flat may require deposition parameters, such as pulse and purge times, to be adjusted to achieve adequate control over coating thickness [13,23]. Kim et al. describe the deposition of  $\text{Al}_2\text{O}_3$  and ZnO on carbon nanotubes at temperatures between 40 °C and 120 °C [24]. Higher GPCs are reported for  $\text{Al}_2\text{O}_3$  and ZnO depositions than those expected from ALD on flat substrates, likely due to the mix of the precursors [24]. Li et al. report the deposition of ZnO on multi-walled carbon nanotubes at 200 °C [23]. In this work, a specified GPC is obtained by using longer purge times. The authors conclude that CNTs require longer purge times to avoid CVD, due to the small free space between nanotubes which makes the purging of precursors difficult [23].

In the current work, the purge time required to achieve a controlled deposition with a desired coating thickness of  $\text{HfO}_2$  on optical fibers is investigated. Standard SMF was coated with  $\text{HfO}_2$  using tetrakis(dimethylamido) hafnium(IV) (TDMAHf) as the metal precursor and  $\text{H}_2\text{O}$  as the oxygen precursor. PCF interferometers were coated using the ALD process parameters determined in this

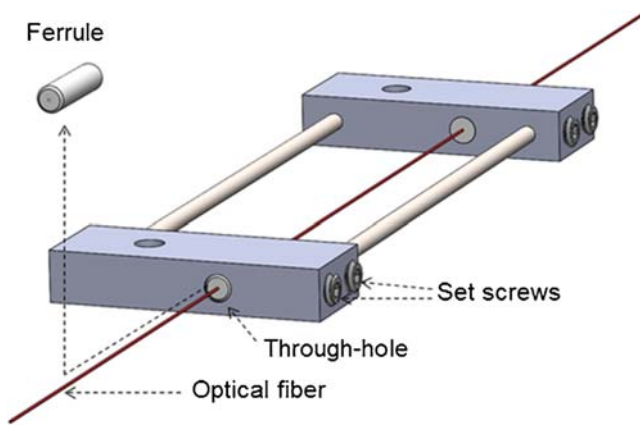


Fig. 2. Fiber fixture showing an optical fiber gripped by ferrules at each end.

study of the purge times for coating standard SMF. The results show that the highest sensitivity of a PCF interferometer at low SRI is 1307 nm/SRI for a coating thickness of 60 nm. This work provides a novel contribution to design coated PCF interferometers with high sensitivity at low SRIs by applying controlled coating thicknesses.

## 2. Methods

Prior to deposition of  $\text{HfO}_2$  on PCF interferometers, tests were conducted to determine the purge time that achieves a target coating thickness on optical fibers. Standard SMF and silicon wafers are used as substrates for three different depositions with purge times of 10 s, 20 s, and 30 s. Fiber fixtures were designed and manufactured to support the optical fibers during deposition. To determine the effect of purge time on the substrates, coating thickness is measured on optical fibers by scanning electron microscopy (SEM) and film thickness is measured on silicon wafers by ellipsometry. PCF interferometers are then coated with  $\text{HfO}_2$  by selecting the process parameters determined by the study of purge time. The effect of different coating thicknesses on the SRI sensitivity of PCF interferometers is investigated.

### 2.1. Fiber fixtures

Fixtures were custom-built to support optical fibers during the deposition process. As shown in Fig. 2, each fiber fixture has a block at each end with a single through-hole of diameter of 2.8 mm, to accommodate standard ceramic ferrules (CFLC128, Thorlabs, US). The ferrules have an external diameter of 2.5 mm and an internal diameter of 128  $\mu\text{m}$  and are fixed in the holes using set screws located at the side of the fiber fixture. The fibers are cleaned with isopropanol and fed through the ferrules as illustrated in Fig. 2. The optical fibers used in this work have a cladding diameter of 125  $\mu\text{m}$ ; therefore, the fiber fits snugly into the ferrules and remains relatively taut during deposition. The fiber fixture suspends the optical fiber above the substrate table of the ALD, allowing the gas precursors to flow freely around the cylindrical surface of the fiber. The distance between the optical fiber and the substrate table is 2.4 mm.

### 2.2. Atomic layer deposition of $\text{HfO}_2$

The optical fibers were coated with  $\text{HfO}_2$  using the precursors TDMAHf and  $\text{H}_2\text{O}$  and the Fiji F200 ALD system (Cambridge NanoTech Inc., US). The temperature in the process chamber was 200 °C and the temperature of TDMAHf, prior to injection, was 75 °C.

The injection of the precursors into the process chamber and the subsequent purge were performed using argon (Ar) as a carrier

Table 1  
Pulse and purge times investigated to coat standard SMF with  $\text{HfO}_2$ .

| Label        | TDMAHf pulse (s) | TDMAHf purge (s) | $\text{H}_2\text{O}$ pulse (s) | $\text{H}_2\text{O}$ purge (s) |
|--------------|------------------|------------------|--------------------------------|--------------------------------|
| Deposition 1 | 0.25             | 10               | 0.06                           | 10                             |
| Deposition 2 | 0.25             | 20               | 0.06                           | 20                             |
| Deposition 3 | 0.25             | 30               | 0.06                           | 30                             |

gas with a flow rate of 60 standard cubic centimeters per minute (sccm). Each ALD cycle comprises a pulse of TDMAHf, followed by an Ar purge, followed by a pulse of  $\text{H}_2\text{O}$ , followed by another Ar purge.

#### 2.2.1. Investigation of purge time of ALD

Standard SMF (SMF-28e, Corning, US) was used to investigate the purge time that leads to a complete depletion of the products inside the process chamber. The process parameters to coat standard SMF are expected to be identical to those required to coat PCF because both fibers have the same geometry and similar chemical composition. Therefore, standard SMF was used as the substrate for this study due to its lower price relative to PCF.

To determine adequate purge time for coating standard SMF, three depositions were conducted with purge times of 10 s, 20 s, and 30 s, referred to as Depositions 1, 2, and 3, respectively. The pulse times were kept the same in Deposition 1–3. Table 1 summarizes the deposition parameters used in this study.

The GPC of  $\text{HfO}_2$  is approximately 0.11 nm/cycle, as specified by the manufacturer of the ALD system. The target coating thickness in this study is 50 nm; therefore, 464 cycles are required to achieve this coating thickness by ALD. Completing Depositions 1–3 required 2.6 h, 5.2 h, and 7.8 h, respectively.

For each deposition, a 2 in. diameter silicon wafer was placed on the substrate table in addition to the fiber fixture. The coating applied to this wafer was used as a reference for the thicknesses of the coatings applied to the standard SMF.

#### 2.2.2. Coating of PCF interferometers

PCF interferometers were fabricated using a commercial splicer (FSM-40PM, Fujikura, Japan) to splice a segment of a PCF (LMA10, NKT Photonics, Denmark) with a length of 20 mm between standard SMFs. The arc power and arc time used to collapse the holes of the PCF at the junction between the PCF and standard SMF were 20 bit (relative unit provided by the splicer) and 2 s, respectively. After fabrication, the PCF interferometers were placed in fiber fixtures as described in Section 2.1.

PCF interferometers were then coated by ALD using process parameters determined by the study of purge times for coating standard SMF. The rationale for the selection of these parameters is presented in Section 3.1. The ALD cycle comprised a pulse of TDMAHf (0.25 s), followed by an Ar purge (20 s), followed by a pulse of  $\text{H}_2\text{O}$  (0.06 s), followed by another Ar purge (20 s).

The effect of coating thickness on the SRI sensitivity of PCF interferometers was investigated by selecting six depositions targeting different coating thicknesses, namely 30 nm (Deposition 30), 40 nm (Deposition 40), 50 nm (Deposition 50), 60 nm (Deposition 60), 70 nm (Deposition 70) and 90 nm (Deposition 90). The number of cycles required to achieve the target coating thicknesses is calculated based on the GPC specified by manufacturer (i.e. 0.11 nm/cycle). Table 2 summarizes the ALD parameters used in each deposition.

For each deposition, a silicon wafer and a fiber fixture with a PCF interferometer were placed on the substrate table. The coated PCF interferometers were labeled as PCF 30, PCF 40, PCF 50, PCF 60, PCF 70, and PCF 90, the label corresponds to the nominal thickness of each deposition.

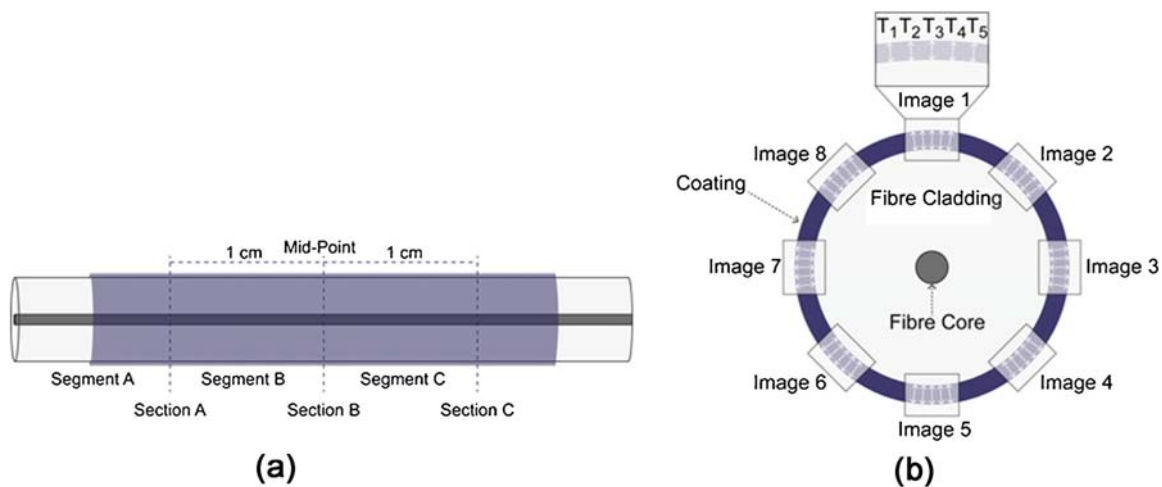


**Fig. 3.** (a) Schematic view of a coated fiber showing the location of fiber sections that were mechanically cleaved and then imaged. (b) Schematic view of the cross section view of a fiber section showing the location of image samples.

**Table 2**

ALD parameters selected to coat PCF interferometers.

| Label         | Target coating thickness (nm) | Number of cycles | Deposition time (h) |
|---------------|-------------------------------|------------------|---------------------|
| Deposition 30 | 30                            | 278              | 3.4                 |
| Deposition 40 | 40                            | 371              | 4.4                 |
| Deposition 50 | 50                            | 464              | 5.5                 |
| Deposition 60 | 60                            | 556              | 6.5                 |
| Deposition 70 | 70                            | 649              | 7.6                 |
| Deposition 90 | 90                            | 834              | 9.7                 |

### 2.3. Measurement of the coating thickness

#### 2.3.1. Ellipsometry

The film thickness of  $\text{HfO}_2$  on silicon wafers coated by Deposition 1–3 (see Section 2.2.1) was measured with an ellipsometer (Uvisel, Horiba Scientific, US). For each wafer, one ellipsometry measurement was taken at the center of the wafer. An ellipsometry measurement is based on the polarization change of a light beam that is reflected from the surface of a coated silicon wafer. The Cauchy dispersion model was selected to fit the experimental data [25].

The simulation of the Cauchy dispersion model is performed using proprietary software provided by the ellipsometer manufacturer. The film thickness of  $\text{HfO}_2$  is obtained from the simulation by using an iterative process to optimize RI and extinction coefficient as a function of wavelength [26]. For these simulations, a two-layer model is defined with silicon as the substrate layer and  $\text{HfO}_2$  as the ALD film. As a reference, the RI of  $\text{HfO}_2$  at the wavelength of 1550 nm, which is defined by the Cauchy dispersion model as a starting condition for the simulations, is approximately 1.95.

To determine how well the simulations using the Cauchy dispersion model fit the experimental data, the *reduced biased estimator* parameter ( $\chi^2$ ) was used as the figure-of-merit [26]. A smaller  $\chi^2$  indicates a better fit and, typically,  $\chi^2 \approx 1$  represents a good fit whereas  $\chi^2 \gg 1$  represents a poor fit.

Film thicknesses on silicon wafers coated by Depositions 30, 40, 50, 60, 70, and 90 were measured by a different ellipsometer (MM-16, Horiba Scientific, US). The measurements and modeling were conducted using an identical procedure as described above for measurements on silicon wafers coated by Deposition 1–3.

#### 2.3.2. Scanning electron microscopy

SEM (Hitachi S-4800) was used to measure the thickness of the  $\text{HfO}_2$  coating on standard SMF coated by Depositions 1–3.

Images were taken at a voltage of 1 keV, an emission current of 10  $\mu\text{A}$ , a working distance of 4 mm and at magnifications between 50 000 and 250 000 times. Prior to imaging, the fiber sections were coated with carbon (Cressington 208C, Ted Pella, US) to increase the conductivity and thus reduce image charging effects.

For each deposition, the coated standard SMF (*i.e.* fiber sample) was cleaved at three locations using a mechanical cleaver; at the mid-point of the fiber sample and at points located 1 cm to either side of the mid-point, as shown in Fig. 3(a). Each segment was mounted in a 90° SEM stub (Ted Pella INC., US) to allow imaging of the cleaved end. These cleaved ends are referred to as sections A, B and C in Fig. 3(a).

For each fiber section, an SEM image was taken at eight different locations spaced approximately equally around the fiber edge (see Fig. 3(b)). Within each of these eight images, thickness measurements were taken at five locations, as illustrated in the expanded view of Image 1 in Fig. 3(b). These measurements were used to calculate the mean coating thickness and its standard deviation on each fiber section (*i.e.* 40 data points). For each fiber sample, mean coating thickness and standard deviation were determined using all the data from all of the images taken at the three fiber sections (*i.e.* 120 data points).

Film thickness was also measured by SEM (Helios Nanolab, FEL, US) on a silicon wafer coated by Deposition 2. For this analysis, a 10 mm by 10 mm chip was cut from the silicon wafer. Cross-section images of the interface between the silicon wafer and  $\text{HfO}_2$  film were taken to measure film thickness on the edge of the chip. The mean film thickness and its standard deviation were determined from images taken at ten locations along the edge of the chip. One measurement of thickness was taken from each image (*i.e.* 10 data points).

### 2.4. SRI characterization of PCF interferometers

The response of the PCF interferometers to the SRI was characterized with mixtures of glycerin and water solutions providing a SRI range from 1.3328 (*i.e.* distilled water) to 1.4602 (*i.e.* 100% glycerin). The RI measurements of the solutions were made with an Abbe refractometer at 589 nm with a resolution of  $1 \times 10^{-4}$  RI units. The transmission spectrum of the PCF interferometers

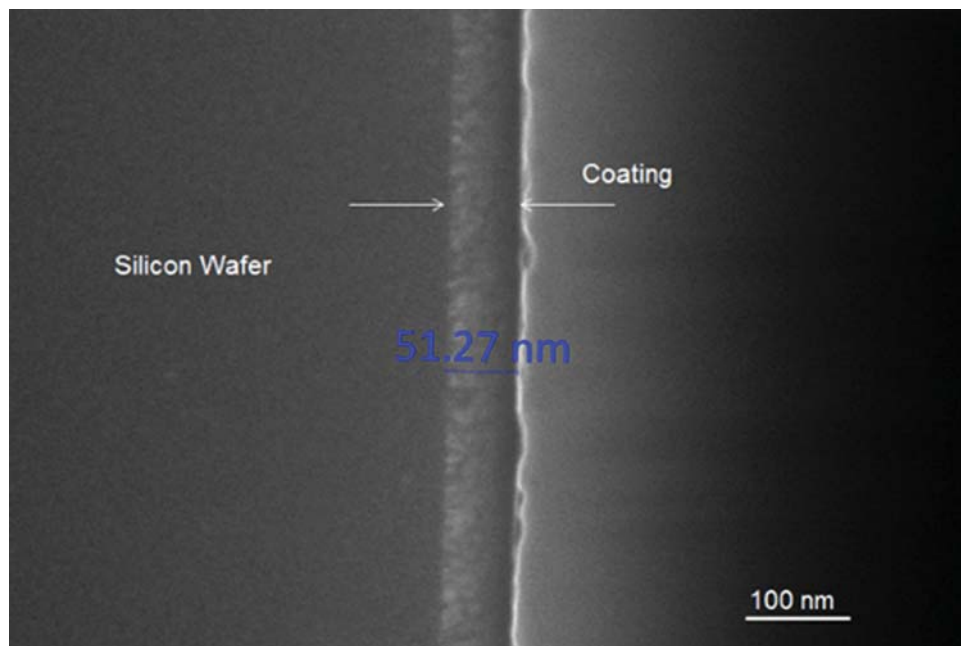


Fig. 4. SEM image of film thickness of  $\text{HfO}_2$  on the silicon wafer coated by Deposition 2.

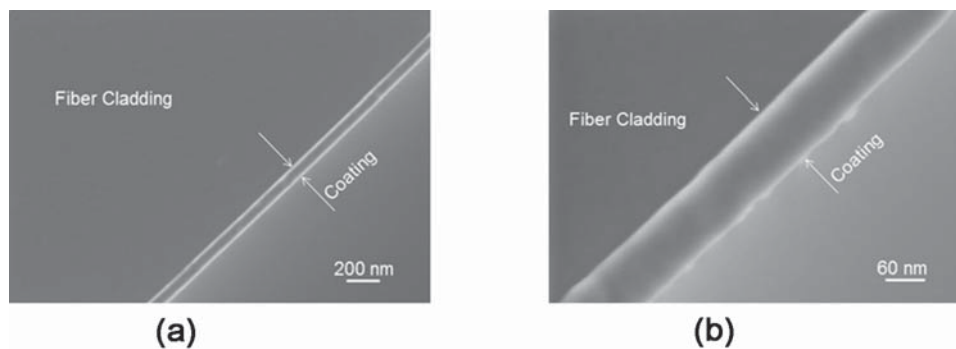


Fig. 5. (a) Deposition 2, fiber section B using a magnification of 50,000 times (b) Close-up of Fig. 5(a) with a magnification of 200,000 times.

was obtained with an optical interrogator (sm125, Micron Optics, US) with a resolution of 1 pm over the wavelength range of 1510–1590 nm.

For these characterizations, the sensors were placed in custom-built holders to provide a constant fiber tension, allowing the sensor to be fully immersed in the testing solutions. PCF 30 was characterized before (*i.e.* bare PCF) and after coating, whereas the other PCF interferometers were characterized after coating.

### 3. Results

#### 3.1. Investigation of purge time on thickness

The film thicknesses measured by ellipsometry on silicon wafers after Depositions 1, 2, and 3, are 69.45 nm, 53.11 nm, and 50.30 nm, respectively. The GPC of Depositions 1, 2, and 3, calculated from the film thickness results, is 0.15 nm/cycle, 0.11 nm/cycle, and 0.11 nm/cycle, respectively.

The GPC provided by the ALD manufacturer is 0.11 nm/cycle. Therefore, Deposition 1 shows a high GPC, whereas the results obtained by Depositions 2 and 3 show excellent agreement with the expected GPC. The effect of the purge time on GPC is discussed further in Section 4.

Film thickness was also measured by SEM on a silicon wafer coated by Deposition 2 to compare with a result obtained by ellipsometry. Fig. 4 shows a representative SEM image of the cross section of the chip with a film thickness of 51.27 nm. The mean film thickness and standard deviation obtained from data of ten SEM measurements on different images is  $51.7 \pm 0.9$  nm. This value confirms a good agreement (*i.e.* within 2.7%) between ellipsometry and SEM measurements on the same silicon wafer.

A representative SEM image of an  $\text{HfO}_2$ -coated fiber section is shown in Fig. 5(a). The edge of the fiber captured by the image is fully coated with  $\text{HfO}_2$  (*i.e.* conformal coating). Conformal coating was observed around the full circumference of all fiber sections. A close-up of Fig. 5(a) is shown in Fig. 5(b) using a magnification of 200,000.

Fig. 6 shows the results of the coating thickness measurements made with the method illustrated in Fig. 3. For each fiber sample, data for the three fiber sections are grouped within a rectangle. Fig. 6 shows that the coating thickness values for Deposition 1 are significantly higher than for Depositions 2 and 3. For Deposition 1, the mean coating thicknesses of sections A, B, and C are 122 nm, 120 nm, and 108 nm, respectively. For Deposition 2, the mean coating thicknesses of sections A, B, and C are 66 nm, 67 nm, 65 nm, respectively. For Deposition 3, the mean coating thicknesses of sections A, B and C are 65 nm, 65 nm, and 68 nm, respectively.

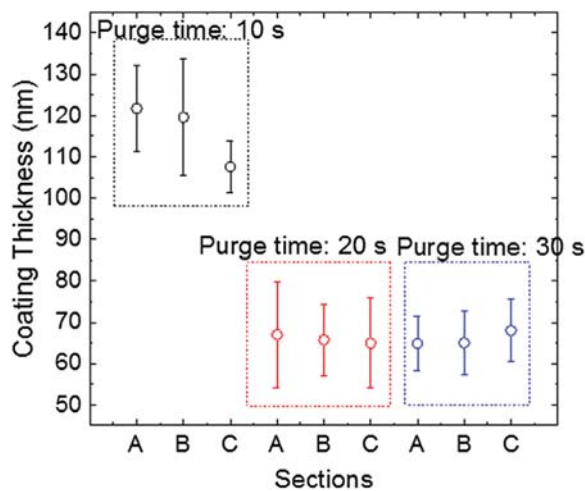


Fig. 6. Measurement of coating thickness on fiber sections by SEM.

**Table 4**  
Film thickness measured on silicon wafers by ellipsometry.

| Label         | Cycles | Thickness (nm) | $\chi^2$ |
|---------------|--------|----------------|----------|
| Deposition 30 | 278    | 29.98          | 0.20     |
| Deposition 40 | 371    | 39.99          | 0.10     |
| Deposition 50 | 464    | 50.01          | 0.33     |
| Deposition 60 | 556    | 59.88          | 2.35     |
| Deposition 70 | 649    | 69.97          | 0.61     |
| Deposition 90 | 834    | 89.85          | 3.75     |

The mean coating thickness and standard deviation of each fiber sample for Depositions 1–3, are  $116 \pm 12$  nm,  $66 \pm 11$  nm, and  $66 \pm 7$  nm, respectively, corresponding to GPCs of 0.25 nm/cycle, 0.14 nm/cycle, and 0.14 nm/cycle, respectively.

Table 3 summarizes the thickness and GPC results for both the wafers and the fiber samples.

The results of coating thickness measured by SEM on fiber samples coated by Deposition 2, and 3 show consistent coating thicknesses independent on purge time. The process parameters of Deposition 2 were selected to coat PCF interferometers because it leads to faster deposition rates compared to process parameters of Deposition 3, which reduces the deposition cost.

### 3.2. Investigation of depositions on PCF interferometers

For each deposition, film thickness was measured by ellipsometry on a silicon wafer placed next to the fiber fixture (see Section 2.2.2). The values of film thickness agree with the expected values (i.e. nominal coating thickness). The maximum difference between the experimental thickness and the nominal thickness is 0.2%, corresponding to the coating thickness obtained on a silicon wafer coated in Deposition 90. As shown in Table 4, the values of  $\chi^2$  are between 0.10–3.75. Values of  $\chi^2$  less than 10 are considered relatively small [26,27]. Therefore, the results of  $\chi^2$  suggest that Cauchy dispersion model is a good fit for the experimental data obtained from each silicon wafer.

The GPC is calculated by the slope of a linear regression fit to data of film thickness expressed as a function of number of deposition cycles. The GPC is 0.11 nm/cycle based on the six data points presented in Table 4. The coefficient of determination obtained by the linear regression confirms the linearity of the fit, i.e.  $R^2 = 1.0000$ . This result suggests that a target film thickness on silicon wafers can be predicted with high control.

Fig. 7(a)–(c) shows the spectrum of PCF 30 before coating (i.e. bare PCF), PCF 30 and PCF 60, respectively, when immersed in solutions with different RI.

The arrows in Fig. 7(a) and (b) show the trend of each valley as the SRI increases. The arrows in Fig. 7(c) are used to indicate the wavelength shift and the intensity change of each valley when the SRI is changed from water (i.e. SRI = 1.3327) to a glycerin solution of 20% (i.e. SRI = 1.3634). Fig. 7(a)–(c) shows that as the SRI increases, the central wavelength of each valley shifts towards higher wavelengths. By comparing Fig. 7(b), and (c) it can be observed that thicker coatings lead to greater wavelength shifts.

The central wavelength of each valley in the spectrum of bare PCF, PCF 30, PCF 60, and PCF 90 as a function of SRI is shown in Fig. 8(a)–(d), respectively. For comparison, the horizontal and vertical scales are the same in these four figures.

As shown in Fig. 8(a), the three valleys of the bare PCF have similar responses to changes in SRI. As the SRI increases, the sensitivity of each valley (i.e. the slope of a linear fit applied to the experimental data) of bare PCF increases gradually. For solutions with RI values higher than 1.4483, the cladding mode becomes a radiation mode and the interferometric pattern is no longer observed in the transmission spectrum.

The wavelength response of PCF 30, depicted in Fig. 8(b), show three different slopes corresponding to different sensitivities. To help visualization these results, sensitivity regions are defined, labeled as “I” (i.e. region I), “II” (i.e. region II), or “III” (i.e. region III). The mean sensitivity of valleys #1 through #3 over the SRI range corresponding to region I is 230 nm/SRI. The mean sensitivity of valleys #2 through #5 over the SRI range corresponding to region II is 1249 nm/SRI. The sensitivity of valley #5 over the SRI range corresponding to region III is 272 nm/SRI.

Note that the SRI value at the transition between two regions, referred to here as the *switch point*, is different for each valley. For example, in Fig. 8(b), the switch point between region I and II for valley #2, occurs at 1.3917, whereas the switch point of valley #3 occurs at 1.3990. The dashed lines in Figs. 8(b)–(d) indicate the approximate SRI value of the switch points.

The valleys in Fig. 8(c) show a region of high sensitivity (i.e. between 1.3327–1.4483) followed by a region of low sensitivity (i.e. between 1.4483–1.4727). Therefore, the SRI range of high sensitivity was labeled as region II, and the SRI range of low sensitivity was labeled as region III. The mean sensitivity of region II and III is 970 and 115 nm/SRI, respectively. For PCF 60, there may be a region I located at an SRI range lower than 1.3327, which is outside of the range of the test solutions used in this work.

Sensitivity regions II and III are also observed in PCF 90 as shown in Fig. 8(d). The SRI range associated with sensitivity region III of PCF 90 is significantly wider (i.e. between 1.3767–1.4727) compared to the same sensitivity region of PCF 30 and PCF 60.

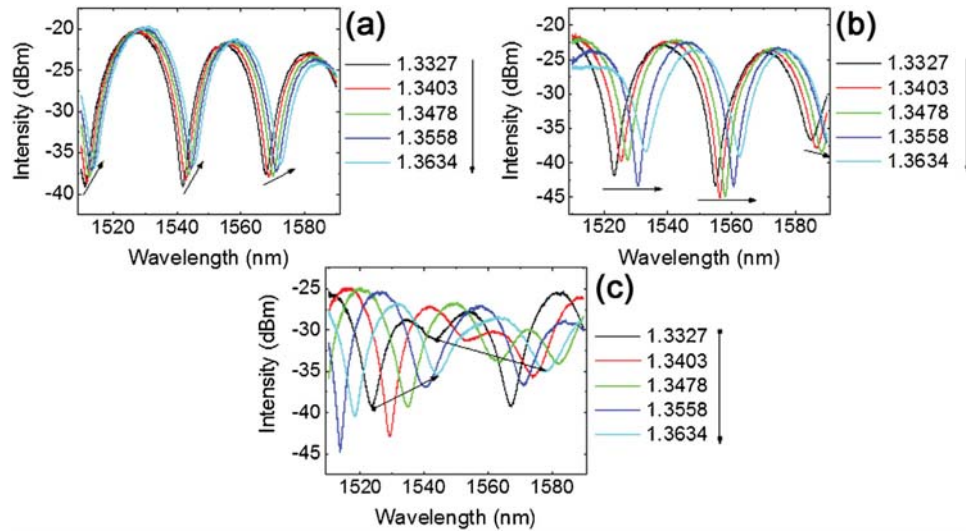
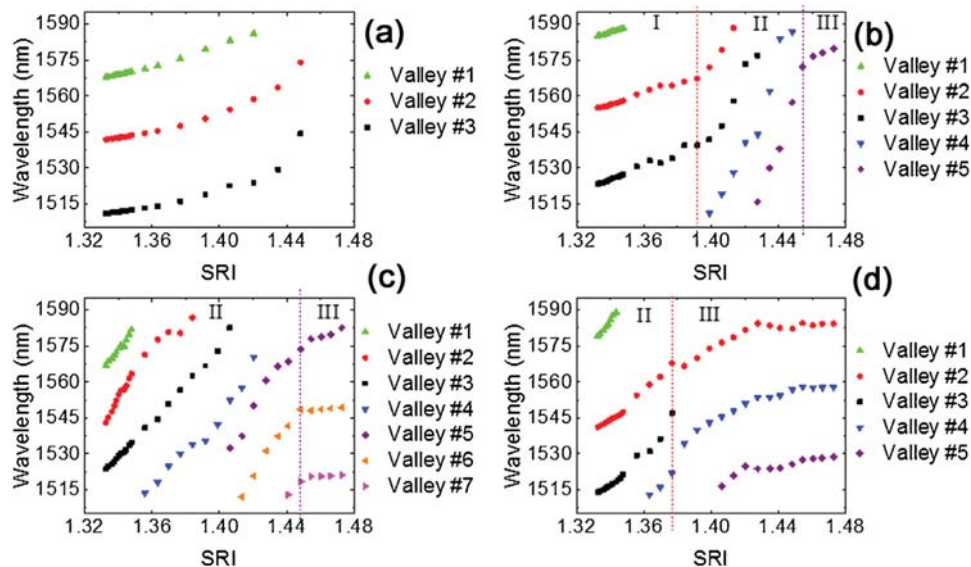
Comparison between Figs.(b), (c), and (d) suggests that, as coating thickness increases, the switch points of each coated PCF interferometer shift towards lower SRI values, and thus each sensitivity region is shifted towards a lower SRI range.

Development of sensors with high sensitivity to an SRI range in the vicinity of water was investigated. For each PCF interferometer, the valley of highest sensitivity at an SRI range between 1.3327–1.3478 is depicted in Fig. 9. The vertical dashed lines represent the SRI range of interest. To improve data visualization, the experimental points for each PCF interferometer were connected with a dashed lines. It can be seen that the increase of coating thickness from 30 nm (i.e. PCF 30) to 60 nm (i.e. PCF 60), increases the sensitivity of the sensor. Further increase of coating thickness leads to a decrease in sensitivity (see PCF 70 and PCF 90). The sensitivity values calculated in the SRI range between 1.3327–1.3478 are presented in Fig. 10. The maximum sensitivity is 1307 nm/SRI for a coating thickness of 60 nm.

**Table 3**

Film thickness measured on silicon wafers by ellipsometry and coating thickness measured on fiber samples by SEM.

| Label        | Purge time (s) | Ellipsometry on silicon wafers |          |                | SEM on fiber samples |                |
|--------------|----------------|--------------------------------|----------|----------------|----------------------|----------------|
|              |                | Thickness (nm)                 | $\chi^2$ | GPC (nm/cycle) | Thickness (nm)       | GPC (nm/cycle) |
| Deposition 1 | 10             | 69.45                          | 4.3      | 0.15           | 116 ± 12             | 0.25           |
| Deposition 2 | 20             | 53.11                          | 2.2      | 0.11           | 66 ± 11              | 0.14           |
| Deposition 3 | 30             | 50.30                          | 2.5      | 0.11           | 66 ± 7               | 0.14           |

**Fig. 7.** Spectra of (a) bare PCF, (b) PCF 30, and (c) PCF 60 at different SRI.**Fig. 8.** Wavelength shift as a function of SRI for (a) bare PCF, (b) PCF 30, (c) PCF 60 and (d) PCF 90.

#### 4. Discussion

The GPC calculated from film thicknesses of  $\text{HfO}_2$  measured by ellipsometry, is higher for Deposition 1 than for Depositions 2 and 3 (see Table 3). This occurs because the purge times specified for a deposition on a flat substrate are not sufficient for more complex substrate geometries. Insufficient purge times prevent a complete separation of the precursors in the process chamber leading to CVD-type reactions [20–22]. In CVD-type reactions, both precursors are present at the same time in the process chamber leading to gas-phase reactions. These reactions form material which is con-

tinuously deposited on the substrate. As a consequence, thicker coatings are expected in depositions where CVD-type reactions occur in addition to ALD compared to an ALD process [22].

The purge time of 10 s used in Deposition 1 was provided by the manufacturer as part of the standard method to deposit films of  $\text{HfO}_2$  on flat substrates at 200 °C. For silicon wafers coated with this standard method, the GPC measured by ellipsometry is 0.11 nm/cycle. The higher GPC observed on the silicon wafers for Deposition 1 was caused by the presence of the fiber fixtures and optical fibers in the process chamber. The optical fibers and the fiber fixtures disturbed the gas flow, creating dead spaces where

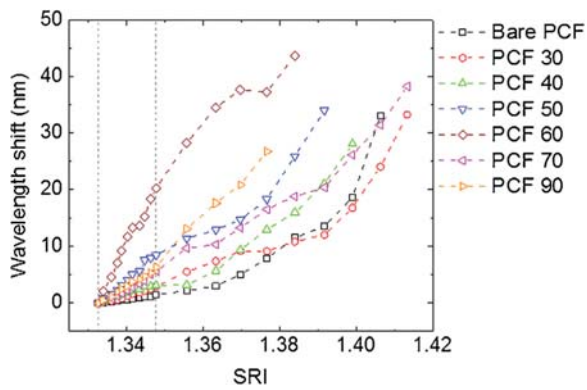


Fig. 9. Wavelength shift of PCF interferometers with different coating thicknesses.

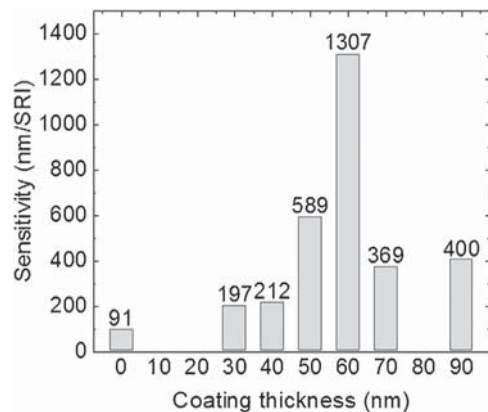


Fig. 10. Sensitivity of PCF interferometers coated with different coating thicknesses at an SRI range between 1.3327–1.3478.

the precursors were trapped. As a consequence, the gas precursors were not fully purged leading to CVD-type deposition, as discussed above. Target GPCs on silicon wafers were obtained when purge times were increased, as shown by the ellipsometry results in Depositions 2 and 3 (see Table 3).

The results of coating thickness measured by SEM on fiber samples show that increasing purge time from 10 s to 20 s leads to a reduction of GPC from 0.25 nm/cycle to 0.14 nm/cycle (see Table 3). Further increases in purge times do not change the GPC. This trend is in agreement with the results obtained by ellipsometry on silicon wafers. Therefore, both measurement methods show that for purge times higher than 20 s, consistent thicknesses are achieved independent of purge time.

For each deposition, the mean coating thickness measured by SEM on a fiber sample is greater than that measured by ellipsometry on a silicon wafer (see Table 3). The results shown in Table 3 were obtained using different measurement methods on different substrates. However, the SEM was also used to measure film thicknesses on a silicon wafer to compare with the thickness obtained by ellipsometry. The results show agreement within 2.7% using these different methods on the same substrate. This result suggests that the difference between thickness on silicon wafers and optical fibers is not due to the measurement method.

The difference between thickness measurements on silicon wafers and optical fibers may be due to the initial growth of  $\text{HfO}_2$  on the substrate. Ideally, GPC should remain constant during an ALD process. However, the GPC may vary at the start of the deposition because of nucleation [28–31]. Nucleation of a given material by ALD is dependent on the chemical composition of the substrate surface [28]. For the deposition of  $\text{HfO}_2$ , hydroxyl groups (OH) are the main nucleation sites due to the high reactivity of hafnium precursors

with OH groups [32]. Therefore, the GPC during  $\text{HfO}_2$  coverage on the substrate is dependent on the concentration of OH groups at the surface of the substrates. When the surface of the substrates is fully covered with  $\text{HfO}_2$ , the GPC should be the same regardless of substrate material (e.g., silicon wafers or optical fibers) because the  $\text{HfO}_2$  growth occurs over  $\text{HfO}_2$ , not the underlying substrate [30].

Optical fibers are made of silicon dioxide ( $\text{SiO}_2$ ) and are therefore expected to have higher concentrations of OH groups at the surface compared to silicon wafers. As a result, GPC during nucleation of  $\text{HfO}_2$  on optical fibers may be higher which would lead to thicker final coatings.

The GPC calculated from ellipsometry measurements on silicon wafers for Depositions 30, 40, 50, 60, 70 and 90, is in agreement with the GPC provided by the manufacturer. This result confirms that, with extended purge times, CVD-type reactions were successfully prevented on these depositions.

The coating of PCF interferometers induces up to three different sensitivity regions. The region of higher sensitivity was labeled as region II and is located between two regions of lower sensitivity (i.e. region I and III). As the coating thickness increases, the SRI values of the switch points between the three regions are shifted towards lower SRIs. Therefore, there is a value of coating thickness that allows tuning region II at a target SRI to promote maximum sensitivity of a coated PCF interferometer.

The maximum sensitivity for a coated PCF interferometer operating at the SRI range between 1.3327–1.3478 is 1307 nm/SRI for a deposition target coating thickness of 60 nm. PCF 50 and PCF 70 show sensitivities of 589 nm/SRI and 369 nm/SRI at the same SRI range, respectively. These results show the importance of using ALD to coat PCF interferometers due to the high control of coating thickness achieved by this method.

The PCF interferometers coated by ALD show higher sensitivity close to the RI of water than the maximum sensitivity reported previously for PCF interferometers. Smietana et al. reported a sensitivity 874 nm/SRI for a PCF interferometer coated with silicon nitride by radio frequency plasma enhanced CVD, operating at an SRI range in the vicinity of water [11].

The SRI sensitivity of coated PCF interferometers may be further increased by tapering the PCF before coating. Different tapering methods have been investigated to increase the sensitivity of uncoated PCF interferometers at low SRIs. Qui et al. investigated the sensitivity of PCF interferometers tapered by hydrofluoric acid [33]. The authors report an increase in sensitivity from 152 nm/SRI to 750 nm/SRI, in the SRI range between 1.3577–1.3739, by reducing the PCF diameter from 125  $\mu\text{m}$  to approximately 60  $\mu\text{m}$ . Li et al. investigated the tapering of PCF interferometers using the heat-and-pull method [34]. The authors report an increase in sensitivity from 223 nm/SRI to 1629 nm/SRI, at the SRI of 1.34, by reducing the fiber diameter from 125  $\mu\text{m}$  to 30  $\mu\text{m}$ . The combination of tapering with high-RI coatings to increase the SRI sensitivity of PCF interferometers is a promising research topic of future investigation.

The PCF interferometer proposed in this article represents an important contribution of an SRI sensor with high sensitivity at SRI values in the vicinity of water. The development of sensors with high sensitivities at low SRI is important in a large number of chemical and biological applications [1–3]. The simple and inexpensive fabrication method of PCF interferometers are key advantages compared with other high sensitivity sensors such as LPGs.

## 5. Conclusion

ALD was used to coat optical fibers with  $\text{HfO}_2$ . The effect of purge time between precursors, in the ALD process, on coating thickness applied to standard SMF was investigated. Desired coating thickness is achieved by increasing purge times relative to purge times required for deposition on a flat substrate.

This work also presents the first reported use of ALD to coat a fiber-optic RI sensor based on a Mach-Zehnder interferometer to increase sensitivity to SRI. We show that is possible to shift the region of higher sensitivity to a target SRI range by tuning the coating thickness. This demonstrates ALD as a suitable deposition method for these devices due to its potential to achieve high control of coating thickness.

Sensitivity of 1307 nm/SRI was obtained for an SRI range between 1.3327–1.3478, for a Mach-Zehnder interferometer with a coating thickness of 60 nm. This is the highest SRI sensitivity reported for a PCF interferometer at a low SRI range.

## Acknowledgments

The authors gratefully acknowledge funding provided by the Natural Sciences and Engineering Research Council of Canada (NSERC), Carbon Management Canada (CMC), and the Korean Carbon Capture and Sequestration R&D Center (KCRC). This work made use of the shared facilities of 4D LABS, which are supported by the Canada Foundation for Innovation (CFI), British Columbia Knowledge Development Fund (BCKDF), Western Economic Diversification Canada, and Simon Fraser University.

## References

- [1] M.J. Iqbal, M.A. Chaudhry, Thermodynamic study of three pharmacologically significant drugs: density, viscosity, and refractive index measurements at different temperatures, *J. Chem. Thermodyn.* 41 (2009) 221–226.
- [2] L. Melo, G. Burton, S. Warwick, P. Wild, Experimental investigation of long period grating transition modes to monitor CO<sub>2</sub> in high pressure aqueous solutions, *J. Lightwave Technol.* 33 (2015) 2554–2560.
- [3] D.A. Pereira, O. Frazão, J.L. Santos, Fiber Bragg grating sensing system for simultaneous measurement of salinity and temperature, *Opt. Eng.* 43 (2004) 299–304.
- [4] L. Melo, G. Burton, B. Davies, D. Risk, P. Wild, Highly sensitive coated long period grating sensor for CO<sub>2</sub> detection at atmospheric pressure, *Sens. Actuators B: Chem.* 202 (2014) 294–300.
- [5] J. Albert, L.Y. Shao, C. Caucheteur, Tilted fiber Bragg grating sensors, *Laser Photonics Rev.* 7 (2013) 83–108.
- [6] S.W. James, R.P. Tatam, Optical fibre long-period grating sensors: characteristics and application, *Meas. Sci. Technol.* 14 (2003) R49–R61.
- [7] A.B. Socorro, I. Del Villar, J.M. Corres, F.J. Arregui, I.R. Matias, Spectral width reduction in lossy mode resonance-based sensors by means of tapered optical fibre structures, *Sens. Actuators B: Chem.* 200 (2014) 53–60.
- [8] T. Zhu, D. Wu, M. Liu, D.W. Duan, In-line fiber optic interferometric sensors in single-mode fibers, *Sensors* 12 (2012) 10430–10449.
- [9] W.J. Bock, T.A. Eftimov, P. Mikulic, J.H. Chen, An inline core-cladding intermodal interferometer using a photonic crystal fiber, *J. Lightwave Technol.* 27 (2009) 3933–3939.
- [10] J. Villatoro, V.P. Minkovich, V. Pruneri, G. Badenes, Simple all-microstructured-optical-fiber interferometer built via fusion splicing, *Opt. Express* 15 (2007) 1491–1496.
- [11] M. Smietana, D. Brabant, W.J. Bock, P. Mikulic, T. Eftimov, Refractive-index sensing with inline core-cladding intermodal interferometer based on silicon nitride, *J. Lightwave Technol.* 30 (2012) 1185–1189.
- [12] M. Smietana, M.L. Korwin-Pawłowski, W.J. Bock, G.R. Pickrell, J. Szmiedt, Refractive index sensing of fiber optic long-period grating structures coated with a plasma deposited diamond-like carbon thin film, *Meas. Sci. Technol.* 19 (2008) 1–7.
- [13] H. Kim, H. Lee, W. Maeng, Applications of atomic layer deposition to nanofabrication and emerging nanodevices, *Thin Solid Films* 517 (2009) 2563–2580.
- [14] F. Zou, Y. Liu, C. Deng, Y. Dong, S. Zhu, T. Wang, Refractive index sensitivity of nano-film coated long-period fiber gratings, *Opt. Express* 23 (2015) 1114–1124.
- [15] M. Smietana, M. Myśliwiec, P. Mikulic, B.S. Witkowski, W.J. Bock, Capability for fine tuning of the refractive index sensing properties of long-period gratings by atomic layer deposited Al<sub>2</sub>O<sub>3</sub> overlays, *Sensors (Basel)* 13 (2013) 16372–16383.
- [16] D.J. Mandia, W. Zhou, M.J. Ward, H. Jores, J.J. Sims, J.B. Giorgi, J. Albert, S.T. Barry, The effect of ALD-grown Al<sub>2</sub>O<sub>3</sub> on the refractive index sensitivity of CVD gold-coated optical fiber sensors, *Nanotechnology* 26 (2015) 1–12.
- [17] S. Zhu, F. Pang, S. Huang, F. Zou, Y. Dong, T. Wang, High sensitivity refractive index sensor based on adiabatic tapered optical fiber deposited with nanofilm by ALD, *Opt. Express* 23 (2015) 13880–13888.
- [18] Y. Zhao, F. Pang, Y. Dong, J. Wen, Z. Chen, T. Wang, Refractive index sensitivity enhancement of optical fiber cladding mode by depositing nanofilm via ALD technology, *Opt. Express* 21 (2013) 26136–26143.
- [19] M. Smietana, M. Koba, E. Brzozowska, K. Krogulski, J. Nakonieczny, L. Wachnicki, P. Mikulic, M. Godlewski, W.J. Bock, Label-free sensitivity of long-period gratings enhanced by atomic layer deposited TiO<sub>2</sub> nano-overlays, *Opt. Express* 23 (2015) 8441–8453.
- [20] J.W. Elam, M.D. Groner, S.M. George, Viscous flow reactor with quartz crystal microbalance for thin film growth by atomic layer deposition, *Rev. Sci. Instrum.* 73 (2002) 2981–2987.
- [21] O. Sneh, R.B. Clark-Phelps, A.R. Londergan, J. Winkler, T.E. Seidel, Thin film atomic layer deposition equipment for semiconductor processing, *Thin Solid Films* 402 (2002) 248–261.
- [22] D.M. Hausmann, E. Kim, J. Becker, R.G. Gordon, Atomic layer deposition of hafnium and zirconium oxides using metal amide precursors, *Chem. Mater.* 14 (2002) 4350–4358.
- [23] X.L. Li, C. Li, Y. Zhang, D.P. Chu, W.I. Milne, H.J. Fan, Atomic layer deposition of ZnO on multi-walled carbon nanotubes and its Use for synthesis of CNT-ZnO heterostructures, *Nanoscale Res. Lett.* 5 (2010) 1836–1840.
- [24] D.S. Kim, S.M. Lee, R. Scholz, M. Knez, U. Gösele, J. Fallert, H. Kalt, M. Zacharias, Synthesis and optical properties of ZnO and carbon nanotube based coaxial heterostructures, *Appl. Phys. Lett.* 93 (2008) 1–3.
- [25] O. Bui, Y. Lu, I.Z. Mitrovic, S. Hall, P. Chalker, R.J. Potter, Spectroellipsometric assessment of HfO<sub>2</sub> thin films, *Thin Solid Films* 515 (2006) 623–626.
- [26] E. Langereis, S.B.S. Heil, H.C.M. Knoops, W. Keuning, M.C.M. Van de Sanden, W.M.M. Kessels, In situ spectroscopic ellipsometry as a versatile tool for studying atomic layer deposition, *J. Phys. D: Appl. Phys.* 42 (2009) 1–19.
- [27] G.E. Jellison, F.A. Modine, Parameterization of the optical functions of amorphous materials in the interband region, *Appl. Phys. Lett.* 69 (1996) 371–373.
- [28] R.L. Puurunen, W. Vandervorst, Island growth as a growth mode in atomic layer deposition: a phenomenological model, *J. Appl. Phys.* 96 (2004) 7686–7695.
- [29] M.T. Ho, Y. Wang, R.T. Brewer, L.S. Wielunski, Y.J. Chabal, N. Mouten, M. Boleslawski, In situ infrared spectroscopy of hafnium oxide growth on hydrogen-terminated silicon surfaces by atomic layer deposition, *Appl. Phys. Lett.* 87 (2005) 1–3.
- [30] M.L. Green, M.Y. Ho, B. Busch, G.D. Wilk, T. Sorsch, T. Conard, B. Brijs, W. Vandervorst, P.I. Räisänen, D. Muller, M. Bude, J. Grazul, Nucleation and growth of atomic layer deposited HfO<sub>2</sub> gate dielectric layers on chemical oxide (Si-O-H) and thermal oxide (SiO<sub>2</sub> or Si-O-N) underlayers, *J. Appl. Phys.* 92 (2002) 7168–7174.
- [31] Y. Wang, M. Ho, L.V. Goncharova, L.S. Wielunski, S. Revillon-Amy, Y.J. Chabal, T. Gustafsson, N. Mouten, M. Boleslawski, Characterization of ultra-thin hafnium oxide films grown on silicon by atomic layer deposition using tetrakis(ethylmethyl-amino) hafnium and water precursors, *Chem. Mater.* 19 (2007) 3127–3138.
- [32] M.A. Alam, M.L. Green, Mathematical description of atomic layer deposition and its application to the nucleation and growth of HfO<sub>2</sub> gate dielectric layers, *J. Appl. Phys.* 94 (2003) 3403–3413.
- [33] S.J. Qiu, Y. Chen, J.L. Kou, F. Xu, Y.Q. Lu, Miniature tapered photonic crystal fiber interferometer with enhanced sensitivity by acid microdroplets etching, *Appl. Opt.* 50 (2011) 4328–4332.
- [34] C. Li, S.J. Qiu, Y. Chen, F. Xu, Y.Q. Lu, Ultra-sensitive refractive index sensor with slightly tapered photonic crystal fiber, *IEEE Photonics Technol. Lett.* 24 (2012) 1771–1774.

## Biographies

**Luis Melo** received his M.Sc. degree in Physics Engineering from the University of Aveiro, Portugal in 2010. Currently, he is pursuing his Ph.D. degree in Mechanical Engineering at the University of Victoria in British Columbia, Canada, conducting his research in fiber optic sensors for detection of CO<sub>2</sub>. His areas of research include application of fiber-optic sensors for detection of chemical species, investigation of atomic layer deposition to coat sensors, and utilization of scanning electron microscopy to characterize materials.

**Geoff Burton** received his Bachelor's degree in mechanical engineering in 2012 from the University of Victoria, Canada. Since then, he has worked as a research engineer at IESVIC, the Institute for Integrated Energy Systems at the University of Victoria. His research is focused on fiber-optic sensor design for the detection of chemical species.

**Peter Wild** is a Professor in the Department of Mechanical Engineering at the University of Victoria. He holds the Natural Sciences and Engineering Research Council (NSERC) Chair in Sustainable Energy Systems Design and is the Director of the Institute for Integrated Energy Systems at UVic (IESVic). Dr. Wild's research interests include: optical sensors for industrial, environmental and biomedical applications; impacts of integration of renewable energy generation into existing grids; and renewable energy generation technologies.

**Philip Kubik** is a Process Engineer at 4D LABS. His areas of research include utilization of atomic layers deposition to coat different substrates with various coating materials. He is also an expert on using different techniques for materials characterization including X-ray Photoelectron Spectroscopy angle-resolved, X-ray Photoelectron Microscopy, Auger Electron Spectrometry, Scanning Electron Microscopy and Secondary Ion Mass Spectrometry.